In-operando spatially resolved probing of solid oxide electrolysis/fuel cells

Pitscheider, Simon

Publication date:
2018

Document Version
Publisher's PDF, also known as Version of record

In-operando spatially resolved probing of solid oxide electrolysis/fuel cells

Simon Pitscheider

Ph.D Thesis
Submitted on 30/4/2018

Supervisors:
Dr. Christodoulos Chatzichristodoulou
Dr. Karin Vels Hansen
Dr. Johan Hjelm
Dr. William C. Chueh

Table of Contents

Preface

This work is presented to the evaluation committee and the Ph.D. school of the Technical University of Denmark in candidacy for a Ph.D. degree. It is the result of three years of experimental work, funded through the ECoProbe project by the Danish Independent Research Council (Grant DFF – 4005-00129), as well as a six months stay at the University of Stanford, which was possible thanks to the additional funding provided by the Otto Mønsteds Fond (17-70-0196) and SUNCAT in collaboration with the Danish Agency for Science and Higher Education (7032-00001B). Furthermore, for granting the access to their synchrotron radiation facilities we acknowledge the Elettra synchrotron and the Advanced Light Source, which is a DOE Office of Science User Facility under contract no. DE-AC02-05CH11231.

The work was performed under the supervision of Dr. Christodoulos Chatzichristodoulou, with co-supervision and useful discussions from Dr. Karin Vels Hansen, Dr. Johan Hjelm, Dr. William Chueh, Prof. Torben Jacobsen and Prof. Mogens Bjerg Mogensen.

Abstract

The reactions occurring at the oxygen electrodes of solid oxide fuel and electrolysis cells (SOFC/SOEC - SOC) were investigated, both with conventional techniques and with advanced *in situ* techniques, in order to study the reaction mechanisms and the surface evolution of the electrode materials under realistic operating temperatures and oxygen partial pressures. For this purpose, model (La,Sr)(Co,Fe)O_3 (LSCF), (La,Sr)FeO_3 (LSF) and La(Ni,Fe)O_3 (LNF) electrodes were produced with pulsed laser deposition (PLD) and characterized using electrochemical impedance spectroscopy (EIS), X-ray photoelectron spectroscopy (XPS), scanning photoemission microscopy (SPEM) and high temperature scanning probe microscopy (SPM) with the additional functionality of Kelvin probe force microscopy (KPFM). In particular, XPS and SPEM represent novel tools with respect to solid state electrochemical characterization, as they only recently have been reaching relevant operating conditions in terms of obtainable temperatures and oxygen pressures in the experimental chambers. KPFM is a less established technique with respect to SOC studies, being used mostly at low temperatures in corrosion science and for the study of semiconducting devices, but has a great potential and was optimized for the desired operating parameters during this work, obtaining promising results.

The influence of the experimental conditions on the surface exchange, as measured by EIS on model thin film electrodes produced by PLD, was the subject of the first main study. The influence of current constriction, current collector material and design and the purity of the gases proved to be most important with respect to R_{surf}. However, other parameters were also evaluated, such as the stoichiometry of the thin films and their geometric area, but showed negligible effects with respect to the aforementioned parameters. The results succeeded in reproducing the scatter of three orders of magnitude present in literature data for the PLD, and resulted in a set of useful guidelines for measuring the intrinsic electrode materials performance and avoiding the influence of external artifacts.

In the second main study, the oxygen electrode reactions were studied under polarization, obtaining current-voltage profiles in varying oxygen partial pressures ranging between atmospheric oxygen content (210 mbar) and 10^{-1} mbar at 600 °C. These studies were integrated by surface chemistry characterization performed with XPS in an oxygen content between 1 mbar and 10^{-2} mbar at 600 °C, and with the added benefit of lateral spatial resolution of the surface chemistry with SPEM in $2.6\text{-}5\cdot10^{-2}$ mbar oxygen at 600 °C. The surface chemistry characterization allowed an interpretation of the surface behavior, both in terms of degradation and with respect to the oxygen reactions, and for the first time a correlation between the electrode overpotential and the surface potential was deduced. Furthermore, the outcome of the studies of the electrode reactions under polarization also allowed the identification of the most probable reaction pathway for the oxygen incorporation.

SPEM was also used to investigate, with lateral spatial resolution, the surface chemistry and the electrical potential profiles in distributed electrodes deposited on thin electrolytes, in an attempt to contemporarily study the evolution of the surface chemistry and the distribution of the electric potentials in the LSCF electrodes and the GDC electrolyte under externally applied potential differences. The sample was designed as a model system which could replicate the composite nature of technological SOC electrodes. The

overpotential distribution that was experimentally determined between the electrodes and the electrolyte was compared with finite element modelling simulations, showing good correspondence between the simulated values and the measured ones.

In order to approach the real operating conditions for the study of SOC materials, SPM and KPFM were performed in a specially designed microscope at temperatures of up to 600 °C in atmospheres ranging from pure N_2 to pure O_2 on a model sample, consisting of two isolated LNF electrodes on an MgO substrate. The sample could be used as a high temperature capacitor in order to evaluate the spatial resolution of KPFM in the relevant conditions, as well as the quality of the obtainable signal and the stability of commercial probes in more demanding operating conditions than the ones usually present in SPM setups. The results were very promising, and KPFM could represent a useful technique in future studies of SOC materials in realistic operating conditions, combining topographic characterization with chemical and electrostatic distributions across the sample surface.

Resumé

Reaktionerne som foregår ved iltelektroderne i faststofoxid brændsel- og elektrolyseceller (SOFC/SOEC - SOC) blev analyseret, både med konventionelle teknikker og med avancerede in-situ teknikker på specielt udviklede prøver. Formålet var at undersøge reaktionsmekanismerne og kemiske eller strukturelle overfladeændringer på elektrodematerialer ved realistiske temperaturer og iltpartialtryk. Derfor blev modelelektroder af (La,Sr)(Co,Fe)O_3 (LSCF), (La,Sr)FeO_3 (LSF) og La(Ni,Fe)O_3 (LNF) fremstillet med pulsed laser deposition (PLD). Prøverne blev testet med elektrokemisk impedansspektroskopi (EIS), X-ray photoelectron spectroscopy (XPS), scanning photoemission microscopy (SPEM) og højtemperatur scanning probe microscopy (SPM) i form af Kelvin probe force microscopy (KPFM). Specielt *in situ* XPS og SPEM er nye teknikker i forhold til analyse af faststofoxid-elektrokemi, da de først for nylig er blevet tilgængelige ved relevante temperaturer og iltpartialtryk. KPFM har været brugt endnu mindre til SOC-studier og bruges mest ved lav temperatur i korrosionsvidenskab og halvlederstudier, men teknikken har et stort potentiale og blev optimeret i løbet af dette studie, hvilket bringer teknikken en stort skridt videre.

Effekten af forskellige eksperimentelle parametre på overfladereaktionerne, målt med EIS på model-tyndfilmselektroder fremstillet med PLD, blev undersøgt i det første hovedstudie. Strømkonstriktion, materialet og geometrien af de elektriske kontakter og renheden af gasserne blev identificeret som de vigtigste parametre i forhold til overfladereaktionerne. Andre parametre blev også undersøgt, bl.a. støkiometrien og arealet af elektroderne, men deres virkning var ubetydelig i forhold til de førnævnte parametre. Resultaterne af det første hovedstudie reproducerede den store spredning på tre størrelsesordener, som man kan finde i litteraturkilder for overflademodstanden på LSCF-elektroder og kan bruges som et sæt af forholdsregler til at måle den reelle overfladeaktivitet uden indflydelse af eksterne påvirkninger.

I det andet hovedstudie blev iltelektrodereaktionerne undersøgt under polarisering, og strøm-spændingskurver blev målt ved 600 °C mellem 210 mbar og 10^{-1} mbar iltpartialtryk. Overfladekemien blev også undersøgt med XPS ved 600 °C mellem 1 mbar og 10^{-2} mbar iltpartialtryk, og med lateral opløsning med SPEM ved 600 °C og et iltpartialtryk på $2.6\text{-}5\cdot10^{-2}$ mbar. Ændringerne i overfladekemien blev brugt til at analysere degradering og iltreaktioner. For første gang blev en sammenhæng mellem overpotentialet og overfladepotentialet etableret. Undersøgelsen af elektrodereaktionerne under polarisering gjorde det også muligt at identificere den mest sandsynlige reaktionsmekanisme for iltreduktionen.

SPEM blev også brugt til lateralt at kortlægge overfladekemien og udbredelsen af de elektriske potentialer på distribuerede elektroder i LSCF-elektroderne og GDC-elektrolytten under polarisering. Prøven blev designet til at simulere den komplekse mikrostruktur af teknologiske SOC-elektroder. Fordelingen af overfladepotentialet blev målt mellem elektroderne og elektrolytten, og sammenlignet med finite element modelling simuleringer. Dataene fra eksperimenterne var i overensstemmelse med dataene fra simuleringen.

SPM og KPFM blev brugt i det sidste hovedstudie i et specialbygget mikroskop til operando studier ved SOC betingelser. Eksperimenterne forløb ved op til 600 °C i N_2 og O_2 på en prøve lavet af to isolerede LNF-elektroder fremstillet med PLD på et MgO-substrat. Prøven blev brugt som en højtemperaturkondensator til at evaluere lateralopløsningen og potentialsensitiviteten sammen med stabiliteten af kommercielle SPM-prober,

som normalt ikke bliver brugt ved høj temperatur og oxiderende atmosfærer. Resultaterne viste at KPFM vil være en nyttig teknik i fremtidlige SOC-studier ved realistiske betingelser, hvor man kombinerer topografimålinger med kemiske og elektriske målinger på prøveoverfladen.

Acknowledgements

Three years can be a very long time, or they can feel like the blink of an eye if one is surrounded by a motivating environment and is enjoying what he is doing. I can count myself between the fortunate ones belonging to the second category, and looking back to the last 3 years I sometimes have a hard time believing they're gone already. Many people contributed to making this experience a positive one, and helped me through the more challenging moments.

First of all, none of this would have been possible without my supervisor, Christos, who has shown a lot of helpfulness (and patience!!!) from the first interview back in 2014, through all the ups and downs of the project. He's been very helpful and supportive whenever we had setbacks or problems and managed to keep me motivated and on track, and also participated actively to two of the beamtimes we had during these years.

Second, I'd like to thank all my co-supervisors, Karin, Johan and Will, who welcomed me in his group at Stanford, as well as Torben and Mogens for all the useful discussions and inputs and the help with my experiments and with the data analysis, often offering different points of view and new potential investigation paths.

Third, I would like to thank all colleagues who helped me throughout these years: a big thank you goes to Simone for his help with the PLD work, to Kosova for the sample production and the brainstorming when something was not working, as well as Zixuan, Michael, Dawei and Di for the help with the experiments and the beamtimes performed at Stanford and Berkeley. The beamtimes were also successful thanks to other participating people, such as Torben, Nicola, Matteo, Luca, Patrick and Hikmet for the two Elettra beamtimes and Hendrik and Ethan for the two ALS beamtimes. Finally, I had lots of help from the technical and scientific staff at Risø, so thank you to Ebtisam, Jens B., Jens Ø, Jørgen, Kion, Karl, Janet and all others that in one or the other way helped me preparing and analyzing the samples.

Social life is as important as results, when it comes to defining a positive experience, and for this I have to thank all my countless colleagues and friends, near, far and further away still (way too many to singularly address each one of you, sorry about that!), with whom I spent lots of time over lunch breaks in the canteen, coffee breaks and relaxing and fun evenings at the Friday Bar or in other occasions. I'd like to thank all the people who helped me establishing the Friday Bar as an organization and who keep helping me improving it. I'd also like to thank the "Stanford Crew", which means Michael, David, Wolf, Marco, Matthias, Francesco and Tobias who made me feel at home from the moment I arrived at Stanford until either they left or I did. A big thank you also to Giovanni for being a good friend and gym buddy in the last stressful months!

My family always supported me in every choice, and even though I know it wasn't always easy to be far apart they were always by my side, and it's also thanks to them that I managed to get to the point I am. I know they are proud of me and I'm extremely happy for that, and I wish I can keep on doing so.

Last but not least, I'd like to thank my girlfriend Siw, who has been very supportive even though she got most of my more stressed time, and who also gave me strength and motivation whenever I had one of the (many) writer's blocks.

To all of you, and to whomever I might have forgotten (with deepest apologies), a huge THANK YOU

List of abbreviations

2PB	Two-phase boundary
3PB	Three-phase boundary
AC	Alternate current
AFM	Atomic force microscopy
ALS	Advanced light source
AM	Amplitude modulation
ASR	Area-specific resistance
BE	Binding energy
CAHT	Controlled atmosphere - high temperature
CC	Current collector
CE	Counter electrode
CPD	Contact potential difference
CV	Cyclic voltammetry
DC	Direct current
DFT	Density functional theory
EC	Electronic conductor
EDS	Energy dispersive spectroscopy
EIS	Electrochemical impedance spectroscopy
FIB	Focused ion beam
FM	Frequency modulation
GDC	Gadolinia-doped ceria
GDMS	Glow discharge mass spectroscopy
HF	High frequency
HT	High temperature
IC	Ionic conductor
ICP-MS	Inductively coupled plasma mass spectroscopy
IV	Current-voltage

KPFM	Kelvin probe force microscopy
LF	Low frequency
LNF	$La(Ni,Fe)O_3$
LSCF	$(La,Sr)(Co,Fe)O_3$
LSF	$(La,Sr)FeO_3$
LSM	$(La,Sr)MnO_3$
ME	Microelectrode
MF	Medium frequency
MIEC	Mixed ionic and electronic conductor
NAP	Near-ambient pressure
NGO	$NdGaO_3$
OCV	Open circuit voltage
PLD	Pulsed laser deposition
$\boldsymbol{pO_2}$	Oxygen partial pressure
$\boldsymbol{R_{surf}}$	Surface exchange resistance
SC	Symmetric cell
SDC	Samaria-doped ceria
SEM	Scanning electron microscopy
SOC	Solid oxide cell
SOEC	Solid oxide electrolysis cell
SOFC	Solid oxide fuel cell
SPEM	Scanning photoemission microscopy
SPM	Scanning probe microscopy
ToF-SIMS	Time of flight secondary ion mass spectroscopy
UHV	Ultra-high vacuum
WE	Working electrode
XPS	X-ray photoelectron spectroscopy
XRD	X-ray diffraction
YSZ	Yttria-stabilized zirconia

1 Introduction

1.1 Principles of solid oxide cells

In the effort to limit the contribution of human activities to climate change, mostly caused by pollutants and greenhouse gases, focus is placed on moving from conventional energy conversion sources to cleaner alternatives. Renewable energy sources, such as wind and solar power, are improving in terms of cost-efficiency and their installed capacity is increasing fast, but their intermittent nature poses a challenge for the stability of the energy grid, bringing forward the need to be supported by efficient and large scale energy storage technologies.

In this context, solid oxide fuel and electrolysis cells (SOFC/SOEC – SOC) represent one of the best candidates, as they are among the most cost-efficient reversible energy conversion technologies, capable of converting the chemical energy of fuels to electrical energy without emitting particulate matter or toxic exhaust gasses such as NO_x [1–4]. Furthermore, when operated reversibly, they are also capable of storing excess electrical energy from renewable sources in the form of fuels [5–7].

The electrochemical energy conversion occurs through two reversible sets of reactions, namely oxygen incorporation coupled with fuel oxidation and oxygen evolution coupled with fuel production. In the first case, which corresponds to the fuel cell mode, chemicals of high free energy (for ex. H_2, CO, O_2) are converted into chemicals of lower free energy (H_2O and CO_2) and the excess energy is released in the form of electricity. In the second case, corresponding to electrolysis cell mode, the opposite process is realized by supplying electrical energy and reverting the chemical processes, as can be seen in Figure 1.1.

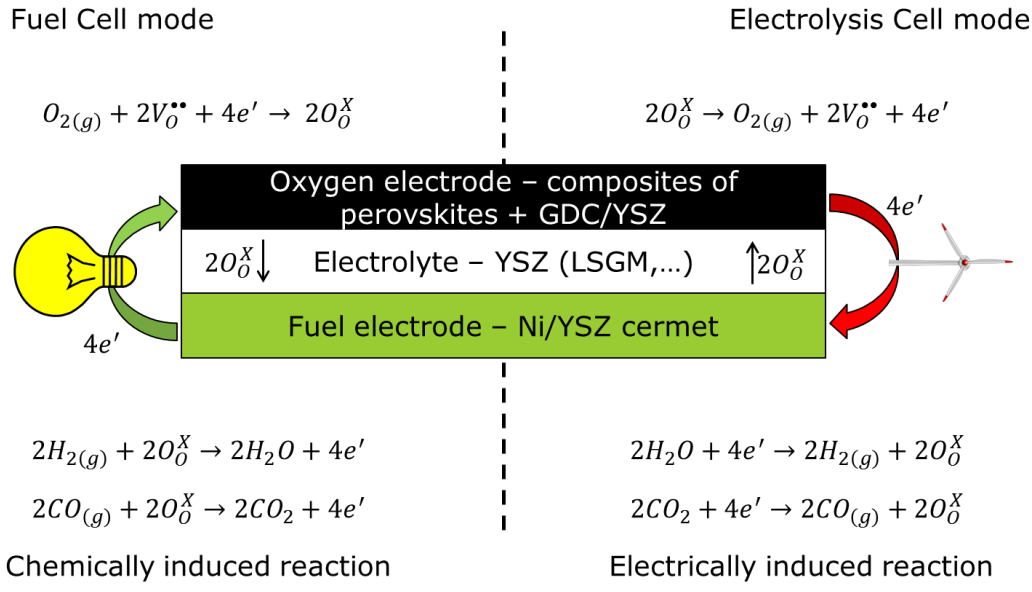

Figure 1.1. Overview of reactions occurring at SOC electrodes.

The efficiency under operation of SOCs depends on many parameters, and can be determined by observing the deviation of the cell voltage from the expected potential difference derived from the free energy difference between reactants and products. The potential losses can be simplified and divided into four main categories [8]:

- Activation losses correlate to the non-linear potential drops associated with the electrode reactions and are associated with the so-called Tafel slope and the equilibrium exchange current, namely the slope and the zero-voltage intercept that can be deducted by plotting the electrode overpotentials versus the natural logarithm of the current density flowing through the cell. They can be reduced by employing more catalytically active materials and by operating at high temperature, but still represent the most investigated aspects of the cell performance.
- Fuel crossover and internal losses are present when the electrolyte is either not dense, allowing part of the fuel to migrate and react with the oxygen without the production of electrical current, or electronically conductive and therefore dissipating part of the produced electrical energy. These types of losses mostly affect the open circuit voltage (OCV).
- Ohmic losses relate to resistive processes and are linear potential drops dominated by the electrolyte conductivity. For this reason, state-of-the-art SOCs employ thin electrolytes to minimize such losses.
- Mass transport or concentration losses are present when the mass supply of reactants to the electrode surfaces is not sufficient, and are usually seen at high current densities. This type of losses can partially be prevented by enhancing the active areas of the electrodes and using high gas supplies.

Activation or polarization losses are divided between the fuel electrode and the oxygen electrode, although in the case of hydrogen fuel cells the fuel electrode activation is negligible compared to the oxygen electrode activation [8]. This work concentrates in particular on the reactions taking place at the oxygen electrode, as these are still poorly understood and represent one of the most important aspects to be improved in terms of activity and stability.

The electrodes can be structured as either single phase or composites. Typically, the electrodes can consist of mixtures of electronic conductors (EC) and ionic conductors (IC), as well as mixed ionic and electronic conductors (MIEC) or intermediate combinations [9]. MIECs offer the advantage of being active for the oxygen reactions on the whole surface exposed to the gas, exhibiting a two-phase boundary (2PB) nature of the processes, while in EC/IC composites the active sites are limited to the three-phase boundary (3PB) where the two materials and the gas meet [10,11].

1.2 Materials used in SOCs

SOC oxygen electrodes primarily consist of perovskite-type oxides, a class of ceramic materials that share the crystal structure with the mineral Perovskite ($CaTiO_3$). The general formula for perovskites is ABO_3, where A is typically a large cation in a twelve-fold coordination with the oxygen anions (Figure 1.2a) and B is a small cation in six-fold coordination with the oxygen anions (Figure 1.2b). Substitution on one or both sites with ions of different valence can be used to promote electronic and/or ionic conductivity [12–16].

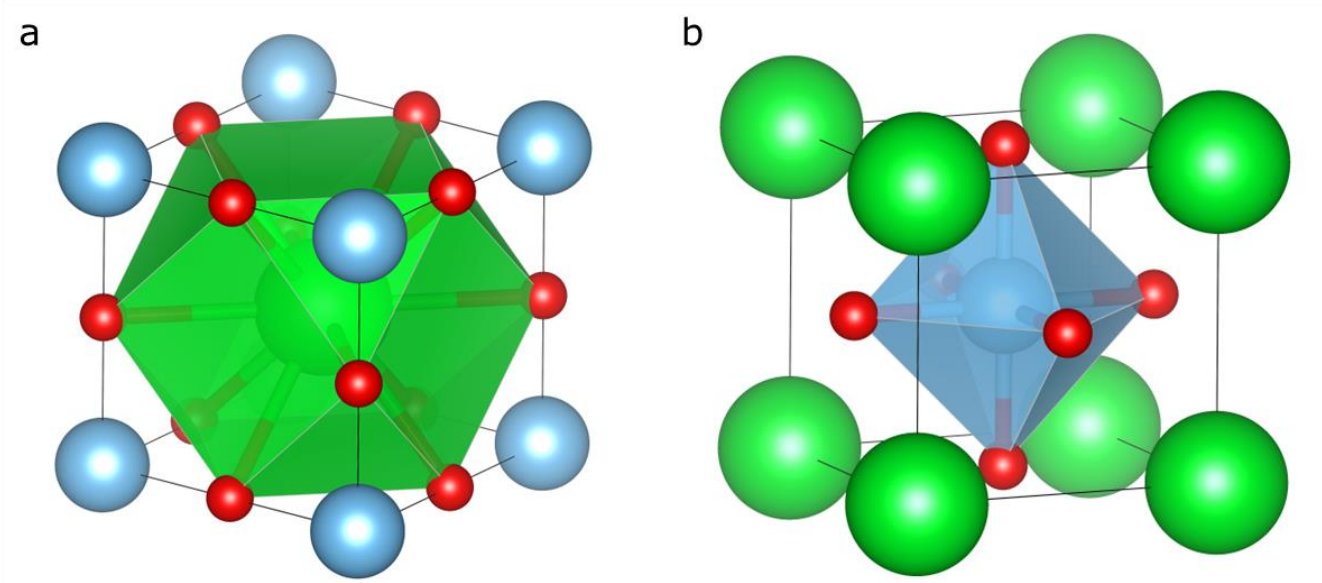

Figure 1.2. Perovskite crystal structure, centered a) on the A cation and b) on the B cation, realized with VESTA [17]**.**

The common choices for state-of-the-art SOC electrodes are represented by Sr-substituted $LaMnO_3$ (LSM), which is primarily electronically conductive, and - more recently - Sr- and Co- substituted $LaFeO_3$ (LSCF), which is a MIEC [18].

Common electrolyte materials for SOCs are represented by oxides with the Fluorite (CaF_2) structure (shown in Figure 1.3), even though perovskites are seen with progressively more interest in recent years for better lattice and thermal expansion compatibility with the electrodes [18]. The most common choices are represented by ZrO_2 or CeO_2, using cations with a lower valence, such as Y and Sc for ZrO_2 or Gd, Pr and Sm for CeO_2 to increase their ionic conductivity and, in the case of ZrO_2, to stabilize the cubic crystal structure [16].

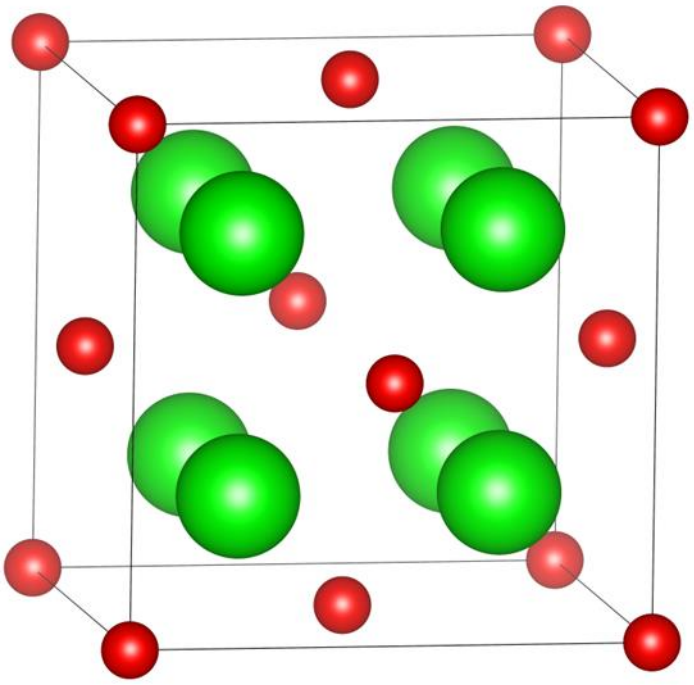

Figure 1.3. Fluorite crystal structure, realized with VESTA [17]**.**

1.3 Properties of LSCF

LSCF possesses a multitude of properties that made it one of the most studied materials for SOC oxygen electrodes. In particular, Tai et al. studied the crystal structure, thermal expansion coefficient, Seebeck coefficient and electrical conductivity of LSCF with different Co contents on the B-site [19] and different Sr contents on the A-site [20]. Both Sr and Co increased the electrical conductivity of LSCF, enabling reaching values in the 10^2-10^3 S/cm range, as well as the weight loss due to oxygen excorporation at high temperature and the thermal expansion coefficient. The electrical conductivity proved to be dominated by a p-type, thermally activated small polaron hopping mechanism. The oxygen nonstoichiometry of LSCF was also studied as a function of pO_2 for different temperatures and Co- contents on the B-site, showing reduced stability ranges in pO_2 when more Co was present [21,22]. Finally, the Co- and Sr- content affect also the ionic conductivity of LSCF, which increases with increasing quantities of both elements, reaching values within the 10^{-2}-1 S/cm range at 800 °C [23].

In terms of surface exchange, LSCF performs better than the conventional state-of-the-art oxygen electrode material, (La,Sr)MnO_3, and the performance increases with increasing Co-content from (La,Sr)FeO_3 (LSF) through LSCF until (La,Sr)CoO_3 (LSC). Even better performances can be found with other types of perovskites, such as (Sm,Sr)CoO_3 (SSC) or(Ba,Sr)(Co,Fe)O_3 (BSCF), but at the cost of lower stability when subjected to high cathodic polarizations and low pO_2 [24–26].

The surface exchange data that can be found in literature are scattered over three orders of magnitude and often lack pO_2 dependence, as will be discussed more in detail in chapter 3. This underlines how difficult it

is to obtain a reliable measurement of the surface activity of electrode materials, which is a core requirement for the understanding of the reaction kinetics.

Being a MIEC is one of the reasons for the higher activity of LSCF towards the oxygen reactions, since the reaction occurs on the whole available electrode area; however, the determination of the precise reaction pathway and the reaction intermediates cannot be simply deduced from surface exchange data. Only if the experimental data are integrated with density functional theory (DFT) calculations, possible pathways can be outlined, identifying the most likely reaction mechanism as a function of the oxygen vacancy concentration in the electrode material [27].

1.4 Motivation of the present work

This work will concentrate on the investigation of the oxygen reactions on the surface of LSCF electrodes, with the aim of studying their fundamental aspects, both in terms of intrinsic activity of the electrode materials and by attempting a mechanistic interpretation of the processes occurring at the electrode surface derived solely from experimental results. Multiple techniques will be explored and developed, in order to assess their potential in terms of obtainable information with the aim of achieving *in situ* spatially resolved measurements which can help probing the materials in or close to real operating conditions and thereby "visualize" the oxygen incorporation and evolution pathways on technological SOC electrodes.

1.5 Approach of the present work

Given the high complexity of SOC oxygen electrodes and the high number of chemical, structural and morphological parameters which need to be taken into account, a fundamental comprehensive investigation of the electrode reaction is nearly impossible. Current studies employ performance monitoring, such as electrochemical impedance spectroscopy (EIS), current-voltage curves (IV-curves), cyclic voltammetry (CV) while varying the gas compositions and flows at the electrodes, as well as the operating temperature. Additionally, these techniques can be used to study the long-term degradation of operating cells. Post-mortem characterization, such as 3D reconstruction using focused ion beam milling (FIB) in conjunction with scanning electron microscopy (SEM) can be used to observe the differences between the initial and the final state of the cells, but are unable to capture the causes for the variations under operation [28]. *In situ* techniques with high surface chemical sensitivity and lateral spatial resolution have recently been developed in order to attempt the investigation of the electrode materials' properties under realistic operating conditions, and will be described further in this work. However, the use of these techniques can not eliminate the multitude of parameters governing the investigated processes. For this reason, it can be useful to establish a series of model systems of increasing complexity and approach the problem in different steps.

The first parameter that needs to be controlled in order to study the electrode reaction is the microstructure of the electrode-gas and electrode-electrolyte interfaces. This can be done in different ways, but the approach used in this study was to use pulsed laser deposition (PLD) on single crystal substrates to produce films of well-defined crystal structure and active interface area.

Even when the active area and the microstructure of the investigated materials are well known, many external parameters can influence the materials' activity towards the oxygen reactions and cause a wide scatter in the reported literature values for the surface exchange resistance. This was the first issue that was

addressed in this work, and systematic studies varying for example film thicknesses, current collection strategies or gas purity were conducted and are described in detail in chapter 3.

Furthermore, the chemical evolution of the electrode surfaces, together with the relation between the overpotential applied to the electrodes and the corresponding surface potential changes are of great importance in order to investigate the reaction mechanisms for oxygen incorporation and evolution. For this reason, once appropriate testing procedures were established to exclude the influence of other parameters, the electrodes were characterized with chemically sensitive techniques, namely X-ray photoelectron spectroscopy (XPS) and scanning photoemission microscopy (SPEM) in advanced synchrotron beamlines. Such studies are described in detail in chapters 4 and 5. In particular, chapter 5 focuses on using the combined advantages of high chemical sensitivity and lateral spatial resolution of SPEM to attempt the investigation of electrodes with more complex structures. This represents an additional step of increasing complexity in a controlled manner towards the final goal of understanding technological SOC electrodes.

Another promising tool for the in operando characterization of SOC electrodes is represented by high temperature scanning probe microscopy (HT-SPM). SPM is normally not able to operate at high temperature, but a specially designed tool with appropriate modifications was used, as will be explored in chapter 2.7. Chapter 6 focuses on the development of this technique and on the first promising results that could be obtained. In particular, SPM was used with the additional capability of performing KPFM, and therefore map the work function distributions on the sample. KPFM is capable of operating in any atmosphere, and the use of this technique could, in the future, represent the best compromise to characterize in a single measurement the morphological, chemical and electrical evolutions of the surfaces in real operating conditions and with high spatial resolution.

1.6 Structure

This thesis is presented as a monograph, where the different studies are organized in a paper-like structure in separate chapters, each having their own motivation, presentation and discussion of results, and conclusions. In order to avoid unnecessary repetitions (where possible), the experimental techniques and parameters that were common to multiple studies are described in a self-standing chapter following the introduction. Finally, overall conclusions are drawn by considering the obtained achievements, and suggestions for future developments are offered.

2 Sample production and characterization techniques

2.1 Pulsed laser deposition [29]

Pulsed laser deposition (PLD) is a versatile technique used to fabricate thin films of a wide range of materials (oxides, polymers, metals) by transferring the material to be deposited from a target of the desired composition to a substrate. The deposition occurs when a laser pulse of high intensity hits the target material, which is not able to dissipate the laser energy as heat and instantaneously vaporizes, creating a plasma plume which is responsible for transferring the material to the substrate. A schematic design is shown in Figure 2.1. In order for the deposition to be more uniform, both the substrate and the target are rotated during the deposition, and the laser spot is scanned on the target surface.

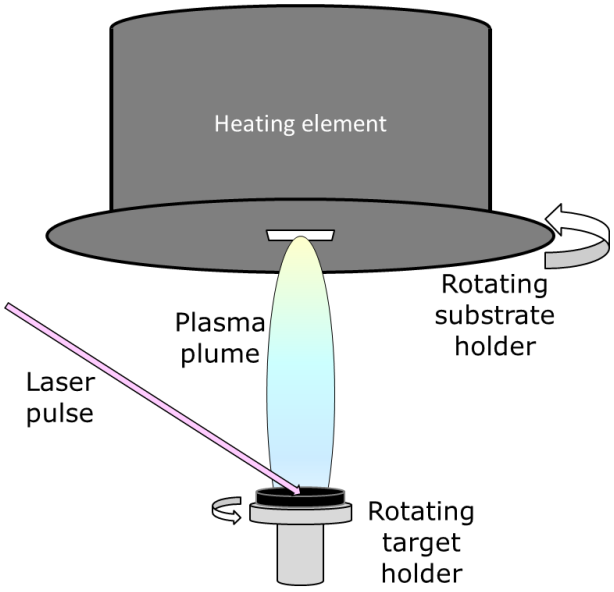

Figure 2.1. Schematic view of the PLD setup

In order for the films to grow with a coherent crystal structure, four main parameters can be tuned, namely the chamber atmosphere and pressure, the deposition temperature, the substrate-target distance and the frequency of the laser pulses. A systematic study of these parameters in the case of LSCF thin films was performed by Plonczak et al. [30], but the relevance of each parameter will be described shortly:

- **Chamber pressure:** The depositions are usually performed in a background pressure of O_2 (if oxides are deposited), but can also be performed in N_2 or Ar in certain cases. For oxides, the O_2 atmosphere is important in order to maintain the desired stoichiometry of the materials in the films, as well as to

reduce the kinetic energy of the deposition plume. Too high pressures can, on the other hand, reduce the deposition rate and cause porous structures in the deposited films.

- **Substrate temperature:** The substrate is usually heated to promote surface diffusion and thereby a uniform growth of the films. Low temperatures result in columnar or amorphous structures, but high temperatures represent a risk of interreactions and undesired secondary phase formation.
- **Substrate-target distance:** The plasma plume is highly directional, with the maximum amount of material deposited on the normal to the laser incidence spot and a decreasing radial deposition profile when moving away from the normal. In order to obtain a uniform deposition, the substrate-target distance should be kept as low as possible, but the system geometry might impose limitations in this respect (heating element in the beam path or similar).
- **Laser frequency:** Since the deposition rate is a function of laser pulses, a higher laser frequency implies that more material can be deposited in the same amount of time. However, high laser frequencies do not allow the surface to relax completely, and can therefore introduce porosity or columnar structures in the deposited layers. The frequency should therefore be chosen as a compromise between deposition time and film quality.

For the depositions performed in this work, the chamber pressure was varied between $6.7 \cdot 10^{-3}$ mbar and 0.1 mbar, the temperature between 600 and 650 °C, the substrate-target distance between 60 and 70 mm and the laser frequency between 10 and 20 Hz, depending on the material to be deposited.

The PLD targets used in this work were produced both using commercial powders as a starting point and with powders produced by solid-state synthesis:

LSCF powder with the stoichiometry $La_{0.58}Sr_{0.4}Co_{0.2}Fe_{0.8}O_3$ was supplied by H.C. Starck, LNF with the stoichiometry $LaNi_{0.6}Fe_{0.4}O_3$ was supplied by Kceracell, 10 mol % gadolinia-doped ceria (GDC) powder was supplied by Rhodia and 20 mol % samaria-doped ceria (SDC) was supplied by Fuel Cell Materials. The LSCF films from the commercial powder will be referred to as LSCF-A.

Solid-state synthesis was also used for LSCF and for LSF powders in order to tune the final stoichiometry more accurately. To distinguish the LSCF targets obtained with these powders from the previous ones, these will be referred to as LSCF-B. In this case, La_2O_3 (99.999%, Sigma-Aldrich), $SrCO_3$ (99.994%, Alfa Aesar), CoO (99.998%, Alfa Aesar) and Fe_2O_3 (99.998%, Alfa Aesar) were grinded together in a 99.8% alumina mortar and pestle (Coorstek) in amounts corresponding to the desired stoichiometry, namely $La_{0.61}Sr_{0.39}FeO_3$ for LSF and $La_{0.6}Sr_{0.4}Co_{0.2}Fe_{0.8}O_3$ for LSCF-B. The detailed procedure is described in [31].

The targets of LSCF-A, LNF and GDC were prepared by pressing the powders into 3.6 cm diameter cylindrical bodies in two steps: first uniaxially with 1.5 tons for 20 sec and then isostatically with 55 tons for 20 sec. LSCF-A targets were sintered at 1200 °C in air for 2 hours, LNF targets at 1400 °C in air for 24 hours and GDC targets at 1600 °C in air for 5 hours. The resulting targets were 2.5-2.6 cm in diameter. In the case of LSF, LSCF-B and SDC, the powders were pressed into pellets of 2.54-3.81 cm in diameter uniaxially with 7.5 tons for two 10-minutes rounds. Afterwards, they were sintered at a final temperature of 1200-1350°C in synthetic air for 10-15 hours, with intermediate steps at different temperatures to burn out the carbonates [31].

2.2 Photolithography and micropatterning

Photolithography is a technique widely used in the semiconductor industry, where patterns are transferred into a photosensitive polymer layer (photoresist) by shining UV-light through a photomask with the desired geometry. Depending on the type of photoresist, the transferred pattern can correspond to the one on the photomask, which means that the masked areas will remain on the sample after developing (positive photoresist), or to its negative, which means that the exposed areas will remain, as shown in Figure 2.2.

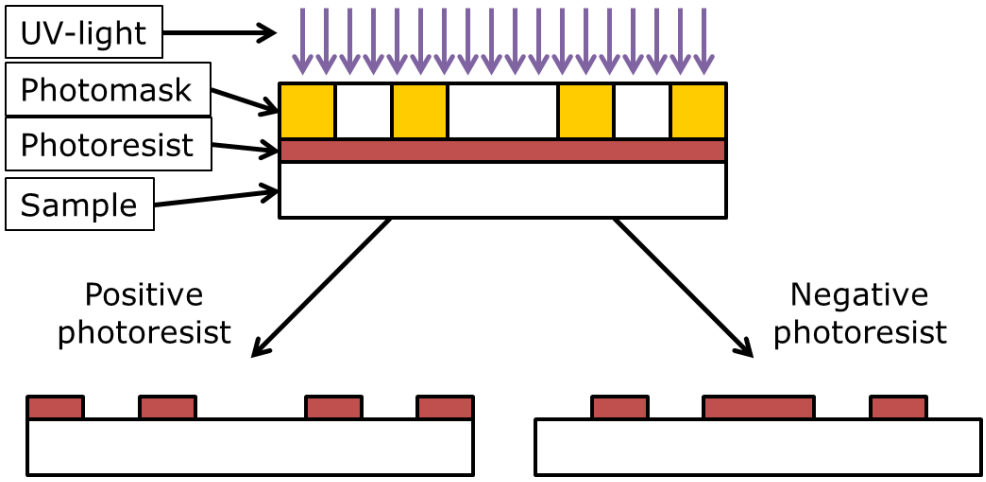

Figure 2.2. Schematic of the Photolithography process, with the two types of available photoresist.

With respect to thin films, photolithography is usually used to either selectively remove part of the thin film by means of physical or chemical etching, or to selectively deposit the material in desired areas.

Using physical etching techniques, such as Ar ion etching (Figure 2.3a), the whole surface is uniformly etched away by an Ar ion beam impacting on the sample. This strategy has the advantage of being directional, thereby transferring precisely the pattern into the film, but does not distinguish between materials, meaning that the photoresist is also removed simultaneously. An accurate calibration is necessary in order to determine a safe ratio between photoresist and film thickness and to establish the correct etching time to remove the thin film completely without removing the underlying material.

Using chemical etching techniques, for example with HCl or HF (Figure 2.3b), has the advantage of being material-sensitive. However, the etching proceeds isotropically and can therefore result in unwanted undercut structures.

The deposition of material through the holes in a photoresist pattern, also called lift-off deposition, represents a third widely used way to produce micropatterned films (Figure 2.3c). This strategy has the advantage of being more controllable than the previous strategies in terms of the obtained film thickness and geometry, but is suitable only for low temperature deposition techniques, excluding therefore PLD of complex oxides, typically requiring heating of the substrate to ca. 500 °C or higher for growth of coherent films. Furthermore, the edges of the photoresist need to be optimized for lift-off, as the solvent needs to be able to access the photoresist in order to obtain a complete removal of the undesired photoresist at the final step of the process.

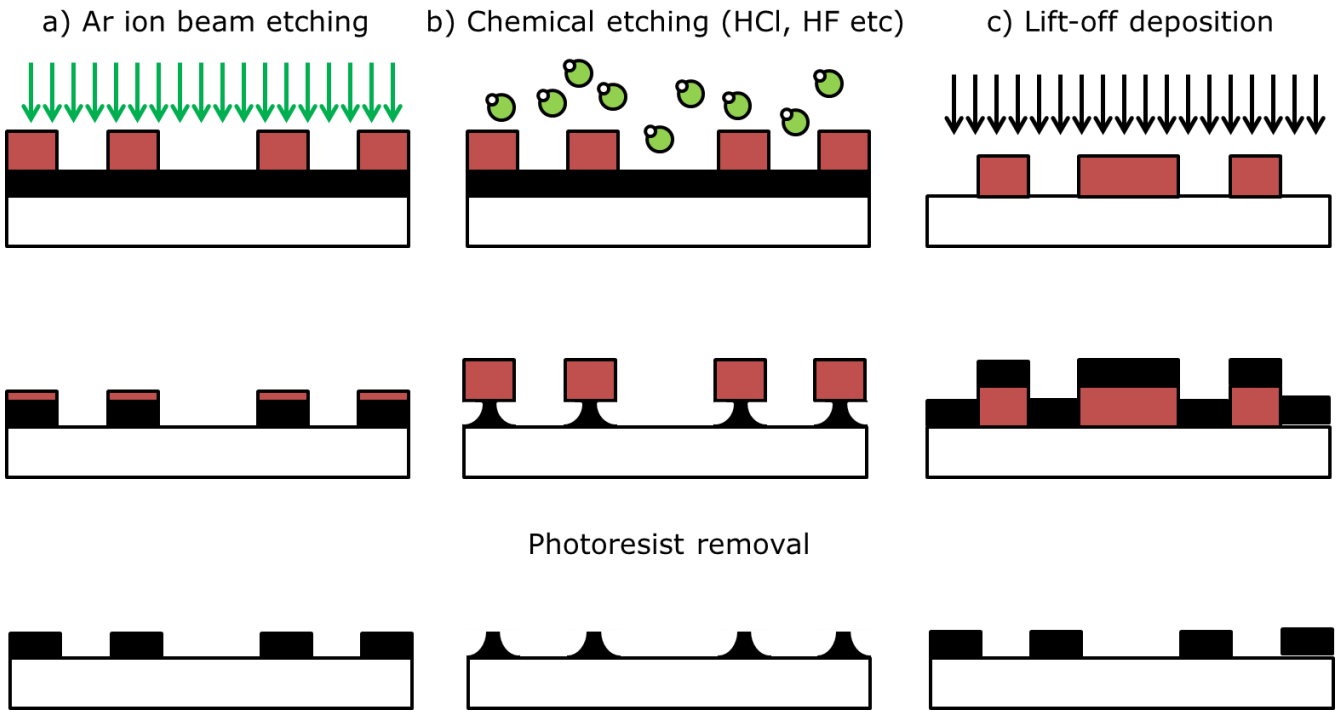

Figure 2.3. Possible microfabrication pathways.

In this work Photolithography was used in the studies described in chapter 5 and chapter 6 in combination with Ar-ion etching to produce patterned perovskite films, and in chapter 3 and chapter 4 in combination with Pt sputtering to produce patterned buried current collectors (CC) under the thin film electrodes using the lift-off technique. The alignment of the patterns with the samples and the exposure to UV light were performed using a Karl Suss MJB-3 mask aligner. In all cases positive photoresist was used (Microposit S1818, micro resist technology GmbH), with a Microposit LOL 2000 (micro resist technology GmbH) layer in the cases where the lift-off route was adopted. The development of the photoresist was performed using the corresponding Microposit MF-319 developer (micro resist technology GmbH).

2.3 Scanning electron microscopy and energy-dispersive spectroscopy [32]

In SEM, an electron gun is used to produce a beam of electrons, which is focused onto the surface of the sample to be analyzed and scanned using electromagnetic fields (electromagnetic lenses), obtaining high-resolution images (potentially down to 1 nm resolution). The information obtainable by SEM varies according to the type of detector employed, but can typically be divided into two main categories, namely backscattered electrons and secondary electrons.

Backscattered electrons are electrons originating from the electron beam, which, as the name suggests, interact with the atoms in the sample and exit again in the same direction as the electron gun, being collected by the analyzer. Since the interaction between the electron beam and the atoms in the sample depends on the atomic mass, the contrast obtained in a backscattered electron image can be correlated with different elements in the surface. Heavier elements will reflect more electrons, resulting in brighter spots in the

image, while lighter elements will allow the electrons to travel further into the sample and therefore be absorbed, resulting in darker areas in the image.

Secondary electrons, on the other hand, are electrons with low kinetic energy (< 50 eV) spontaneously emitted by the surface atoms when hit by the electron beam. This type of electrons will escape the surface more easily in presence of edges, resulting in a topographic view of the sample.

Besides the two types of electrons that can be detected in SEM, the beam-sample interaction also produces element-specific X-rays, which can be used for a chemical characterization of the sample surface by energy dispersive spectroscopy (EDS).

In this work SEM was performed using a Zeiss Supra 35 microscope with a Thermo Scientific EDS analyzer, as well as with a Zeiss Merlin microscope. The samples were either observed without any treatment, typically to observe the film surface characteristics over the entire sample, or as cross-sections to evaluate the quality of the PLD film depositions. The cross-sections were either obtained by fracturing the samples or by embedding them in epoxy resin and polishing them with a 0.1 µm diamond suspension as a final step.

2.4 Time of flight secondary ion mass spectroscopy

Time of Flight Secondary Ion Mass Spectroscopy (ToF-SIMS) is a technique capable of analyzing the chemical composition of surfaces with sensitivity in the ppm range. A focused ion beam is aimed on the desired spot on the surface and a pulse of ions is released. The pulse impacts the sample surface and creates a chain reaction that releases secondary ions from the outmost surface layers. The emitted secondary ions are all accelerated with the same voltage and then transit through an analyzer column, where ions with a lower mass to charge (m/z) ratio will travel faster, resulting in a spatially distributed impact on the detector system. With ToF-SIMS, both imaging and depth-profiling can be carried out. Using imaging mode, a lateral spatial resolution of 250 nm of the surface composition can routinely be achieved. In depth profiling mode, in-depth resolution of 1-2 nm is usually obtained.

ToF-SIMS cannot be used to obtain quantitative information about the detected elements, but rather to observe their variations. In imaging mode, the number of counts for each element is normalized against the total number of counts registered from the spectrometer for that element in the analyzed area and plotted with an appropriate color scale. A similar normalization is applied in depth profiling.

In this work, ToF-SIMS was performed using a ToF-SIMS IV (ION-TOF GmbH) in order to characterize the surface of the samples before and after testing (chapter 3, chapter 4), or to determine the quality of films produced by photolithography and Ar ion etching (chapter 5).

The following experimental parameters were used, as reported from the scientist responsible for the ToF-SIMS analysis:

- 25 ns pulses of 25 keV Bi^+ (primary ions) in bunches of <0.9, frequency 10 kHz, current 1.0 pA for mass spectra, ion images, and depth profiles using a lateral resolution of <10 µm.
- High-resolution images with a lateral resolution of ~200 nm and a target current of 100 fA
  - 256×256 pixels for images up to 500×500 μm^2
  - Stitch mode for images above 500×500 μm^2 using five frames per patch (one shot/pixel), total resolution of 1280×1280 pixels.
- Depth profiling over an analysis area of 200×200 μm^2 centered in a sputter area of 300×300 μm^2

- 30 nA of 3 keV Xe^+ was used as sputter ions.
- Electron bombardment (20 eV) was used to minimize charge built-up at the surface.
- Desorbed secondary ions were accelerated to 2 keV, mass analyzed in the flight tube, and post-accelerated to 10 keV before detection.
- Data evaluation was performed using the software suite SurfaceLab (version 6.7, build 83192) from ION-TOF GmbH.

2.5 X-ray diffraction

X-ray diffraction (XRD) is a technique used to analyze the crystal structure of crystalline materials. A monochromatic X-ray beam is shined onto the sample surface and the amount of reflected photons is typically monitored as a function of the incidence and reflection angle, either by varying both the source and detector angles (ϑ - 2ϑ scan) or by keeping the incident angle constant at a small angle (grazing incidence) and moving only the detector. The emitted photons will form constructive interference at angles that satisfy Bragg's law:

$$n\lambda = 2dsin\vartheta \tag{2.1}$$

where λ is the wavelength of the X-ray beam, n an integer number indicating the order of the reflection, d the distance between lattice planes and ϑ the already mentioned X-ray incidence angle in a ϑ - 2ϑ scan.

For diffraction on powders or polycrystalline samples, the sample is usually rotated in order to enhance the statistical variability of analyzed crystals. For single crystals and thin films, on the other hand, the samples are usually not rotated in order to avoid unnecessary vibrations that might affect the peak positions.

In this study, XRD was performed using a Bruker D8 diffractometer in ϑ - 2ϑ configuration. The measurements were used to identify the diffracting planes of the deposited thin films.

2.6 Atomic force microscopy and Kelvin probe force microscopy [33,34]

2.6.1 Atomic force microscopy

Atomic force microscopy (AFM), also called scanning probe microscopy (SPM), is a technique in which a sharp tip, with a 10-100 nm tip curvature radius, is scanned on the surface of the sample to be analyzed to obtain high-resolution surface topography images. The maximum obtainable lateral spatial resolution is determined by the tip radius, while the vertical resolution can be as low as single atomic layers.

In order to determine the topography of the sample, the scanning tip is mounted on a reflective cantilever on which a laser beam is shined. The reflection is then centered onto a segmented photosensitive diode, capable of recording small variations in the reflection angle. A schematic AFM setup is shown in the following Figure 2.4

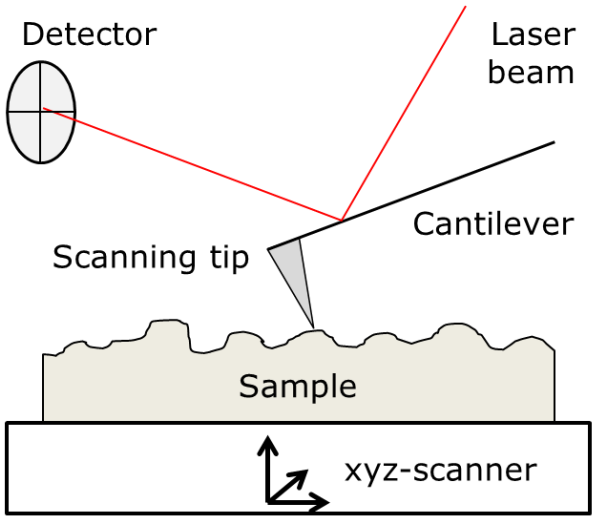

Figure 2.4. Schematic AFM setup

AFM can be performed in two main modes, namely contact and non-contact, with the intermediate variation of tapping mode.

In contact mode, the tip is brought close to the sample surface, until the tip-sample interactions cause the reflection spot to move in accordance with the spring constant of the cantilever. By adjusting the height of the sample with a feedback loop in order to keep the reflection position constant, the topography of the sample is obtained.

In non-contact and tapping mode, the cantilever is vibrated at its resonant frequency using a piezoelectric shaker. When the tip approaches the sample surface, the resonance frequency varies according to the tip-sample interactions, with a relationship that can be approximated with

$$\Delta f_0 = -\frac{f_0}{2k} \cdot \frac{\delta F_{TS}}{\delta z} \qquad 2.2$$

where f_0 is the resonance frequency of the cantilever, k its elastic constant, F_{TS} the tip-sample interaction and z the vertical direction. Being the resonant frequency shift proportional to the force gradient instead of the force, non-contact AFM offers a better sensitivity than contact AFM.

In this work, AFM was performed using a Danish Micro Engineering (DME) DualScope 95E microscope using non-contact mode. The probes used were NanoWorld Arrow NCR Si probes (tip radius <10 nm, resonant frequency 285 kHz), mounted on a specific holder developed by DME for the DualScope microscopes.

2.6.2 Kelvin probe force microscopy

One particular application of SPM which was used in this work is represented by Kelvin probe force microscopy (KPFM). It is a technique that originates from the Kelvin probe technique, where the work function of an unknown material is determined using another material of known work function. The two materials are brought into electrical contact, aligning thereby their Fermi levels, and form the two faces of a parallel plate capacitor. The difference in their work functions results in a potential difference between their surfaces, leading therefore to charge accumulation in the gap. By vibrating the two plates, the distance between them

varies and so does the capacitance of the system, leading to an oscillating current. A DC potential is applied to one of the plates, until no more current can be observed during the oscillation of the plates, meaning that the surface potential difference has been equilibrated. The equilibrium value, called contact potential difference (*CPD*) corresponds to the difference in work function between the two materials, and the work function of the unknown material can be determined.

In KPFM, the AFM tip represents one of the faces of the capacitor, making it possible to obtain a spatially resolved measurement of the local CPD. Instead of the current flowing through the system, the changes in the tip-sample interactions due to the electrostatic forces are monitored. In order to do so, a sum of a DC potential and an AC potential of small amplitude are applied to the cantilever vs. the sample, obtaining a similar effect to the vibration of the plates as in the Kelvin probe technique.

The tip-sample electrostatic interaction is given by

$$F_{el} = -\frac{1}{2}\frac{\delta C}{\delta z}\,\Delta V^2 \tag{2.3}$$

being F_{el} the electrostatic force, C the local capacitance between tip and sample and ΔV the total potential difference between the tip and the sample, which corresponds to

$$\Delta V = V_{DC} - V_{CPD} + V_{AC}\sin(\omega_{AC}t) \tag{2.4}$$

where V_{DC} is the applied DC voltage, V_{CPD} the CPD, V_{AC} the amplitude of the AC voltage and ω_{AC} its frequency.

By inserting this expression into equation 2.3, three main terms of the electrostatic force arise:

$$F_{DC} = -\frac{\delta C}{\delta z}\left[\frac{1}{2}\,(V_{DC} - V_{CPD})^2 + \frac{V_{AC}}{4}\right] \tag{2.5}$$

$$F_{\omega_{AC}} = -\frac{\delta C}{\delta z}\,(\mathrm{V_{DC}} - V_{CPD})V_{AC}\sin(\omega_{AC}t) \tag{2.6}$$

$$F_{2\omega_{AC}} = \frac{\delta C}{\delta z}\frac{{V_{AC}}^2}{4}\cos(2\omega_{AC}t) \tag{2.7}$$

In particular, F_{DC} can affect the topography signal; $F_{\omega AC}$ is the component of the electrostatic force at the AC frequency and is used to determine the correct CPD value and $F_{2\omega AC}$ is used for capacitance mappings [33,35].

Like in AFM, two main modes can typically be employed to perform KPFM, namely amplitude modulation (AM) and frequency modulation (FM). The two modes are thoroughly described in multiple studies, such as [35–38].

In AM mode the AC bias is applied close to the resonance frequency of the cantilever (typically 50-100 kHz), in order to use the enhancement of the oscillation provided by the resonance frequency and therefore minimize the necessary V_{AC}, and a lock-in amplifier is tuned to ω_{AC}, where it monitors the oscillation amplitude and compensates it by tuning V_{DC} until it matches V_{CPD}.

In FM mode, instead, the AC bias is applied at a low frequency (typically 1-3 kHz) to maximize the intensity of the electrostatic force and the frequency shift due to the electrostatic force is monitored. This can be compared with the non-contact SPM mode described by equation (1.2) and it results that the frequency shift due to the AC bias is proportional to the electrostatic force gradient.

In this work, KPFM was performed in AM mode, using a digital programmable waveform analyzer (DiProWA) manufactured by DME and conical Aspire CFM tips with a resonant frequency of 75 kHz. The DC potential difference was applied to the SPM probe vs the sample, which was appropriately grounded.

2.7 *In operando* scanning probe microscopy [39]

In order to characterize SOC materials in relevant operating conditions using SPM and KPFM, a novel tool was developed by DME for DTU Energy, the controlled atmosphere high temperature SPM (CAHT-SPM). In particular, two models were developed, namely CAHT-I and CAHT-II, the latter one representing an upgraded version that was used in this work.

CAHT-II, shown in Figure 2.5a, is equipped with a resistive furnace integrated in the alumina sample holder, capable of reaching 1000 °C. Additionally, the sample environment is sealed from the laboratory atmosphere and is equipped with an independent gas supply line connected to five mass flow controllers (MFC, Brooks 5850S, max flow 20 l/h N_2 equivalent), supplying O_2 (99.5% purity, AGA), compressed air, N_2 (grade 6 purity liquid N_2, AGA), CO_2 (99.8% purity liquid CO_2, AGA) and 5% H_2 in N_2 (mixed from 99.9% pure H_2 AGA). A liquid cooling system ensures the piezo actuators for the scanning stage never exceed the maximum operating temperature of 50 °C and cools down also the specially designed probe holder (Figure 2.5b and c), which is capable of hosting most commercial probes as well as homemade probes.

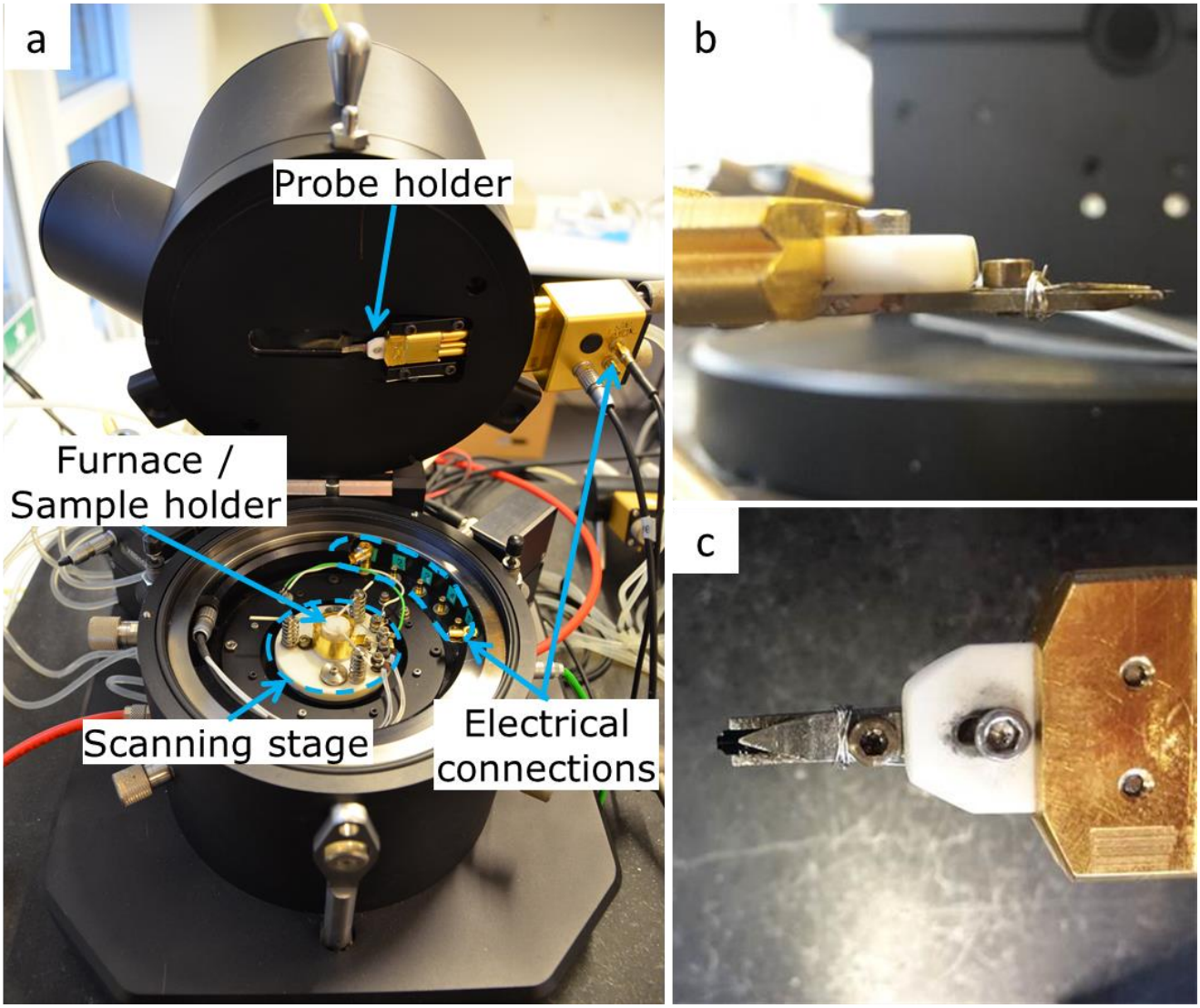

Figure 2.5. a) Overview of CAHT-II, b) close-up of the probe holder from the side and c) from the bottom.

Electrical connections can be established through dedicated pins to the sample and to the tip. These connections can be used to perform electrochemical measurements, local conductance mapping and KPFM, making the CAHT-II a versatile tool for the *in situ* characterization of SOC materials.

2.8 Electrochemical impedance spectroscopy [40,41]

EIS is a technique widely used in the analysis of both liquid and solid state electrochemical reactions. In EIS an oscillating voltage (or current) is applied across the sample with varying frequency, and the resulting (complex) current (or voltage) is monitored using a frequency response analyzer. The real and imaginary impedances for the whole range of investigated frequencies are typically plotted in a Nyquist plot, giving origin to features (arcs) that can be associated with separate processes/steps of the electrochemical reaction.

In this work, EIS was performed in dedicated rigs capable of operating at high temperature (up to 1000 °C) with a variety of available gases. The two rigs are shortly described.

One rig (rig-1) consisted of a vertical tube furnace with an alumina closed-end tube (99.9% purity, Degussit), which allowed the testing of four samples contemporarily. The samples were placed between two castellated alumina cylinders supporting a metallic mesh of Pt (mesh size 500 µm, 99.99% purity, CarboTech Nordic ApS, Denmark) or Au (mesh size 250 or 160 µm, 99.99% purity, CarboTech Nordic ApS, Denmark) and in some cases Ag foam (openings of ø 100-150 µm, MMC SuperAlloy corporation), and pressed down using zirconia weights (Figure 2.6a-b). In some experiments, porous 3 mol% YSZ pellets were inserted between the castellated alumina and the metallic meshes, in order to provide a better contact area without limiting the gas diffusion. A type-S thermocouple placed close to the samples allowed the determination of the actual sample temperature, while a YSZ-based pO_2 sensor measured the oxygen content in the sample environment. The four samples were electrically connected to a multiplexer, allowing the use of a frequency response analyzer (Solartron 1260) to test all four of them consecutively (Figure 2.6c). The gas supply was provided through MFCs (Brooks 5850S, max flow 6 l/h N_2 equivalent) and could be freely mixed between N_2 (grade 6 purity liquid N_2, AGA), O_2 (99.5% purity, AGA) and compressed laboratory air.

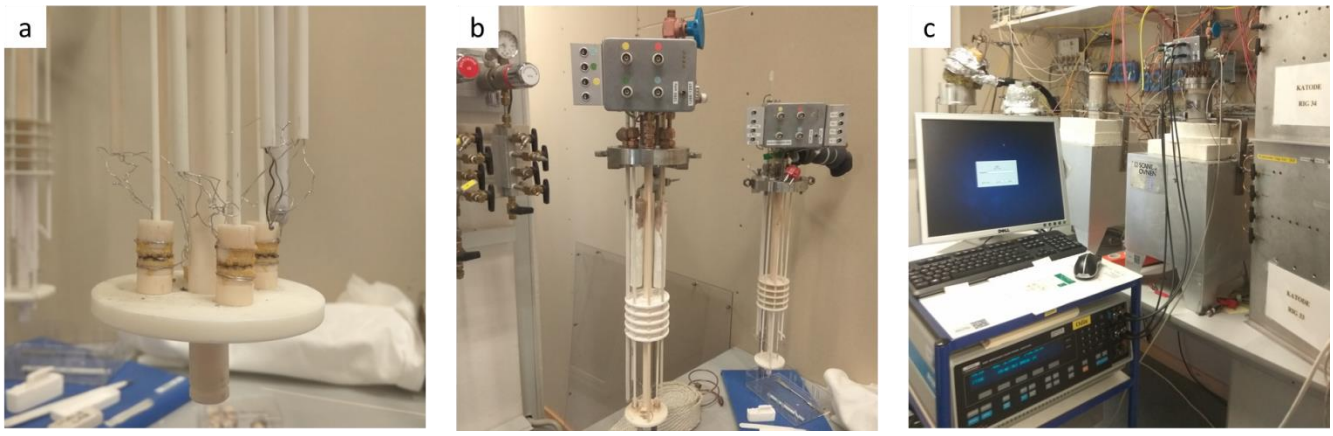

Figure 2.6. a) and b) sample holders for the four positions present in rig-1 and c) overview of the setup.

The second rig (rig-2) consisted of a horizontal Al_2O_3 tube furnace (99.8% pure Al_2O_3, Coorstek), with a single sample holder positioned in the center of the furnace. The sample was placed between two single crystal YSZ substrates (MTI corporation) wrapped in Au mesh (mesh size 300 µm, 99.99% purity, Alfa Aesar), providing the electrical contact, and pressed down with two Pt-Ir springs (99.999% purity, ESPI Metal). The springs themselves could also be used to provide a point electrical contact on small contact pads in the cases where buried Pt CC were used (Figure 2.7a). The impedance measurements were performed using a Biologic VSP-300. The gas supply was provided through MFCs (mks P4B, 5-5000 sccm N_2 equivalent), which controlled pre-mixed flows of 21% O_2 in Ar, 0.13% O_2 in Ar and pure Ar. Additionally, a diaphragm compressor (Thomas 107-series, Gardner Denver) was used to supply compressed laboratory air at 1.3 bar to the testing environment. This rig was also connected to a vacuum pump in order to routinely perform a bake-out in 10^{-5} mbar at 800 °C for 12-24 hours when humidity or other contaminants were introduced in the testing environment, for example through the compressed air feed. The complete rig can be seen in Figure 2.7b.

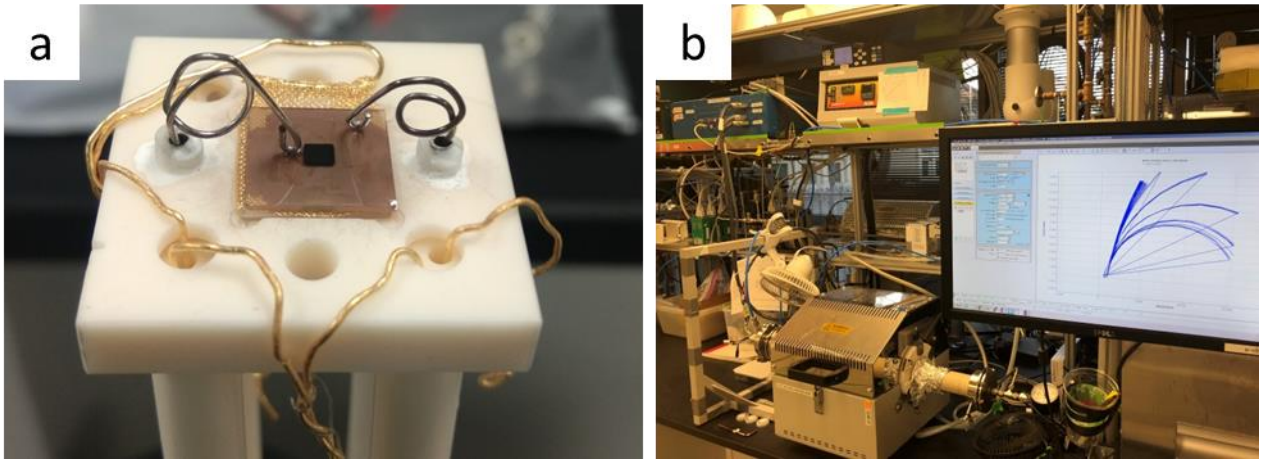

Figure 2.7. a) Sample holder in rig-2, shown in the spring-provided contact mode and b) overall view of the setup.

2.9 Near-ambient pressure X-ray photoelectron spectroscopy [42–44]

XPS is a technique primarily used for surface-sensitive chemical characterization in multiple applications. A monochromatic X-ray beam is directed onto the surface of the sample to be analyzed, and according to the photoelectric effect photoelectrons are generated and escape the sample from the outermost surface region. The photoelectrons are collected in a hemispherical electron analyzer, where they are sorted according to their kinetic energy.

Since the energy of the incident photons is known, the binding energy associated with the atoms found in the sample surface can be calculated, namely

$$E_B = h\nu - E_K - \Phi_{EA} \qquad 2.8$$

being E_B the binding energy of the electron, $h\nu$ the energy of the incident photons, E_K the measured kinetic energy of the electron and Φ_{EA} the work function of the electron analyzer.

Since the mean free path of the electrons in presence of gas molecules is limited, XPS is classically considered an ultra-high vacuum (UHV) technique with operating pressures of 10^{-9} mbar. The UHV conditions are not suitable for *in situ* studies of SOC materials, but recent advances using differentially pumped electron analyzers in synchrotron-based beamlines have allowed progressively higher pressures in the sample environment, resulting in the so-called near-ambient pressure XPS (NAP-XPS).

The NAP-XPS measurements described in this work were conducted at the 11.0.2 beamline of the Advanced Light Source (ALS) at the Lawrence Berkeley National Lab. The beamline uses differential pumping to allow XPS measurements at pressures up to maximum 10 mbar. The X-ray beam shines onto the sample at 45°, illuminating an area of 100·50 μm^2. The sample is placed at the optimal distance from the analyzer cone to maximize the number of photoelectrons entering it. The beam brilliance depends on the selected energy, and in the range of energies that was used was between 10^{18} and 10^{19} photons/(s·mm^2·mrad^2·0.1%BW). The term 0.1%BW refers to the fact that only the photons falling within a bandwidth of 0.1% of the selected energy are counted.

The sample holder, shown in Figure 2.8a, is equipped with four independent electrical contacts. Two-electrode electrochemical measurements were performed with an externally connected Biologic SP-240, while the other two contacts were used to operate a resistive Al_2O_3 heater. Since it was impossible to connect any kind of thermometric element in the setup, the series resistance measured during EIS was used to calibrate the temperature. In order to avoid short-circuits, Al_2O_3 plates or tubes were used between the metallic components and the sample or the holder.

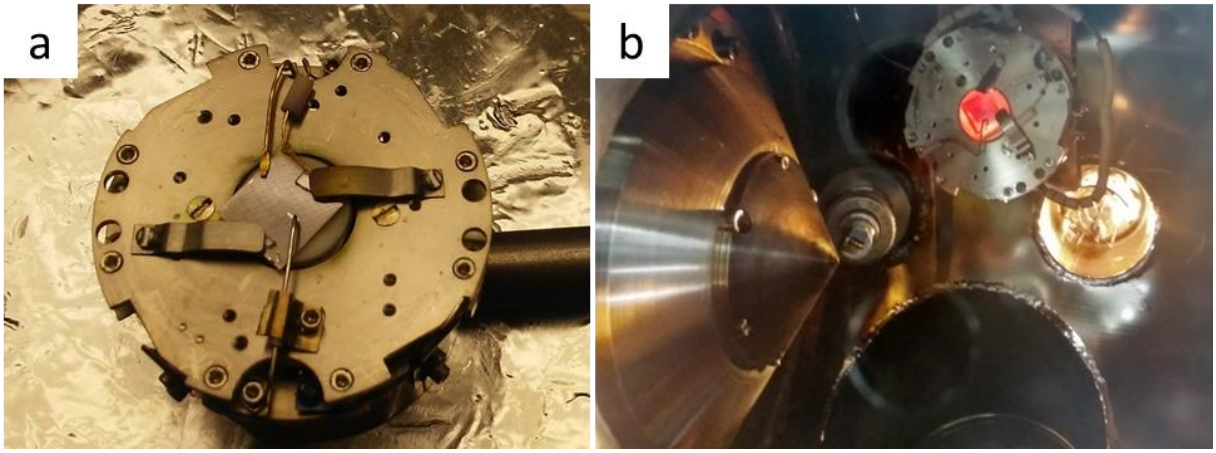

Figure 2.8. a) Sample holder used at the 11.0.2 beamline of the ALS and b) sample holder inside the experimental chamber (not in measuring position).

2.10 Near-ambient pressure scanning photoemission microscopy [45–48]

One further development of XPS enabled by the high brilliance and coherence of synchrotron X-ray sources is represented by SPEM. The working principle is the same as XPS, but the X-ray beam is focused onto a 120 nm spot on the surface of the sample using a zone plate coupled with an order-sorting aperture. The sample can therefore be scanned with the X-ray beam, obtaining spatially resolved XPS spectra, which can for example be used to obtain elemental maps. Due to the additional optics in the SPEM chamber, the use of a differentially pumped analyzer like in NAP-XPS is not possible for SPEM, but different approaches are used in this case in order to increase the operating pressure.

The ESCA Microscopy beamline of the Elettra synchrotron at Trieste offers a newly developed sealed cell with two pinholes, for the entering X-ray beam and for the exiting photoelectrons (Figure 2.9) [48]. The cell, named near-ambient pressure cell (or shortly NAP-cell) is connected to an external gas line providing the desired atmosphere. Relying on the vacuum pumps of the experimental chamber to pump the small quantity of gas exiting through the pinholes, a static pressure of around $5 \cdot 10^{-2}$ mbar is obtainable inside the NAP-cell, without exceeding the technical limit of $1 \cdot 10^{-5}$ mbar inside the experimental chamber. In this case, the X-ray beam enters the sample perpendicularly and the photoelectrons are collected from a cone at a 30° angle ±10° acceptance, thereby improving the surface sensitivity. The NAP cell is also equipped with four electrical connections, of which two were used for the electrochemical measurement and two to power a ceramic heater. As was done in the ALS beamline, the series resistance measured with EIS was used as a temperature calibration.

SPEM was used in two modes for this work, namely spectromicroscopic and microspectroscopic mode. In the first mode, an energy range is selected at the electron analyzer and the sample is scanned with the X-ray beam. For each point of the scan, a 48-channel segmentation of the selected photoelectron energy range is acquired simultaneously. By doing this, a photoelectron spectrum with an energy resolution better than 200 meV is obtained for each point. In the second mode, a point on the surface is selected and a complete XPS spectrum can be acquired. This allows acquisition of spectra of features that can be seen in the first mode with a much higher signal-to-noise ratio and the same energy resolution range.

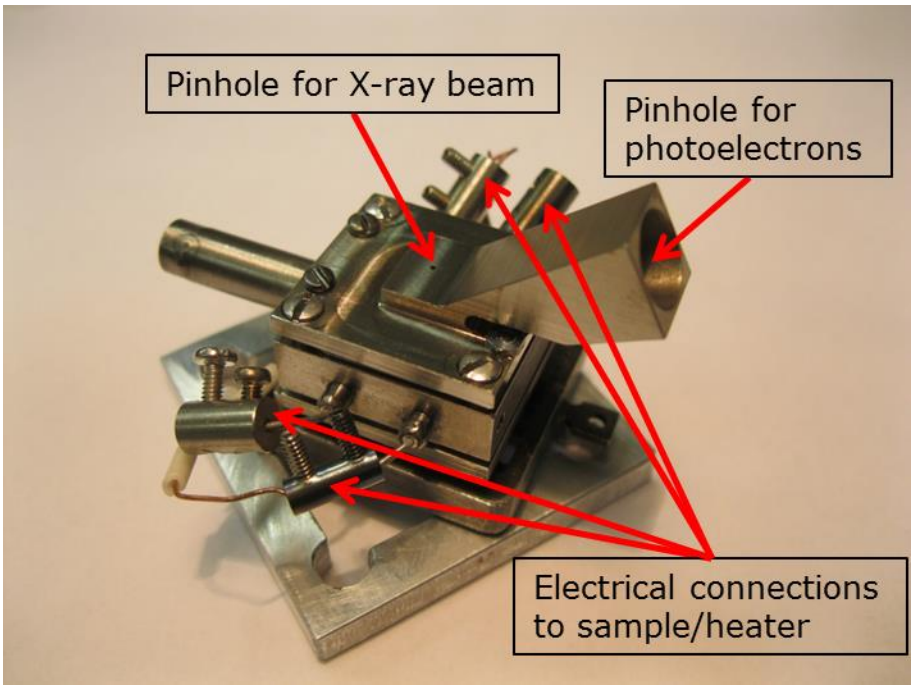

Figure 2.9. NAP-cell used for SPEM experiments.

3 Influence of testing parameters on the EIS response of LSCF thin films

3.1 Introduction

SOCs represent an efficient energy conversion technology, with the possibility of running on a variety of fuels, for example H_2 and H_2/CO mixtures, and even on natural gas. In order to perform efficiently, however, they require operating temperatures of 600-800 °C, which accelerates thermally activated degradation mechanisms and can promote unwanted side reactions between the components of the cells. For this reason, materials with higher ionic and/or electronic conductivities and better catalytic activity towards the oxygen/hydrogen evolution/incorporation reactions are investigated, aiming for higher efficiency, lower operating temperatures and prolonged life for SOCs.

The perovskite (La,Sr)(Co,Fe)O_3 (LSCF), represents the state-of-the-art oxygen electrode material for SOCs and has been studied extensively in the past decades. While the bulk properties of LSCF, like conductivity, oxide ion diffusion and oxygen nonstoichiometry are well-established as function of temperature and oxygen partial pressure [19–21,23,49–52], surface oxygen exchange coefficient data from different literature sources present a scatter of approximately three orders of magnitude, and are often lacking pO_2 dependence [24,25,61,62,53–60].

For the determination of surface oxygen exchange activity, three main techniques are typically employed, namely EIS, electrical conductivity relaxation (ECR) and O^{16}/O^{18} isotope exchange combined with depth profiling. For all three of them, an accurate measurement of the active microscopic surface area is required, given the interfacial nature of the oxygen reactions. Dense samples or thin films are best suited for performing such measurements, but it is possible to generalize the study to porous structures, provided the active surface is known.

The three different techniques provide three different measures of the surface exchange coefficient, which can be correlated to each other. EIS provides the surface exchange resistance, R_{surf} as an area-specific resistance (ASR) in Ωcm^2, ECR provides the chemical exchange rate constant k_{ex} in cm·s^{-1} and O^{16}/O^{18} exchange provides the oxygen exchange rate constant k_O in cm·s^{-1}. The correlations between the three quantities have been established, and the following equations can be used to convert between k_{ex}, k_O and R_{surf} [54,63,64]:

$$R_{surf} = \frac{RT}{4F^2 k_O c_O} \tag{3.1}$$

and

$$k_O = \frac{k_{ex}}{\Gamma_O} \tag{3.2}$$

where R is the universal gas constant, T the absolute temperature, F the Faraday constant, c_O the lattice concentration of oxygen, and Γ_O is the thermodynamic factor of oxygen.

In order to establish a comparison with the measurements that will be performed in this study on model electrodes, only literature studies performed on model systems, meaning thin films and dense samples, were collected and compared. Using the k_O and k_{ex} values reported in [54], and extrapolating them from the original range of 625-750 °C to 500-900 °C, Γ_O was calculated from equation 3.2 for all necessary temperatures, in order to convert k_O and k_{ex} values from available literature sources [24,25,61,62,53–60] to corresponding R_{surf} values. A compilation of all the deduced R_{surf} values is provided in the plot of Figure 3.1.

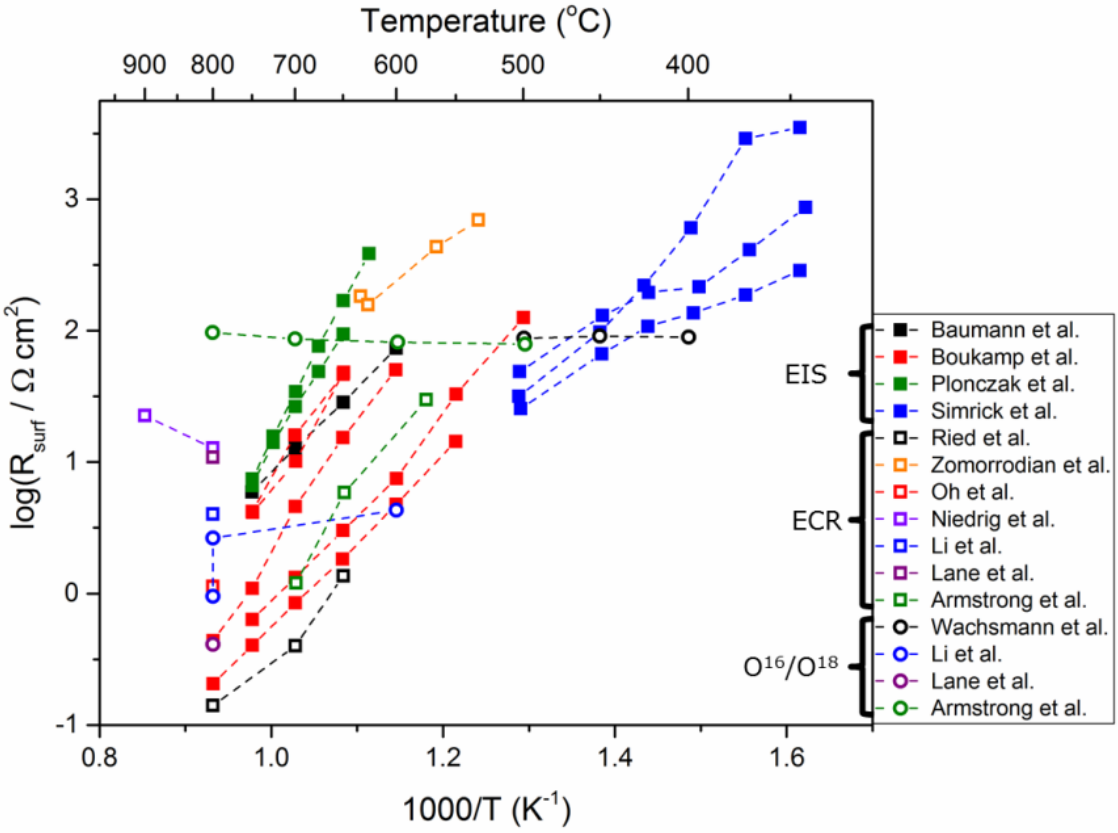

Figure 3.1. Compilation of LSCF R_{surf} values reported in the literature [24,25,61,62,53–60]**.**

Very scattered surface resistance data could be observed within all datasets, resulting in a range of three orders of magnitude, with activation energies ranging from 0.9 to 2 eV (excluding the datasets with apparently null or negative activation energies) and pO_2 exponents (where reported) between -0.15 and -0.5. It is clear that the oxygen surface exchange activity is drastically influenced by the experimental conditions used in the testing procedure and that the intrinsic oxygen surface exchange activity of LSCF remains largely undetermined. It is therefore crucial to identify the parameters that may cause this scatter. Some parameters will affect the data obtained by all the examined techniques, whereas others will only be relevant for EIS studies, especially those performed on model thin film electrodes.

For example, poor current collection can lead to an underestimation of the performance [65,66], whereas active CCs can stimulate a response which is better than the one of the material under study [67,68]. On the other hand, the CCs, the testing setup and the gaseous environment can introduce impurities (S, H_2O, SiO_2, Cr, salts etc.) that poison the electrode surfaces, causing a fast degradation [53,69–72]. Moreover, the electrodes can react with the electrolyte material, and form secondary phases (for example $SrZrO_3$ and $La_2Zr_2O_7$) [73]. At the same time, also impurities present in the electrode materials (like Cr, Si, Na, etc.) can segregate to the surface, which is accelerated at high temperature. Finally, the stoichiometry of the films can also play an important role, both in terms of activity and in terms of stability. It is known, for example, that A-site deficient perovskites will be less susceptible to Sr-segregation and therefore show less degradation[74].

The parameters that will be explored in this study can be summarized as follows:

i) Electrode properties:
   (1) Electronic sheet resistance
   (2) Stoichiometry
   (3) Impurities in electrode material
   (4) Segregation and precipitation
ii) CC properties
   (1) Current collection geometry
   (2) Impurities from current collection
iii) Atmosphere properties
   (1) Impurities from gas

Given the large number of variables and the possible correlations between them, a large set of experiments were undertaken in different atmospheres, with different CCs and using different starting materials and film thicknesses, and the effect on the impedance response was analyzed. Most of the studies were performed on dense LSCF thin films with the nominal composition $La_{0.58}Sr_{0.4}Co_{0.2}Fe_{0.8}O_3$, except in few sub-studies, where $La_{0.61}Sr_{0.39}FeO_3$ (LSF) was used.

3.2 Sample preparation

Dense thin perovskite films were deposited by PLD on single crystal double-side polished yttria-stabilized zirconia (YSZ) substrates with (100) orientation. The chosen dimensions were 10x10x0.5 mm^3. All LSCF films were deposited on 9.5 mol % YSZ substrates (9.5YSZ) supplied by Crystal GmbH (Germany), while the LSF films were deposited on 8 mol % YSZ (8YSZ) substrates supplied by MTI Corp (USA).

The thin films were deposited using two different PLD systems; one from Surface (Germany) and one from PVD (USA), both equipped with a Kr-F excimer laser (Coherent, USA). A complete list of samples, listing materials, thicknesses and geometries, is found in Table 3.1. The depositions were carried out at 600 °C for LSCF and 650 °C for LSF at a laser fluency of approximately 1.8-4 J/cm^2, with 0.01 mbar O_2 and a pulse frequency of 20 Hz for samples LSCF_01-08 and $6.7x10^{-3}$ mbar O_2 and a pulse frequency of 10 Hz for samples LSCF_09-11 and LSF_01-07. The target-sample distance was 60-70 mm. In some cases (LSCF_09/09b and LSF_01-05), Inconel shadow masks (ESPI metal, Fotofab) were used to produce films over smaller areas.

On the samples where a buried Pt CC grid was sputtered before the final LSCF layer was deposited, the spacing between Pt stripes was 30 µm in one direction and 300 µm in the other, and the stripes were 5 µm wide.

Table 3.1. List of samples produced and analyzed in the present study. SC stands for symmetric cell.

Name	Electrode geometry	Layer compositions and thicknesses
LSCF_01/01b	8x8 mm^2 SC	LSCF-A (70 nm)/GDC(140 nm)/9.5YSZ/GDC(140 nm)/LSCF-A (70 nm)
LSCF_02	8x8 mm^2 SC	LSCF-A (420 nm)/GDC(100 nm)/9.5YSZ/GDC(100 nm)/LSCF-A (420 nm)
LSCF_03	8x8 mm^2 SC	LSCF-A (600 nm)/GDC(80 nm)/9.5YSZ/GDC(80 nm)/LSCF-A (600 nm)
LSCF_04	8x8 mm^2 SC	LSCF-B (600 nm)/GDC(80 nm)/9.5YSZ/GDC(80 nm)/LSCF-B (600 nm)
LSCF_05	8x8 mm^2 SC	LSCF-A (450 nm)/GDC(175 nm)/9.5YSZ/GDC(175 nm)/LSCF-A (450 nm)
LSCF_06	8x8 mm^2 SC	
LSCF_07	8x8 mm^2 SC	
LSCF_08	8x8 mm^2 SC	
LSCF_09/09b	2x2 mm^2 WE with buried Pt CC, 8x8 mm^2 CE	LSCF-A (300 nm)/SDC(20 nm)/9.5YSZ/SDC(20 nm)/Pt (140 nm)/LSCF-A (300 nm)
LSCF_10	8x8 mm^2 SC with buried Pt CC	LSCF-B (300 nm)/Pt (100 nm)/SDC(20 nm)/9.5YSZ/SDC(20 nm)/Pt (100 nm?)/LSCF-B (300 nm)
LSCF_11	8x8 mm^2 SC	LSCF-B (300 nm)/SDC(20 nm)/9.5YSZ/ SDC(20 nm)/LSCF-B (300 nm)
LSF_01	1x1 mm^2 SC	LSF (300 nm)/SDC(20 nm)/9.5YSZ/ SDC(20 nm)/LSF (300 nm)
LSF_02	2x2 mm^2 SC	
LSF_03	4x4 mm^2 SC	
LSF_04	3x3 mm^2 SC	
LSF_05	4x4 mm^2 SC	
LSF_06	8x8 mm^2 SC	
LSF_07	8x8 mm^2 SC	

3.3 Overview of experimental parameters

To provide a better overview of the large set of experiments undertaken, these are divided here into five main study-lines:

E-1. Influence of current constriction in the thin films

- E-1.1. Use of metallic CCs with decreasing spacing on LSCF_01 sample (70 nm film) – rig-1, compressed air
- E-1.2. Use of metallic CCs with decreasing spacing on thicker films (450-600 nm - LSCF_02-05,08) and metallic pastes on 450 nm films (Au paste on LSCF_06 and Pt paste on LSCF_07) – partially rig-1, compressed air and rig-2, synthetic air
- E-1.3. Use of buried Pt CCs (LSCF_09) – rig-2, synthetic air

E-2. Influence of the CC

- E-2.1. Activity of Ag foam on YSZ pellet without any electrodes – rig-1, compressed air
- E-2.2. Comparison between the performance of samples LSF_01-03, tested with Au mesh, and samples LSF_04-05, tested with Pt mesh with the same spacing – rig-2, synthetic air
- E-2.3. Comparison between the performance and the impurity levels of samples tested with only Au mesh (LSCF_05) and with the addition of Au paste (LSCF_06) and Pt paste (LSCF_07) – rig-1, compressed air
- E-2.4. Comparison between the performance of samples with buried Pt pattern (LSCF_09-10) and without buried Pt pattern (LSCF_11) – rig-2, synthetic air

E-3. Influence of gas quality

- E-3.1. Testing of samples LSCF_02-04 and observation of their degradation
- E-3.2. Testing of sample LSCF_08 in both synthetic and compressed air and monitoring of its performance – rig-2
- E-3.3. Testing of sample LSF_06 in synthetic air and LSF_07 in compressed air and comparison between their impurity levels – rig-2

E-4. Influence of electrode size, using samples LSF_01-03 with the same Au CC

E-5. Influence of stoichiometry and target impurities, by comparing the performance of samples LSCF_09 and LSCF_10, tested in synthetic air in rig-2, and samples LSCF_03 and LSCF_04 in compressed air in rig-1.

3.4 Results

3.4.1 Characterization of pristine samples

3.4.1.1 SEM for microstructural characterization

The polished cross-section of the LSCF_01b sample was examined using SEM in order to evaluate the microstructure of the thin films after deposition and to measure the layer thicknesses. Conventional physical vapor deposition techniques, such as sputtering, generally produce films with columnar microstructures [75–77], but the use of PLD with an accurate tuning of the deposition parameters enables the deposition of well-defined epitaxial films, meaning that the crystal structure of the film adapts to the one of the substrate in presence of a small lattice mismatch [78–80]. In the in-lens image the layers appeared dense and continuous, without any indication of columnar structures, as seen in Figure 3.2a. Nevertheless, the presence of the carbon coating on top of the sample and the low thickness of the deposited films do not allow reaching this conclusion with absolute certainty. The backscattered electron image, shown in Figure 3.2b showed clear compositional contrast between the layers.

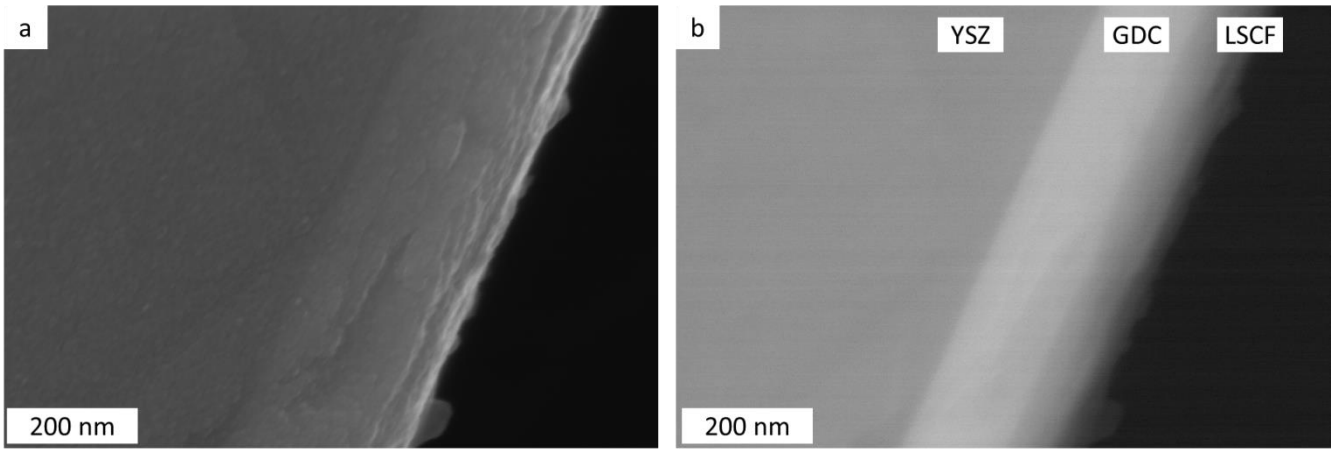

Figure 3.2. Polished cross-section of the pristine LSCF_01b sample. a) image acquired with the in-lens detector, showing a dense microstructure, and b) image acquired with the backscattered electron detector, where clear compositional contrast between the three layers can be observed.

After testing, cross-sections of the thicker LSCF_03 and LSCF_06 samples were also investigated. The in-lens images acquired on these samples, shown in Figure 3.3, suggest again dense layers without indications of columnar growth.

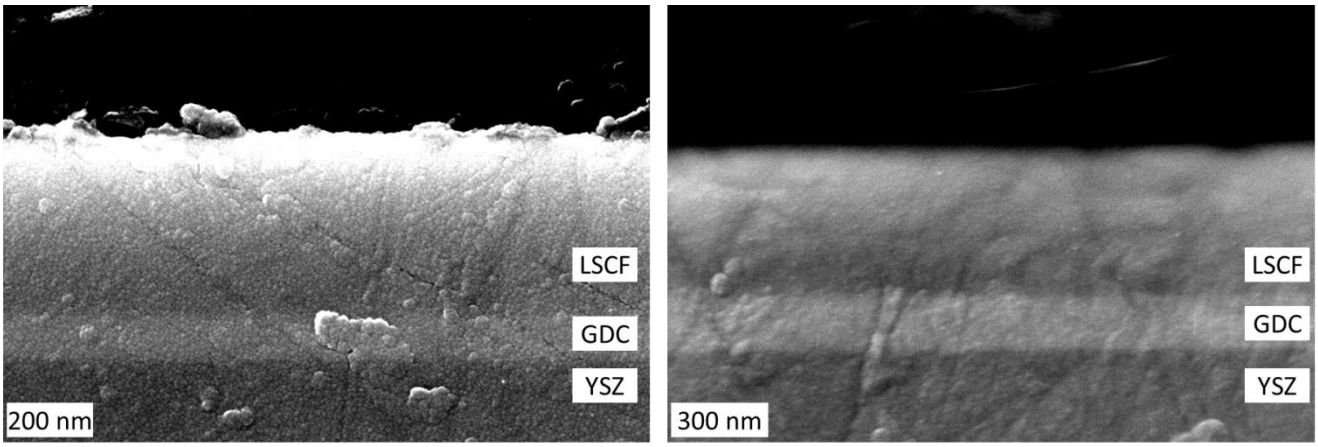

Figure 3.3. In-lens images of the polished cross-sections of a) the LSCF_03 sample and b) the LSCF_06 sample after testing, showing a dense microstructure and compositional contrast.

3.4.1.2 XRD for lattice matching

In order to verify the expectation of an epitaxial deposition, XRD was also performed on the LSCF_01b sample. As can be seen in Figure 3.4, the diffractogram clearly shows lattice planes corresponding to the (100) orientation of the YSZ single crystal, ceria and LSCF. The lattice parameters of YSZ and GDC have a mismatch of 5.5 %, therefore the "cube on cube" epitaxial growth of GDC on the YSZ substrates is expected [81]. For the LSCF perovskite family around the used stoichiometry, on the other hand, two main crystal structures are observed in literature with powder diffraction, namely rhombohedral and cubic, with a transition from rhombohedral to cubic for La-content on the A-site below 0.5 [82]. However, a cubic symmetry was also observed for powders with the $La_{0.6}Sr_{0.4}Co_{0.8}Fe_{0.2}O_3$ composition at high temperature [83]. Previous studies performed on PLD films show a good compatibility between fluorites (YSZ and GDC) and cubic perovskites, the crystal structures being rotated by 45° in order to accommodate the lattice mismatch between them[81,84].

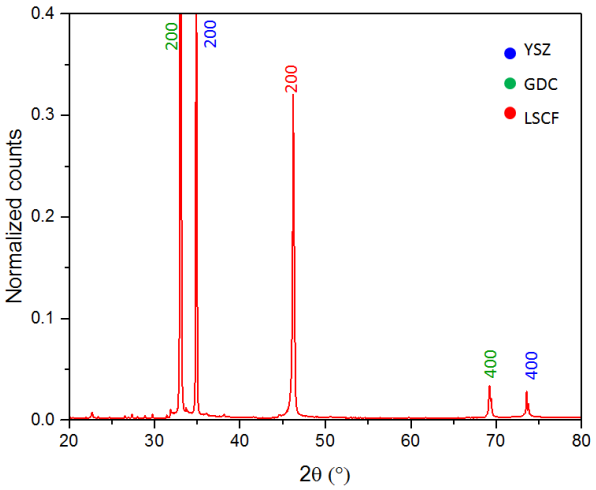

Figure 3.4. Diffractogram of the pristine LSCF_01 sample.

3.4.1.3 AFM for surface roughness measurements

Figure 3.5 shows an AFM image of the LSCF_09b, measured on the CE side. The surface does not exhibit features that point to a columnar microstructure, which indicates epitaxial growth. The mean square root surface roughness (Sq) was calculated with the Scantool software to be 0.4 nm.

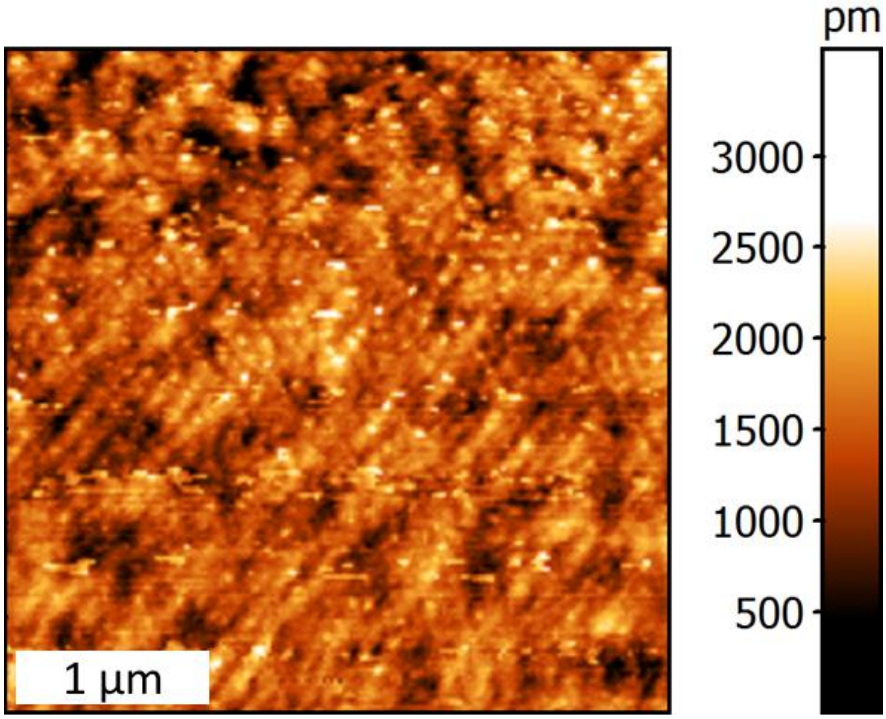

Figure 3.5. AFM image of the surface of the pristine CE of the LSCF_09b sample.

3.4.1.4 ToF-SIMS analysis for surface impurities

The CE side of the pristine LSCF_09b sample was also imaged with ToF-SIMS. Figure 3.6 shows 8x8 mm^2 ion images of F, Cl, Na and K which were the main impurities on the sample. F and Cl were present on the LSCF surface while Na and K were present on the YSZ surface not covered by the GDC/LSCF layers. Traces of S could only be seen when imaging smaller areas, as the signal was too weak to be distinguished on a full scale image.

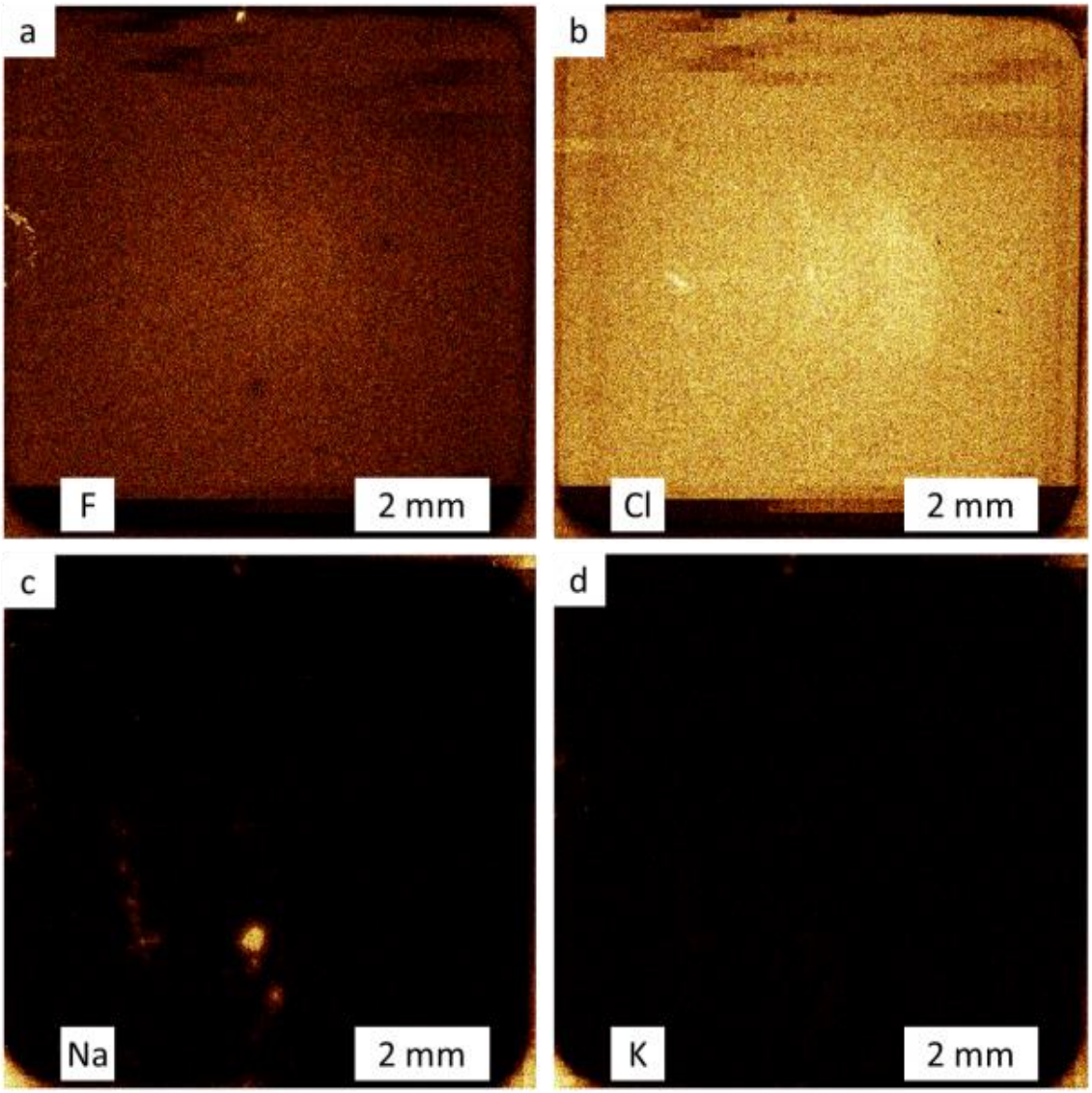

Figure 3.6. ToF-SIMS F, Cl, Na and K ion images of the pristine CE of the LSCF_09b sample. Brighter colors signify a higher signal for the identified element.

3.4.1.5 GDMS and ICP-MS of electrode materials

The LSCF-A powder was analyzed with GDMS, exhibiting traces of Cr (70 ppm), S (230 ppm), Cl (300 ppm) and Si (55 ppm). The complete list of elements is found in Table 3.2.

The stoichiometry of the samples was investigated with ICP-MS, showing a 4 % A-site deficiency in the LSCF-A case, where a 2% A-site deficiency was intended, and a 2% A-site excess in the LSCF-B case, where stoichiometric composition was intended. Both the Sr and the Co content were closer to the desired values of respectively 0.4 and 0.2 in the LSCF-A case than they were in the LSCF-B case, as can be seen in Table 3.3.

Table 3.2. GDMS results of the LSCF-A powder.

Element	Concentration [ppm/wt%]	Element	Concentration [ppm]	Element	Concentration [ppm]
Li	0.32	**Ga**	-	**Nd**	-
Be	-	**Ge**	-	**Sm**	-
B	-	**As**	-	**Eu**	-
C	-	**Se**	-	**Gd**	-
N	-	**Br**	-	**Tb**	-
O	Matrix	**Rb**	<0.1	**Dy**	-
F	<0.5	**Sr**	Matrix	**Ho**	-
Na	57	**Y**	-	**Er**	-
Mg	95	**Zr**	-	**Tm**	-
Al	71	**Nb**	-	**Yb**	-
Si	55	**Mo**	-	**Lu**	-
P	27	**Ru**	-	**Hf**	9.5
S	230	**Rh**	-	**Ta**	-
Cl	300	**Pd**	-	**W**	-
K	2.7	**Ag**	-	**Re**	-
Ca	~0.36wt%	**Cd**	-	**Os**	-
Sc	0.22	**In**	Binder	**Ir**	-
Ti	13	**Sn**	-	**Pt**	-
V	0.95	**Sb**	-	**Au**	-
Cr	70	**Te**	-	**Hg**	-
Mn	490	**I**	<0.5	**Tl**	-
Fe	Matrix	**Cs**	-	**Pb**	0.65
Co	Matrix	**Ba**	160	**Bi**	<0.01
Ni	63	**La**	Matrix	**Th**	-
Cu	16	**Ce**	-	**U**	-
Zn	-	**Pr**	-		

Table 3.3. ICP-MS comparison of films deposited with the two different LSCF targets.

Target	LSCF-A	LSCF-B
A/B	0.959±0.008	1.02±0.03
Sr/(La+Sr)	0.404±0.001	0.389±0.002
Co/(Co+Fe)	0.214±0.003	0.157±0.007

3.4.2 Influence of various parameters on surface exchange of LSCF films

The outcome of the set of experiments described in 3.3 will be described in detail in the following sections, both in terms of electrochemical performance of the samples, as evaluated from their EIS spectra, and of post-mortem chemical analysis.

Before discussing the results of the EIS measurements, a brief summary of the parameters used in the fitting of the spectra is provided. In analogy with [24,54,55], most spectra exhibited a high frequency (HF) series resistance (R_S) associated with the YSZ electrolyte, an intermediate frequency (MF) arc associated with an interfacial resistance (R_I), and a low frequency (LF) arc associated with the R_{surf} of the thin films, as can be seen in Figure 3.7. For the MF and LF arcs, constant phase elements were used in the equivalent circuit model employed for the fitting.

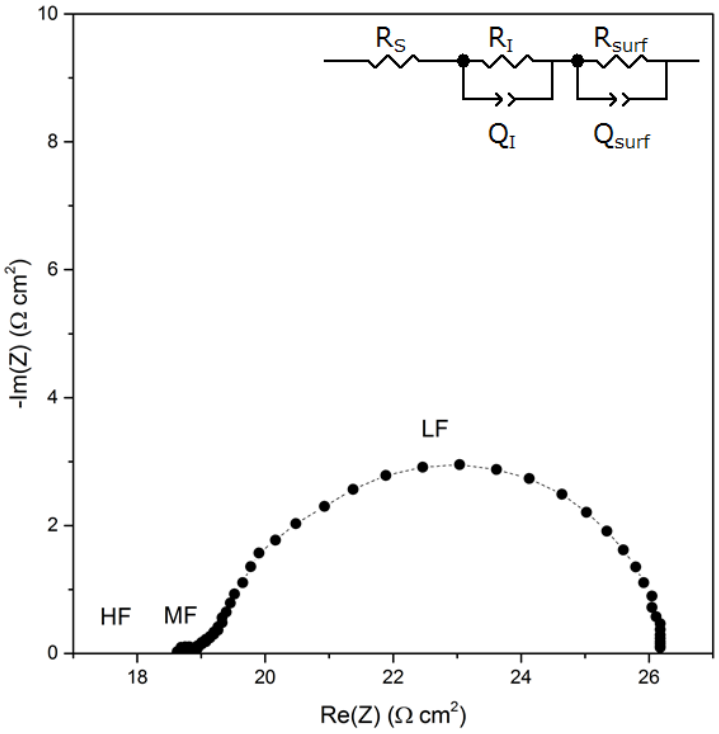

Figure 3.7. Typical EIS spectrum for the investigated SCs and the equivalent circuit used for fitting.

In some cases, the MF arc was too poorly resolved to be fitted, and therefore only the R_S and the R_{surf} arcs were used in the fitting. In particular, the interfacial resistance arc was too small to be resolved in the cases where a high R_{surf} arc was present. Since its contribution was between 5-10 % in the cases where it could be resolved, its contribution was considered negligible for the other cases, where the measured R_{surf} was 10-100 times higher. The combined outcome of the complete set of experiments, shown in Figure 3.8, exhibits a scatter of three to four orders of magnitude with respect to R_{surf}, and in that sense was not unlike the scatter evidenced in the literature compilation of Figure 3.1, where a scatter of about three orders of magnitude could be seen. The activation energies derived from the experimental data varied between 0.75 and 2 eV in 21% O_2.

The pO_2 exponents for the R_{surf} at 600 °C were also evaluated in most of the cases, resulting in values between -0.3 and -0.8. These ranges are closely matched to the ones obtained from the available literature data.

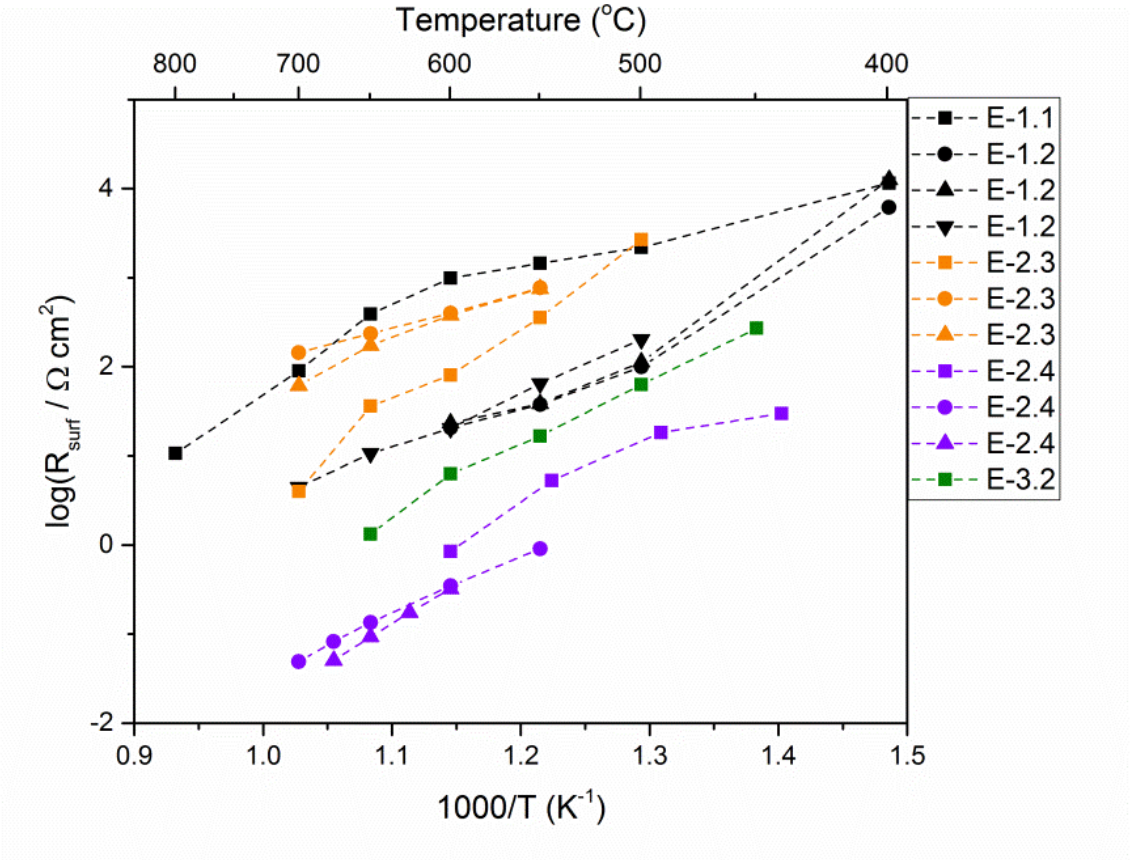

Figure 3.8. Summary of Arrhenius plots for the R_{surf} of LSCF (100) thin films collected in the performed set of experiments.

3.4.2.1 Influence of current constriction in the thin films

One of the challenges when characterizing thin films electrochemically is the possible contribution from the electronic sheet resistance of the film. This can result in a smaller electrochemically active area than the geometrical area of the film, if the spacing between contact points of the CC is too large compared to the film thickness. To assess the significance of current constriction, the R_S values obtained from the testing of samples with different film thicknesses, using different CCs, were evaluated.

In the first sub-study (E-1.1), CCs with varying spacing, namely a platinum mesh with a spacing of 500 µm, a gold mesh with a spacing of 250 µm and a piece of silver foam with openings of 100-150 µm were used on the LSCF_01 sample. At 600 °C, the expected R_S for the used YSZ single crystals is 8-10 Ωcm^2; the measured values for the different cases and their deviation from literature are reported in Table 3.4. The deviation from the literature values decreased progressively with decreasing contact point spacing.

In the second sub-study, the Au mesh and the Ag foam were also used as CCs on thicker LSCF films (450 and 600 nm), to examine the effect of film thickness. Furthermore, Pt and Au pastes were also used as a means of increasing the contact area. In all cases the R_S reached values closer to literature in the whole temperature range, suggesting that the current constriction was negligible under these conditions.

Finally, in the third sub-study, a buried Pt CC was evaluated as an alternative to the use of fine meshes and conducting pastes for current collection. The resulting R_S values appeared to be even lower than the ones measured on the other samples. The geometry of the samples with buried CC, however, was not symmetric. The current distribution in the YSZ single crystal is therefore difficult to estimate, and the normalization over the WE area will lead to an underestimation of the ASR.

All the results of these first three sub-studies are shown in Figure 3.9, together with literature values derived from [85–87]. The results from E-1.1 are shown in red, the ones from E-1.2 in blue and those from E-1.3 in black. The deviation of the values at 600 °C was also calculated and summarized in Table 3.4.

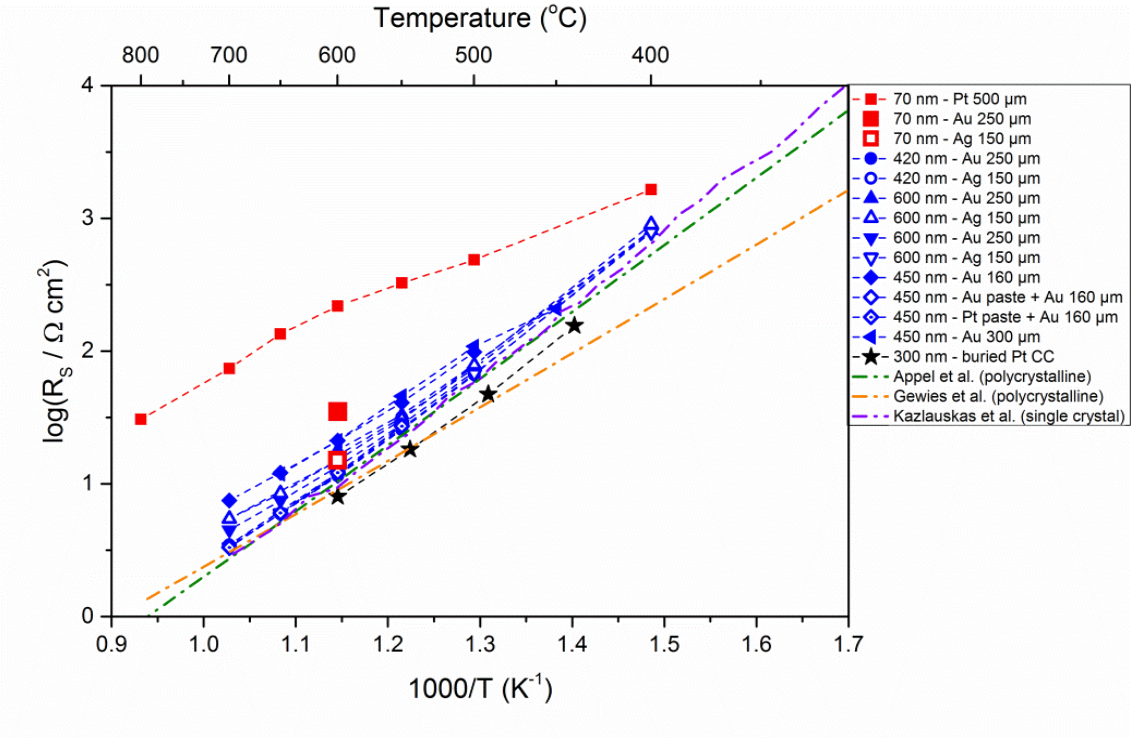

Figure 3.9. Summary of measured YSZ series resistances in air for different CC spacings, film thicknesses, and CC materials, compared with literature values from [85–87]**.**

Table 3.4. Deviation from literature value at 600°C from [50] for all examined cases.

Case	R_S at 600 °C	$\frac{R_S - R_{S,lit}}{R_{S,lit}}$ at 600 °C
70 nm – Pt 500 µm	217.76	22.62
70 nm – Au 250 µm	36.90	3.00
70 nm – Ag 150 µm	15.81	0.71
420 nm – Au 250 µm	16.37	0.78
420 nm – Ag 150 µm	11.49	0.25
600 nm – Au 250 µm	18.01	0.95
600 nm – Ag 150 µm	15.04	0.63
600 nm – Au 250 µm	13.50	0.46
600 nm – Ag 150 µm	11.78	0.28
450 nm – Au 160 µm	21.13	1.29
450 nm – Au paste + Au 160 µm	12.00	0.30
450 nm – Pt paste + Au 160 µm	12.10	0.31
450 nm – Au 300 µm	21.11	1.29
300 nm – buried Pt CC	8.02	-0.13

3.4.2.2 Influence of CC

In the first study, various current collection approaches were compared with respect to their current collection efficiency as a function of their spacing. The CC itself and its method of application can also interact with the thin film in different ways. For this reason, the potential spurious contribution of the CC to the measured electrochemical activity and the impact of CC choice to the near surface chemistry of the thin film were further investigated in order to explore potential artifacts and to arrive at a reliable current collection strategy.

3.4.2.2.1 Ag foam as a CC

The samples measured with silver foam showed R_S values close to literature even for the thinnest film thickness of 60-70 nm (LSCF_01). However, silver is known to be a good oxygen exchange electrocatalyst on its own [24,88]. Indeed, Ag foam showed substantial activity for oxygen exchange in multiple sets of experiments, both with and without LSCF thin films. A SC of Ag foam/YSZ/Ag foam resulted in a R_{surf} of 250 Ωcm^2 at 600 °C in air. This value is smaller than the R_{surf} of LSCF films exposed to severe degradation conditions and can therefore introduce a substantial error. Based on this observation, Ag in any form should be avoided as a CC, especially in the case of films with high R_{surf} values.

3.4.2.2.2 Pt and Au meshes

To assess the influence of Au and Pt meshes, time-resolved degradation measurements were performed on the LSF_03 and LSF_05 samples. These were tested in synthetic air at 650 °C in the same rig using either Pt or Au mesh with the same spacing of 300 µm. As Figure 3.10 shows, the sample tested with Au

mesh activated markedly over the first 5 h and gradually stabilized to a R_{surf} value of 8 Ωcm^2, whereas the sample tested with the Pt mesh showed pronounced deactivation during the first 5 h and progressive decrease of the degradation rate over time, approaching a R_{surf} value of 100 Ωcm^2.

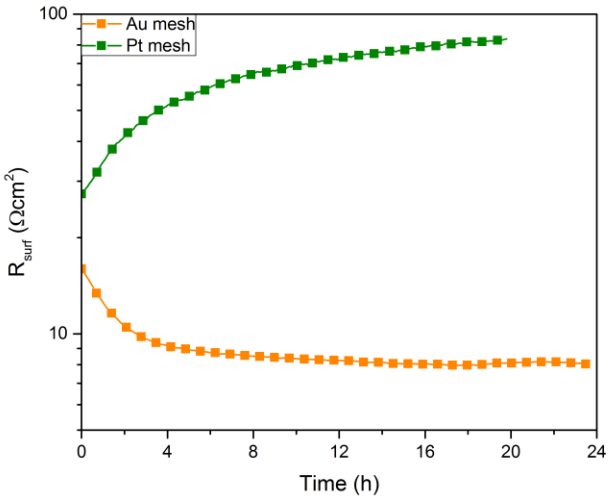

Figure 3.10. Time-resolved evolution of LSF R_{surf}, measured with Au and Pt meshes of the same spacing at 650 °C in synthetic air.

This test was reproduced three times with the Au mesh on the samples LSF_01-03 (1x1, 2x2 and 4x4 mm^2) and two times with the Pt mesh on the samples LSF_04-05 (3x3 and 4x4 mm^2), yielding comparable results (see Figure 3.23 for the other tests performed with Au mesh and Figure 3.11 for the ones performed with Pt mesh).

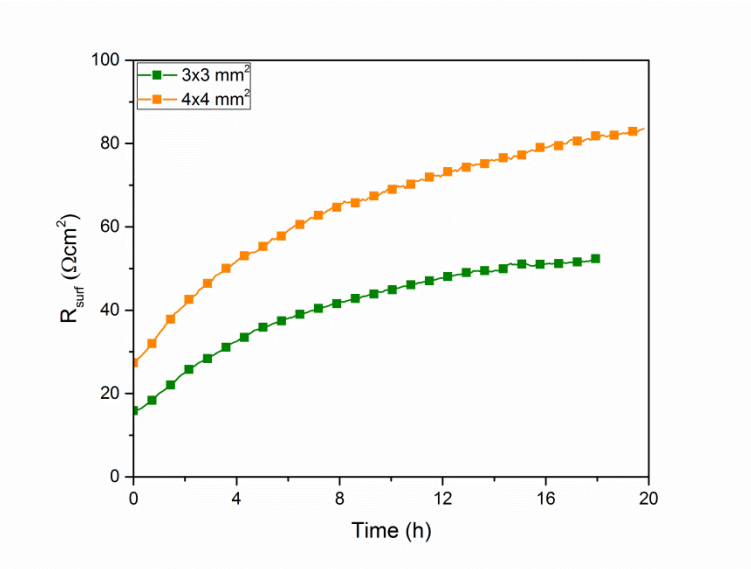

Figure 3.11. Evolution of the R_{surf} of LSF electrodes of varying size, measured at 650 °C in synthetic air using Pt mesh as CC.

The LSF_03 and LSF_05 samples were analyzed after the test using ToF-SIMS and SEM. ToF-SIMS imaging showed a slight difference between them. In particular, S or Cr enriched areas were visible on the sample tested with Au mesh, whereas more extended areas with enhanced F and Cl signal were found on the sample tested with Pt mesh (Figure 3.12). SEM imaging evidenced uniform surfaces with no particular feature that could be associated with degradation or activation, as seen in Figure 3.13.

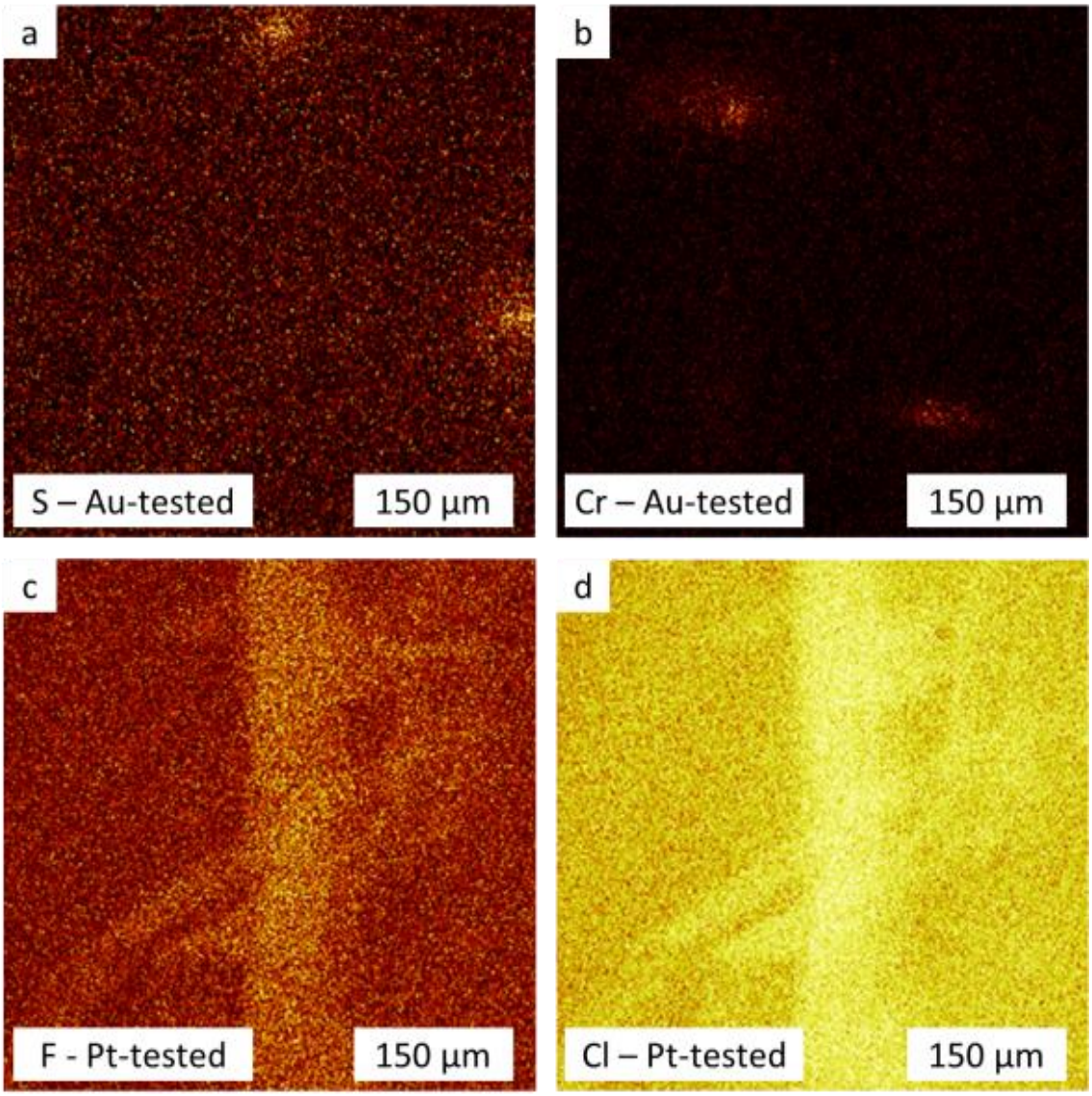

Figure 3.12. 500x500 µm^2 ToF-SIMS ion images. a) Sulfur and b) Chromium impurities evidenced on the LSF_03 sample tested with Au mesh, and c) Fluorine and d) Chlorine impurities evidenced on the LSF_05 sample tested with Pt mesh.

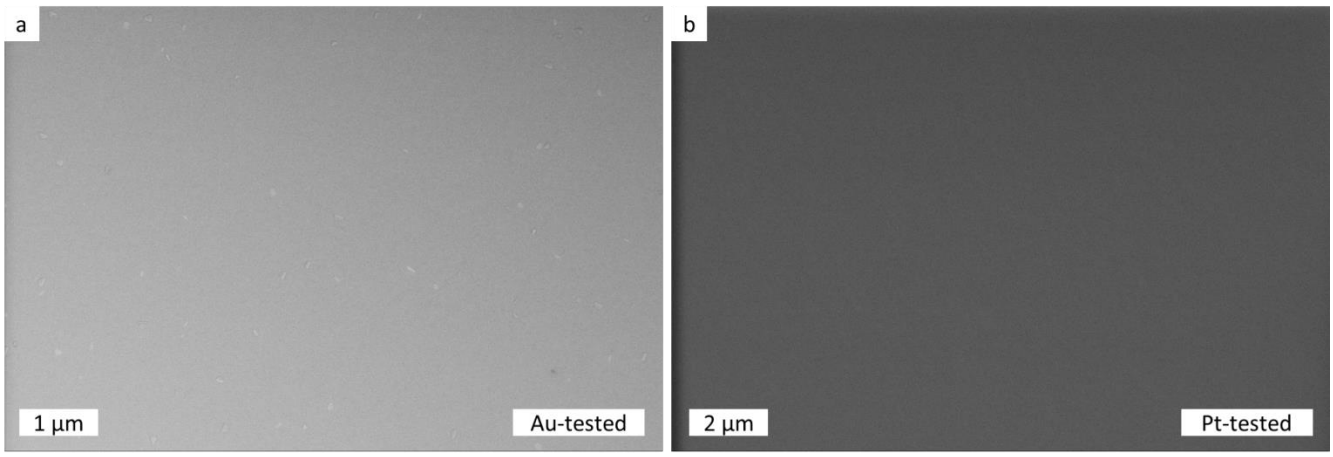

Figure 3.13. In-lens SEM images of a) the LSF_03 and b) the LSF_05 samples after testing and ToF-SIMS analysis.

3.4.2.2.3 Pastes containing metal particles

Using pastes of metal particles is an attractive current collection approach, due to the ease of application and the excellent current collection achieved. Nevertheless, such pastes typically contain organic and inorganic substances of unspecified chemistry, being a potential source of impurities. The samples LSCF_05-07, fabricated simultaneously, were tested concurrently in rig-1 using Au mesh, Au paste (DuPont) or Pt paste (Ferro), to assess this effect. The measured R_{surf} of the samples with Au or Pt paste was one order of magnitude larger than the one measured only with the Au mesh (Figure 3.14). The activation energy was also affected, being 1.98±0.16 eV for the Au mesh case, 0.77±0.01 eV for the Au paste and 1.14±0.12 eV for the Pt paste, clearly suggesting a drastic influence of the pastes on the surface exchange.

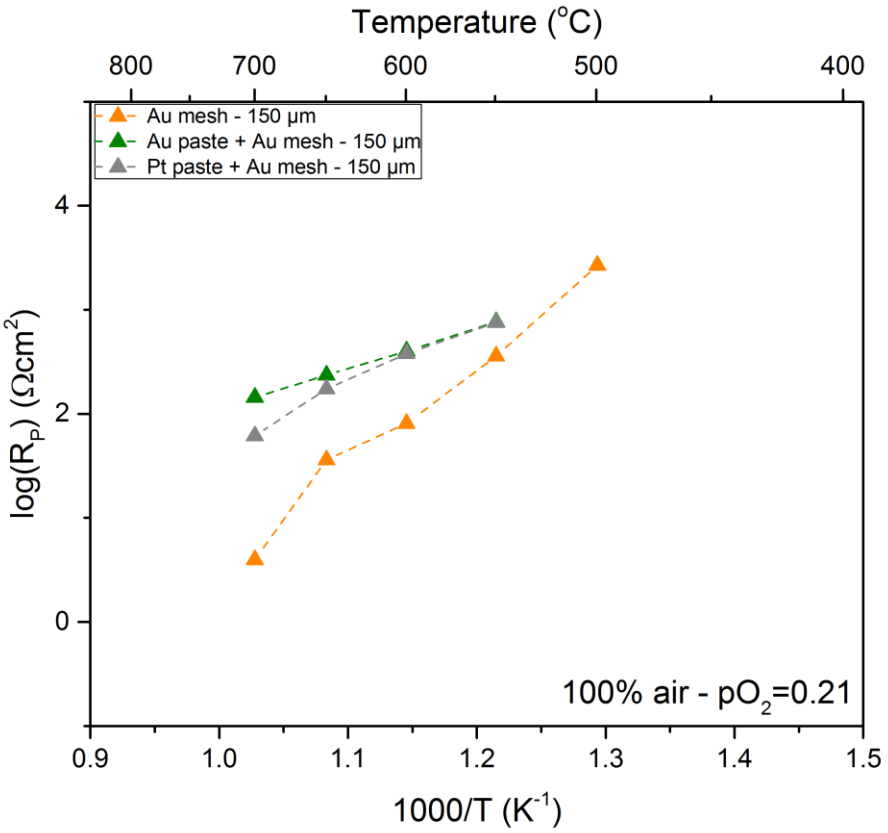

Figure 3.14. Arrhenius plots for samples LSCF_06-07, contacted with Au and Pt pastes compared with LSCF_05, contacted only with the Au mesh, measured in compressed air.

One reason for the increased R_{surf} relates to the reduced active area of the LSCF films, as part of their surface is covered by less active Au/Pt. A precise determination of the actual active area of the thin film was not realized, but SEM cross sections of the tested samples, shown in Figure 3.15 suggest that the active surface was reduced by less than a factor of 2, corresponding to a similar expected increase in R_{surf}. This is far from the factor of 10 difference observed in this study.

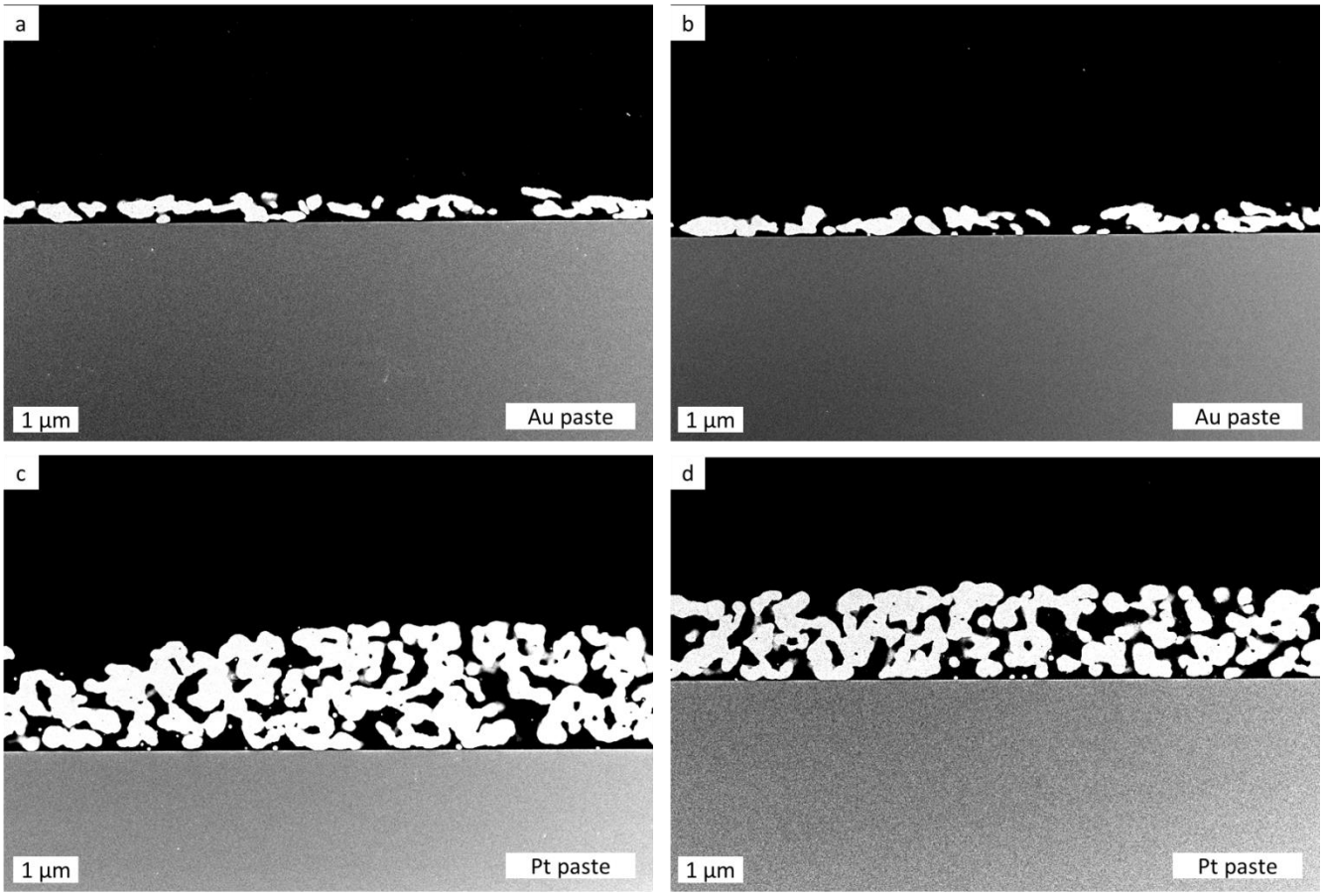

Figure 3.15. In-lens images of different positions on polished cross-sections of a) and b) the LSCF_06 sample and c) and d) the LSCF_07 sample.

ToF-SIMS depth profiling was performed on the LSCF_05-07 samples, in order to determine the difference in contaminants introduced by the pastes in comparison with the ones introduced only by the Au mesh and the atmosphere. For this purpose, areas where the pastes had peeled off after removing the Au mesh were selected. Depth profiles of the most relevant impurities detected are plotted in Figure 3.16. It can be seen that sulfur has a comparable distribution on all samples, most likely deriving from the gas phase and from the LSCF film itself, while phosphorous and fluorine showed a stronger enhancement on the surface of the samples contacted with pastes. Additionally, the sample tested with Au paste exhibited an enhancement of the silicon signal at the surface in comparison to the other samples.

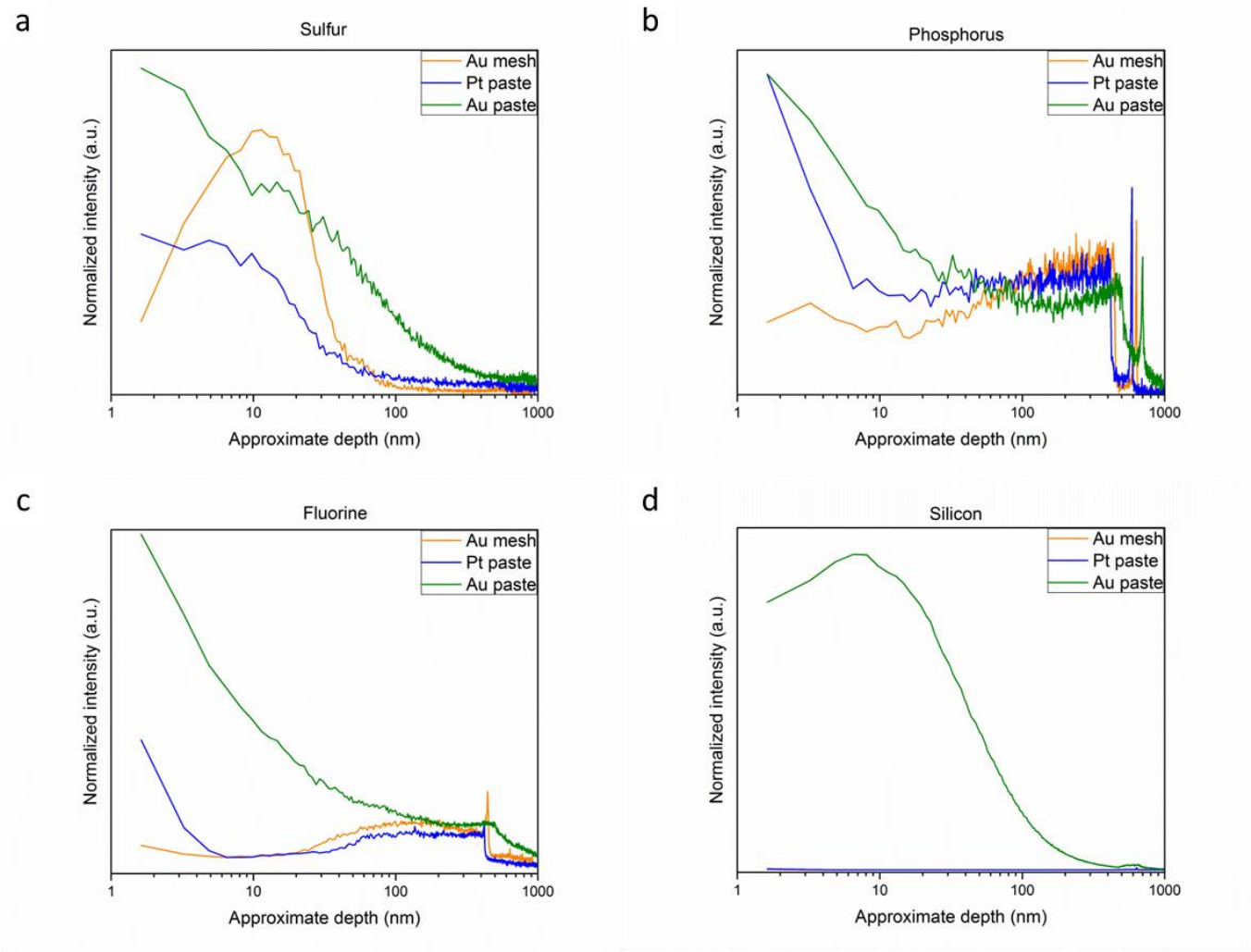

Figure 3.16. ToF-SIMS depth profiling of a) S, b) P, c) F and d) Si in the LSCF_05-07 samples.

3.4.2.2.4 Buried Pt CC

The concept of using a buried CC produced by lift-off photolithography and Pt sputtering represents an interesting alternative for various reasons: first, the spacing between the current collection lines can be tuned according to the characteristics of the film to be deposited on top; second, the metallic CCs are not exposed to the gaseous environment and thereby don't constitute a triple phase boundary for the oxygen reactions; third, being buried, the Pt will not affect the surface of the electrocatalyst as would be the case if it was applied as a mesh.

On the other hand, the different crystal structure of the sputtered Pt with respect to the underlying YSZ/GDC could affect the growth morphology of the thin film in unknown ways. LSCF samples produced with and without the underlying Pt CCs were therefore analyzed in order to assess whether this affects the measured activity of the film, either due to increased surface area and/or due to the exposure of different LSCF orientations than the (100). Microstructural investigations by SEM and AFM on the LSCF_09b sample showed a grainy microstructure (Figure 3.17a), but it could not be concluded if the film was columnar or simply

nanocrystalline on the top, given the high edge effect in the in-lens image of the cross-section (Figure 3.17b). The microstructure on top of the Pt stripes (Figure 3.17c) was finer than the one outside of the Pt pattern (Figure 3.17d). The AFM scans were also used to determine the surface root mean square roughness (Sq) of the sample, resulting in values of around 3 nm on the film between the Pt stripes and around 1 nm on the Pt stripes. As a comparison, a film deposited in the same conditions without the patterning procedure exhibited a roughness of around 0.4 nm, as mentioned in 3.4.1.3. XRD of LSCF films grown on a Pt patterned CC showed the presence of additional orientations of the LSCF, corresponding to the (111) and (220) lattice planes, besides the expected (100) (Figure 3.18).

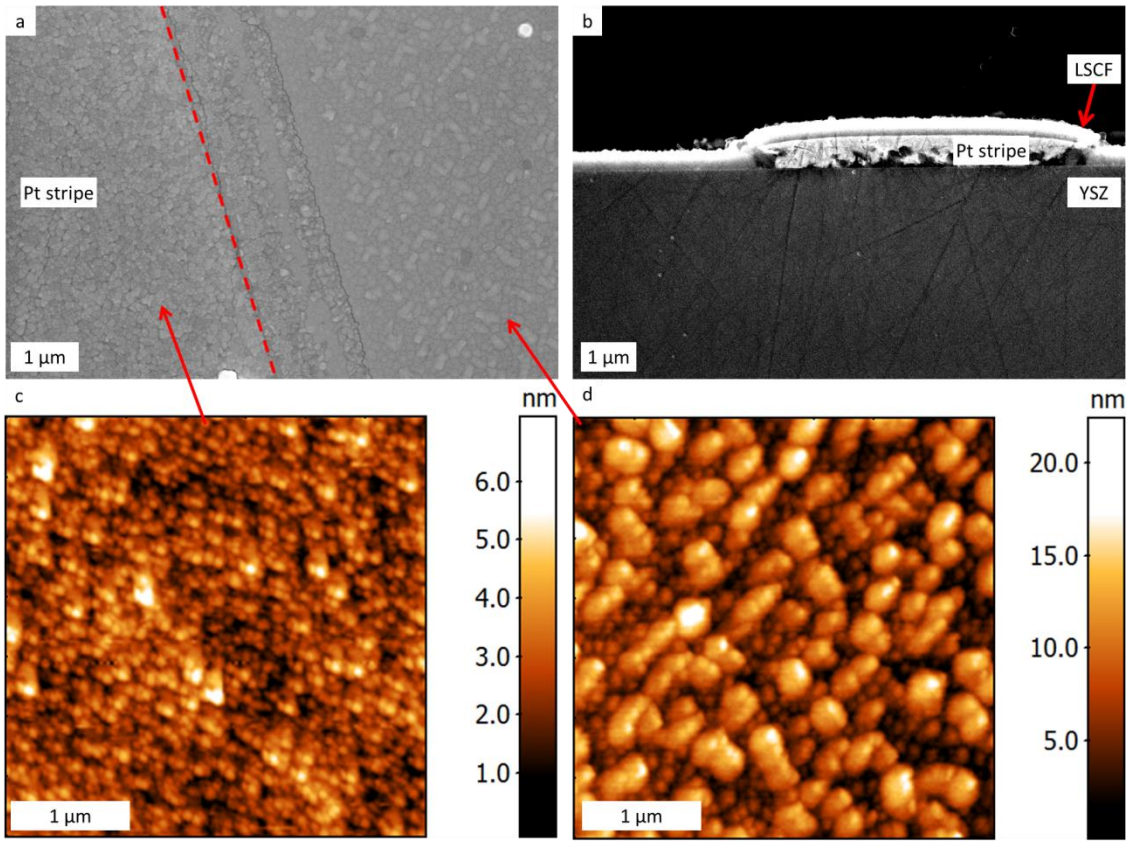

Figure 3.17. SEM (In lens) of a) the surface and b) the cross-section of sample LSCF_09b, c) and d) AFM images of the film on and off the Pt CC, respectively.

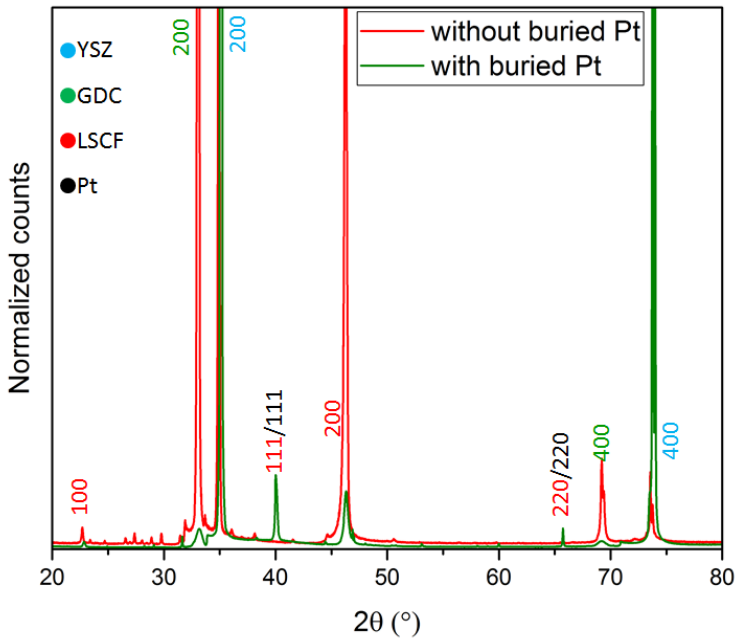

Figure 3.18. Diffractogram of the LSCF_09 sample compared with the one of the LSCF_01 sample (Figure 3.4).

Despite the influence of the underlying Pt CC on both the film microstructure and orientation, its presence only had a minor influence on the measured oxygen exchange activity, as can be seen from Figure 3.19. A sample with buried Pt CC and one without were tested in the same conditions, using an overlying Au mesh for current collection in both cases for better comparison. The sample with the underlying Pt pattern exhibits a similar oxygen exchange activity to the one without. The estimated activation energy was 1.33±0.05 eV in the case with the buried Pt CC and 1.76±0.03 eV in the case without. The R_{surf} ratio between the two samples is 1.1-1.6, increasing with temperature, a very small difference that lies within the statistical variability between different samples.

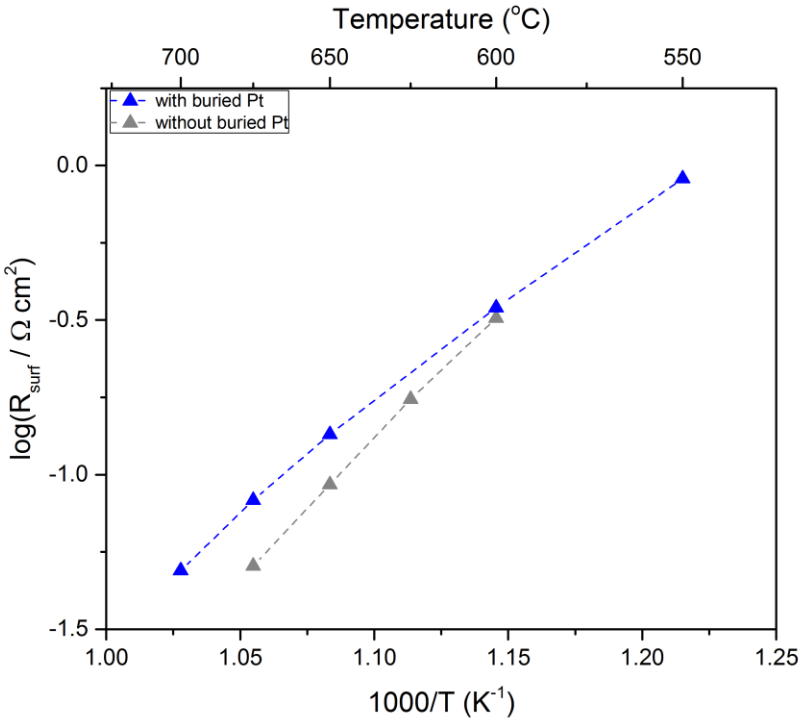

Figure 3.19. Arrhenius plots of samples LSCF_10 and LSCF_11 in synthetic air.

3.4.2.3 Influence of gas quality

The samples LSCF_02-04 were measured using Au mesh as CC in compressed air and mixtures of compressed air and nitrogen. Compressed air was chosen to represent conditions similar to the actual operating conditions of SOCs without an air cleaning filter. When evaluating the Arrhenius plots obtained from these samples (Figure 3.20), it can be seen how the R_{surf} in compressed air is drastically worsened after increasing the temperature to 650-700 °C. All samples show a degradation of 1.5-2 orders of magnitude when returning to 600 °C after having been at 700 °C. The R_{surf} is also seen to deviate from the initial linear slope already around 550 °C for the samples produced with the LSCF-A target, indicating that degradation of the surface exchange activity initiates already at this point. The activation energy was calculated for the three cases in the linear range (400 - 600 °C), measured upon heating, resulting in 1.48±0.18 eV for the 450 nm LSCF-A case, 1.65±0.24 eV for the 600 nm LSCF-A case and 1.23±0.04 eV for the 600 nm LSCF-B case.

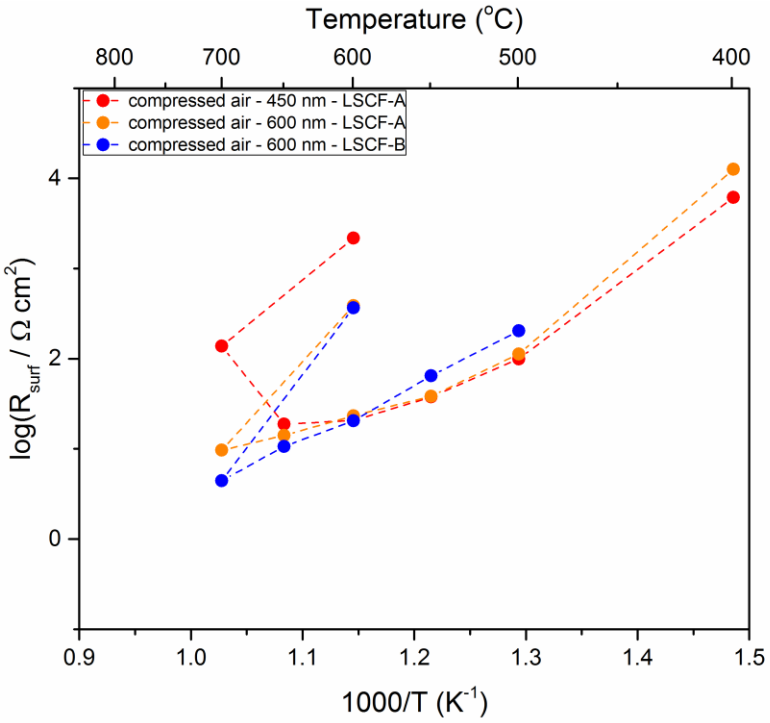

Figure 3.20. Arrhenius plots of samples LSCF_02-04 tested in compressed air. The dashed lines serve as a guide through the measurement points.

The sample LSCF_08 was measured with EIS in synthetic air and in mixtures with higher Ar content between 600 °C and 450 °C for 24 hours. Subsequently, it was kept in synthetic air for 24 hours at 600 °C and thereafter for 24 h at 650 °C. As shown in Figure 3.21a, the sample activated markedly over the first 24 hours and no degradation could be observed at 600 °C. At 650 °C the degradation rate was 0.03 $\Omega cm^2/h$, corresponding to 2.3 %/h when normalized against the starting value. When switching to compressed air, the relative degradation rate increased by a factor of 10, in line with the much larger values and degradation rate of R_{surf} measured when feeding compressed air directly in the previous sub-study. A comparison between the Arrhenius plots in clean synthetic air before degradation and in compressed air after degradation can be seen in Figure 3.21b. Despite the degradation, the activation energies were quite similar, being 1.49±0.07 eV before degradation and 1.48±0.07 eV after degradation.

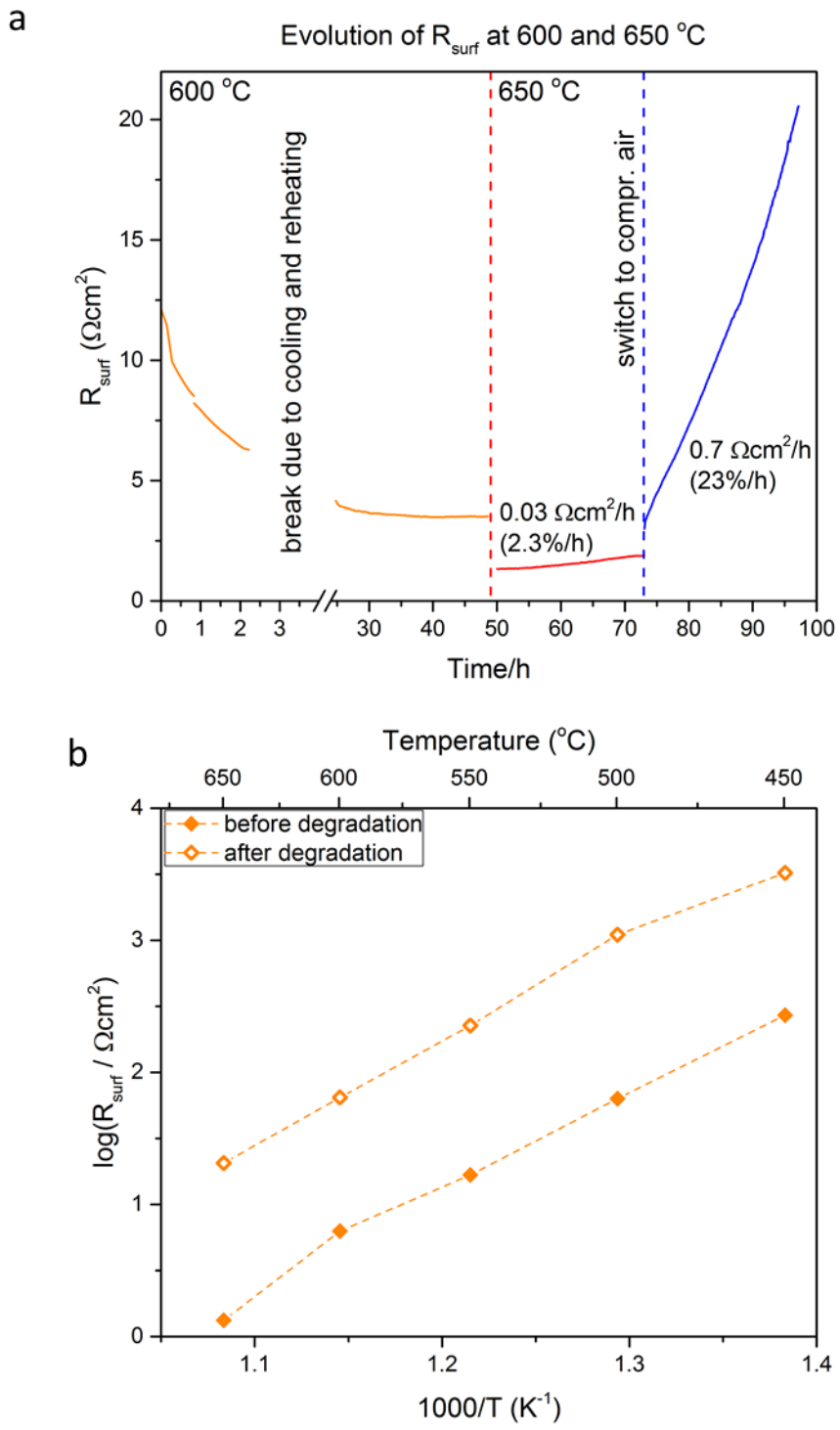

Figure 3.21. a) Time evolution of the R_{surf} of the LSCF_08 sample measured at 600 and 650 °C in synthetic and compressed air using a 300 µm Au mesh CC. b) Arrhenius plots measured after the first 3 hours of testing in synthetic air (before degradation) and after degradation in compressed air.

LSF_06 and LSF_07, which were measured in rig-2 with Au mesh in synthetic air and in compressed air, respectively, were investigated post-mortem in order to compare the type and level of impurities present on and in the samples. ToF-SIMS depth-profiling evidenced the largest differences in the near-surface chemistry of the two samples to be associated with phosphorus and, most notably, sulfur (Figure 3.22).

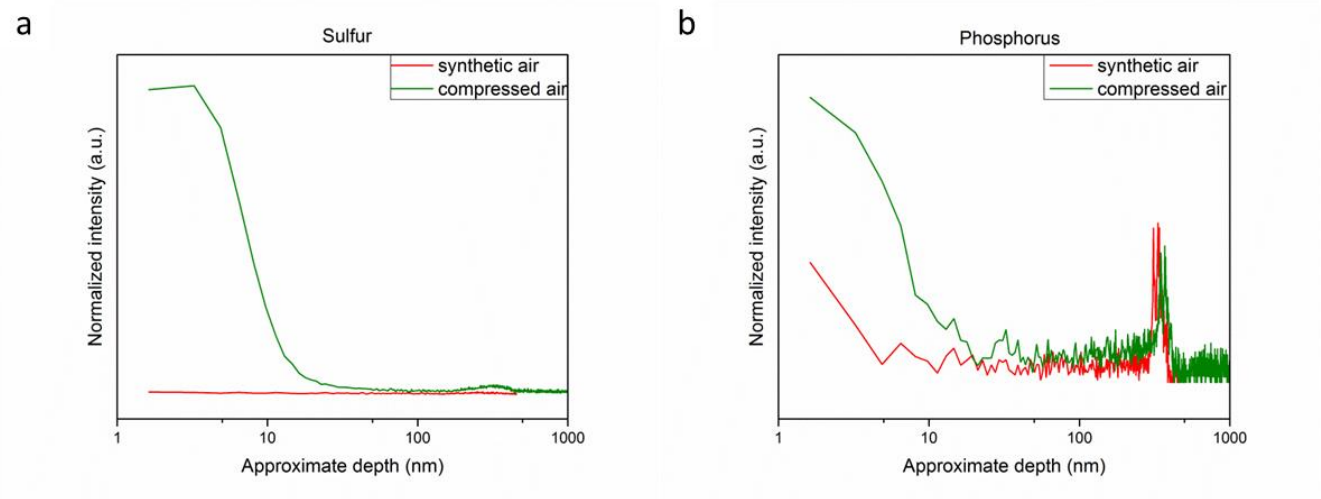

Figure 3.22. ToF-SIMS a) S and b) P depth profiles obtained on LSF_06 and LSF_07 after EIS with Au mesh as CC in synthetic and compressed air, respectively, at 650 °C.

3.4.2.4 Influence of the electrode size

One of the potential drawbacks in the use of thin film model electrodes for the determination of intrinsic material properties is associated with their decreased surface area compared to technological porous electrodes, making them more prone to poisoning from impurities originating from the materials used in the construction of the cell or from the gas phase. In order to assess the influence of the electrode size on the electrode performance, EIS was performed on LSF_01-03 with electrode sizes ranging from 1x1 to 4x4 mm^2. The samples were all tested in synthetic air at 650 °C for 20-24 hours, using Au mesh. As can be seen in Figure 3.23, the performance of all examined electrodes was comparable, thus excluding a size influence on the degradation in the investigated size range.

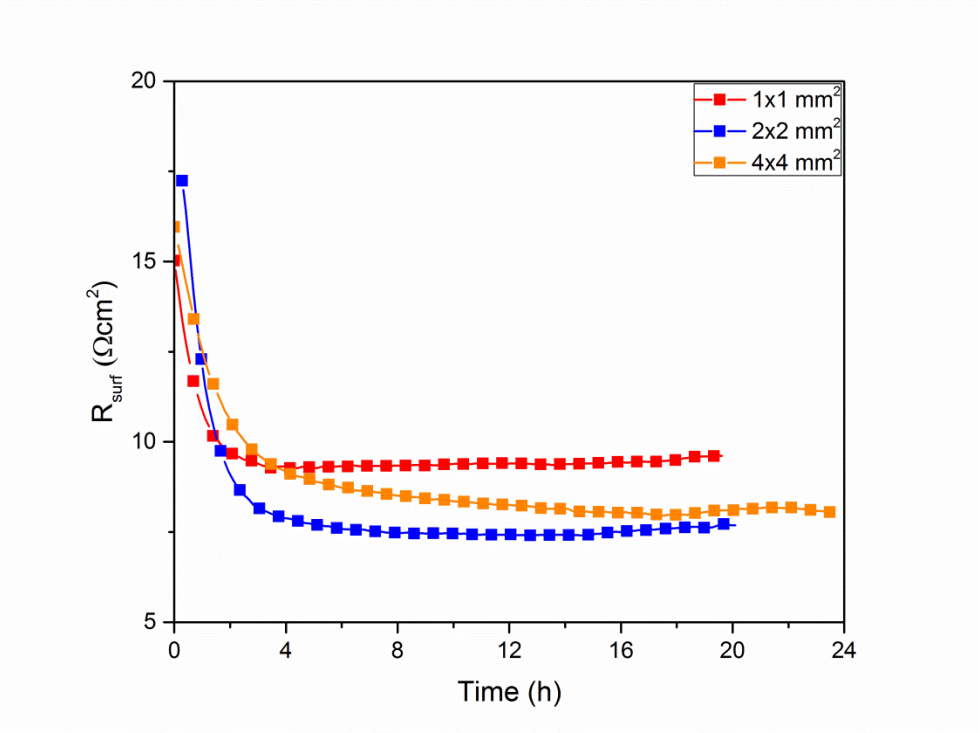

Figure 3.23. Evolution of the R_{surf} of LSF electrodes of varying size, measured at 650 °C in synthetic air using Au mesh as CC.

3.4.2.5 Influence of stoichiometry and impurities from the target

The samples LSCF_09 and LSCF_10 were tested in synthetic air at different temperatures to assess the influence of the different stoichiometries on the performance of the electrodes. Their performance was within the same order of magnitude, as shown in Figure 3.24, suggesting limited, but still present influence of the stoichiometry.

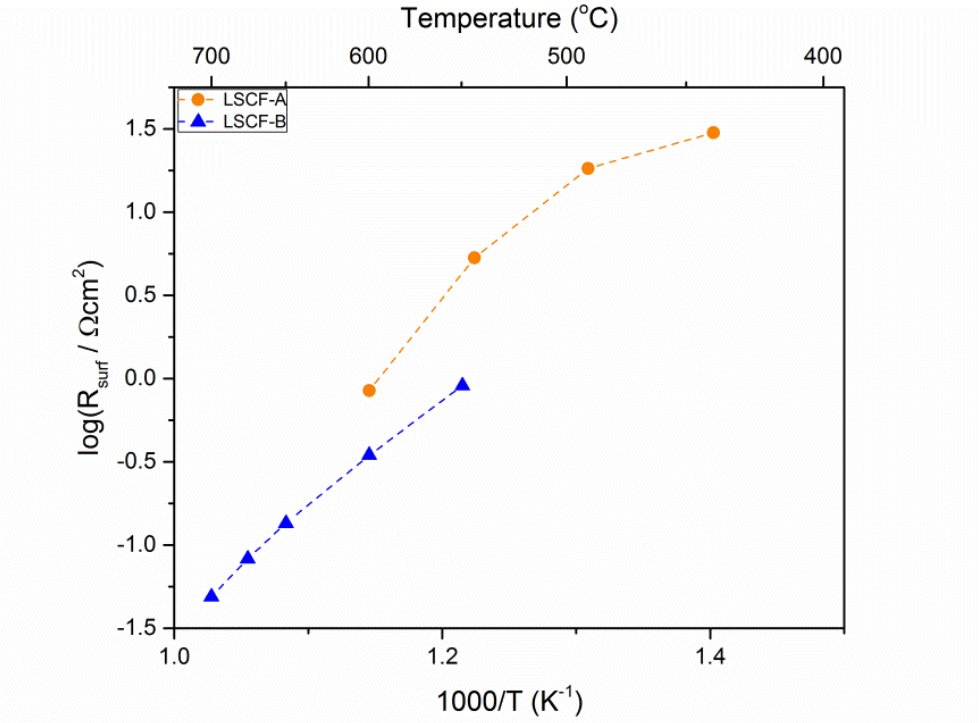

Figure 3.24. Arrhenius plots of the LSCF_09 and LSCF_10 samples tested in synthetic air.

The estimated activation energies were 1.61±0.22 eV in the LSCF-A case and 1.33±0.05 eV in the LSCF-B case. In Figure 3.20 a similar comparison can be found in the case of compressed air. Also in that case, the samples behaved only slightly differently, with similar trends in the activation energies, and degraded to the same extent. In this latter case though, any difference in the intrinsic activity of the two compositions is overshadowed by the large impact from gas phase impurities.

3.5 Discussion

3.5.1 Influence of current constriction

In the scope of understanding the activity of thin films towards the oxygen incorporation/excorporation reactions, it is necessary to obtain a reliable measurement of the R_{surf}, not influenced by current constriction contributions. Two approaches found in the literature are employed here to compare with our results.

Boukamp et al. deposited LSCF films of varying thickness, aiming to study the effect of current constriction on the R_{surf} [65]. The R_{surf} data obtained at 750 °C in air were successfully fitted with the following empirical equation:

$$R_{surf} = (R_{surf,real} + R_{electr} \cdot l^{-2}) \cdot A \tag{3.3}$$

Where l was the film thickness, $R_{surf,real}$ the surface exchange resistance in the absence of current constriction, R_{electr} a factor relating to the contribution of current constriction to the measured R_{surf} and A the area of the sample. Best fitting was achieved with a $R_{surf,real}$ of 2.0 Ω and R_{electr} of $2.9 \cdot 10^5$ Ωnm^2. The so-obtained R_{surf} resulted in 1.6 Ωcm^2 in the absence of current constriction (A = 0.8 cm^2).

Tanner et al. derived an equation to calculate the apparent ASR of a complete SOC using the spacing of the contact points and the electrical conductivities of the materials, together with the expected ASR values for each component [66]:

$$ASR = \frac{R^2}{4} \cdot \left(\frac{\rho_e \cdot t_e + R_{ct}^c + R_{ct}^a}{r_0^2 + \left(\frac{2r_0}{a}\right) \cdot \left[\frac{\left\{K_1(ar_0) \cdot I_1\left(\frac{aR}{2}\right) - I_1(ar_0) \cdot K_1\left(\frac{aR}{2}\right)\right\}}{\left\{K_0(ar_0) \cdot I_1\left(\frac{aR}{2}\right) - I_0(ar_0) \cdot K_1\left(\frac{aR}{2}\right)\right\}} \right]} + \frac{\rho_i \cdot t_i}{r_0^2} \right) \tag{3.4}$$

$$with\ a = \sqrt{\frac{\frac{\rho_c}{t_c} + \frac{\rho_a}{t_a}}{\rho_e \cdot t_e + R_{ct}^c + R_{ct}^a}} \tag{3.5}$$

where R was the distance between contact points, $\rho_{e,c,a,i}$ the resistivities of the electrolyte, the cathode, the anode and the interconnect, $t_{e,c,a,i}$ the thickness of each component, $R_{ct}^{c,a}$ the polarization resistance of the cathode and the anode, r_0 the contact point radius and $I_{0,1}$,$K_{0,1}$ the modified Bessel functions of first and second kind, zeroth and first order.

This equation was simplified for the case of SCs ($R_{ct}^a = R_{ct}^c$, $\rho_a = \rho_c$ and $t_a = t_c$). The interconnect influence was not included, since the resistivity of the used CCs was negligible. In this case, the ASR could be separated into independent R_{surf} and R_S terms, since they simply appear at the numerator of the ASR equation. This might represent a simplification, because it considers the same enhancement factor for all components, as

can be seen in equation 3.4, where the contributions of both electrodes and the electrolyte are divided by the same denominator. A reference R_{surf} value of 1 Ωcm^2 was used for the calculations. The electrical conductivity of bulk LSCF is well-known and studied for many different compositions [19,20]. For thin films, on the other hand, conductivity values between 0.5 and 10 times more than the bulk are found [54,57] For this reason, the calculation was performed with values corresponding to the bulk LSCF conductivity at 600 °C (330 S/cm) and a worst-case-scenario of one order of magnitude lower conductivity. The enhancement factor of the R_{surf} obtained with this calculation is plotted in Figure 3.25a, together with the equation derived from [65], also normalized to a reference R_{surf} value of 1 Ωcm^2. The R_{surf} values obtained from our experiments with the samples LSCF_01, LSCF_02 and LSCF_03 are also included for comparison with the simulated values. Similarly, the apparent R_S and the values obtained from all the experiments performed in the first case study (Figure 3.9b) are reported in Figure 3.25b.

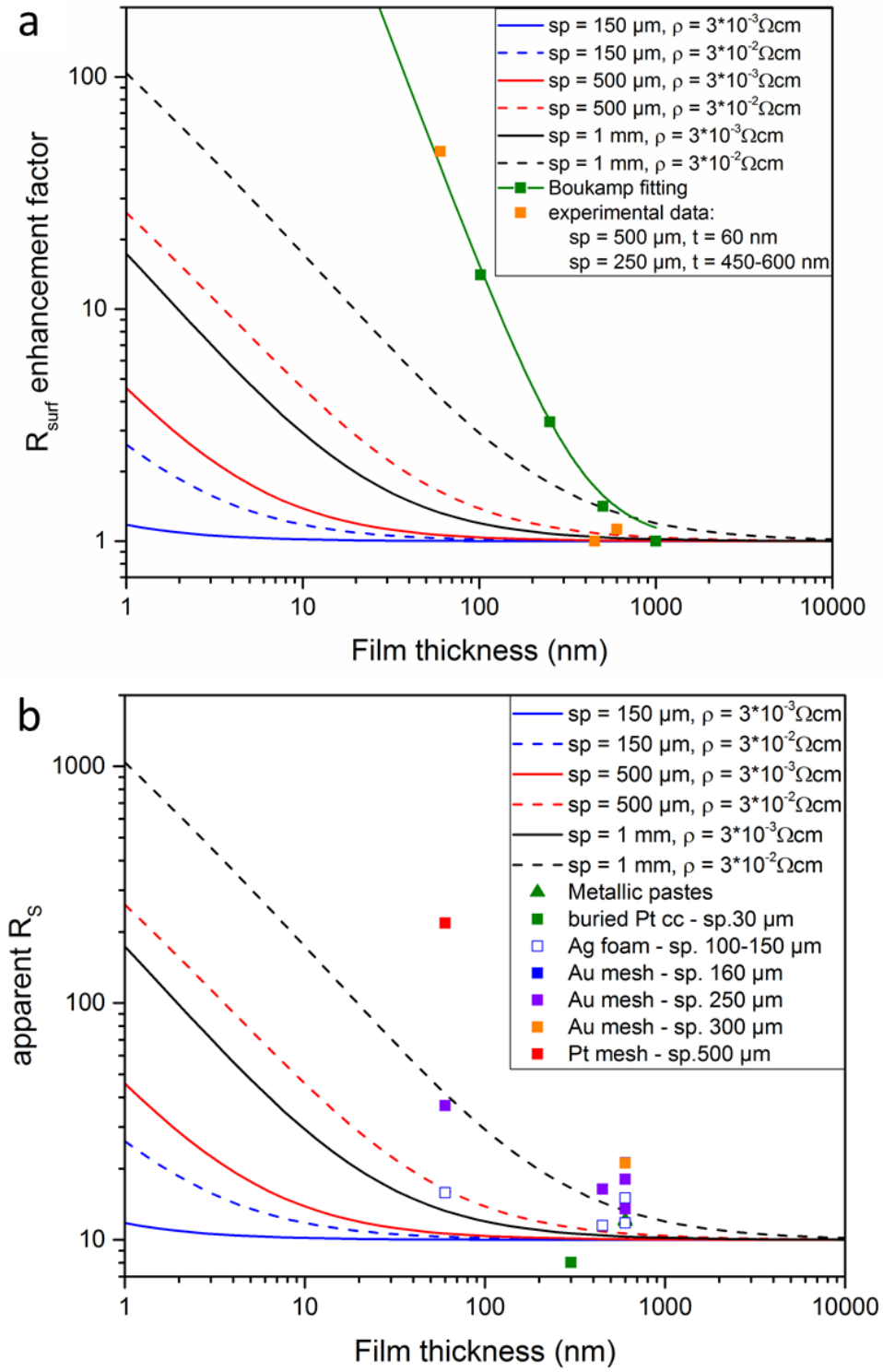

Figure 3.25. a) R_{surf} enhancement factor calculated from [65,66] **and compared with the experimental data and b) apparent R_S calculated from** [66] **and compared with the experimental data**

The Tanner approach underestimates the increase of both the R_{surf} and the R_S due to current constriction. The empirical expression derived by Boukamp, instead, matches the experimental R_{surf} values more closely. In order to ensure adequate current collection even on thin or less conductive films, mesh spacings of 250 µm or less should be preferred..

3.5.2 Influence of CC

Ag has been shown to be active with respect to the oxygen reactions and therefore does not represent an appropriate choice as a CC. At the same time, while other factors may also have played a role in the inferior performance of the samples measured using metallic pastes as CCs, it is beyond doubt that contaminants were introduced by the pastes, which are likely the main cause of the inferior oxygen surface exchange activity measured. Furthermore, the use of metallic pastes introduces an uncertainty in the determination of the active area. Therefore, their use should also be avoided if possible.

The use of fine metallic meshes or buried CCs represents thereby the safest approach towards an accurate measurement of the R_{surf}.

Boukamp et al. previously studied the influence of Pt and Au meshes on the impedance of LSCF thin films deposited by PLD on CGO pellets [53]. The used films were 2-4 µm in thickness and were characterized both in synthetic air between 500 and 800 °C, as well as in nitrogen-oxygen mixtures with pO_2 values between 0.01 atm and 0.81 atm at 600 and 750 °C.

They observed how the samples showed a higher activity and a lower activation energy when measured using a freshly cut Pt gauze with respect to one that was used in previous experiments. They attributed this change in activity to a combination of two factors, namely contamination of the Pt mesh during previous operation and contribution of the Pt CC to the oxygen reactions. At the same time, they recognized how Pt can interact with LSCF to form for example Sr_4PtO_6 or $Sr_3Pt_2O_7$, as reported by Randall et al.[89]. In our study, the Pt mesh was annealed for 24 hours in synthetic air at 800 °C before the experiment. A YSZ single crystal substrate with a 20 nm SDC film on both sides was placed between the Pt meshes to absorb eventual contaminants. This was done in order to avoid contribution from the fresh mesh to the film activity and to stimulate eventual oxidation of the mesh. It was namely observed that Pt springs or meshes, even when exposed only to clean synthetic air, presented a discoloration after multiple uses in oxidizing atmosphere[31]. The degradation of the film performance using Pt meshes was similar for all performed experiments, fast in the beginning and reaching a more stable value after 20 hours.

Contrary to our findings, Boukamp et al. observed a lower activity using Au gauze as a CC, and attributed this to $SrSO_4$ formation on the surface, considering the Au gauze as the source of the S contamination. In our study, the Au mesh was also routinely annealed for 24 hours in synthetic air at 700 °C, also in this case with a YSZ single crystal substrate with a 20 nm SDC film on both sides between the Au meshes. Using this procedure, all the samples measured with the Au meshes showed a much higher activity with a gradual activation over the first 5-10 hours. This behavior, which affected only the R_{surf}, was also observed by Boukamp et al. [53] and attributed to the settling of the Au mesh on the sample surface.

Despite deviating from the behaviors observed in [53], the conclusions reached with our study suggest that Au meshes should be preferred over Pt meshes, since they offer more stability over time. Sulfur can indeed be introduced by the Au mesh, as found from the ToF-SIMS results, but routinely cleaning the meshes

and the rig seems to help maintaining a low degradation, as opposed to the one observed using Pt meshes where P and Cl were also introduced on the sample surface.

The use of buried Pt CC, on the other hand, seems to offer another viable alternative. The R_{surf} of films with and without buried Pt CC did not show significant deviations. Nevertheless, the buried Pt CC compromises the quality of the thin film, resulting in at least partly columnar/particular microstructures of the films exposing multiple orientations, thereby introducing some uncertainty. Since the process required to produce the patterns can be cumbersome and complicated, and in absence of any obvious improvement, the use of buried Pt CC seems less attractive that the use of fine metal meshes where this is acceptable. Buried Pt CC may still be a very valuable approach when optical access to the film surface is required and/or for poorly conducting thin films.

3.5.3 Influence of the gas purity

It could be seen that the relative degradation rate of LSCF at 650 °C in compressed air increased by a factor of 10 when compared with the one in synthetic air at the same temperature. Furthermore, the near-surface chemical characterization on samples tested separately in both atmospheres exhibited an increase of sulphur and phosphorus on the sample tested in compressed air. These impurities could only be introduced by the atmosphere, since all other conditions were the same, and suggest that even a low concentration of impurities in the gas (Sulphur is commonly found in tens of ppm concentrations in air) can react with the surface of the investigated materials and thereby affect their performance.

3.5.4 Other examined parameters

The influence of the electrode area was also investigated. Smaller electrodes have a larger perimeter-to-surface ratio than larger electrodes, and might thereby be more susceptible to impurities diffusing from the YSZ electrolyte surface. However, the results showed no observable trend, and a size-dependence in the examined range was therefore excluded.

Similarly, the influence of the stoichiometry of different samples was also investigated, without leading to significant differences. Furthermore, the LSCF-B powder was believed to be less contaminated than the LSCF-A powder, given the high purity of the precursors and the precautions used to limit the introduction of contaminants, but a quantitative comparison was not available. It appears however that the CCs' and atmosphere's influence on the R_{surf} are much more important.

3.6 Determination of the intrinsic activity of LSCF films

Considering all parameters that were explored in the undertaken studies, the measurements performed on the sample LSCF_09 are considered to be the most accurate in terms of the determination of the intrinsic activity of the thin film without the influence of external factors.

The measurements were performed with a buried Pt CC, which was seen in sections 3.4.2.1 and 3.4.2.2.4 to be an adequate choice, and a film thickness of 300 nm produced with the LSCF-A target. Furthermore, synthetic air was used to avoid the contamination of the surface from gas phase impurities.

The surface exchange data were collected in a pO_2 of 0.21 bar at temperatures between 440 and 600 °C and the pO_2 dependence was evaluated at 600 °C between 0.21 bar and $2.6 \cdot 10^{-4}$ bar. The results can be seen in the following Figure 3.26.

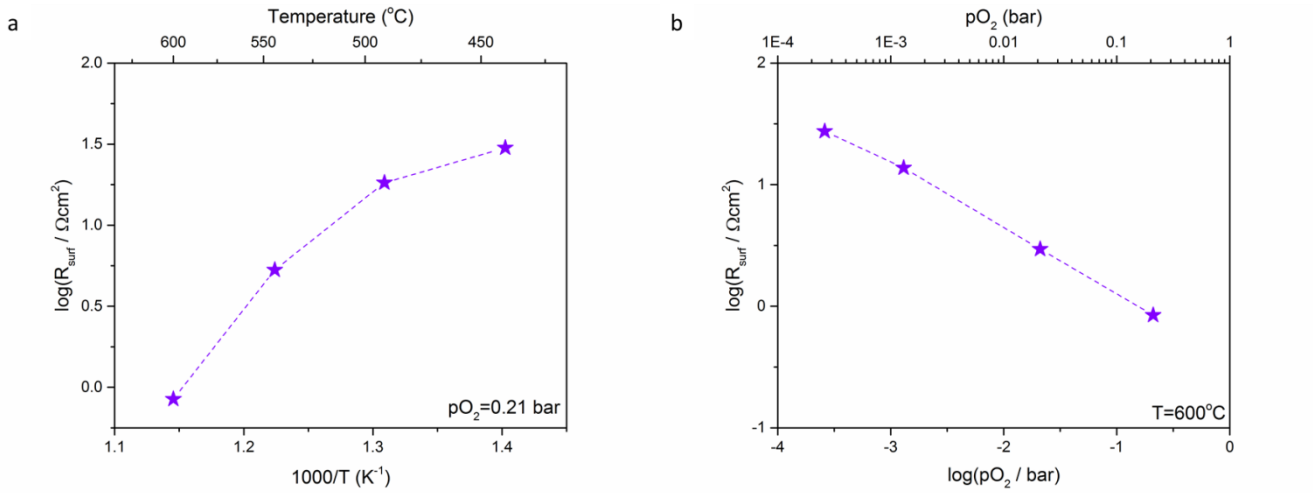

Figure 3.26. a) Arrhenius plot in 0.21 bar O_2 and b) pO_2 dependence at 600 °C for the LSCF_09 sample.

3.7 Conclusions

Given the large scatter of oxygen surface exchange data in literature, various parameters were taken into consideration to assess their influence on the determination of the R_{surf} of perovskite thin films. The evaluated parameters were related to appropriate current collection, to the influence of the CC chemistry, to the gas purity and to the composition of the samples. The chemistry of the CC, the current constriction due to insufficient film thickness or too large CC spacing, and the gas quality exhibited the strongest influence with respect to the oxygen exchange activity. Instead, parameters such as the sample stoichiometry or the electrode size proved to be of no or limited significance. Our results suggest that, in order to obtain reliable results, Au meshes with small spacings or buried metallic CCs should be preferred. Au meshes represent the easiest solution, but require film thicknesses of hundreds of nm in order to provide sufficient current collection. Buried metallic grids, instead, provide the best current collection, but are more cumbersome to fabricate, requiring lift-off photolithography, which is a very delicate process that needs to be performed in a clean room. On the other hand, pastes should be avoided, as they introduce impurities that affect the film activity. Ag is also not recommended, as it is active towards the oxygen reactions on its own, and therefore can represent the most active species in cases where the films have a low activity (R_{surf} at 600 °C in the order of hundreds of Ωcm^2).

Additionally, since gaseous impurities strongly affect the measurements, model electrode studies should be performed using high purity synthetic air. In specific, Sulphur was found in the post-mortem chemical analysis of the tested electrodes, but other contaminants present in compressed air, such as H_2O and CO_2 could likely also affect the activity of the oxygen electrodes.

Finally, the impurities present in the PLD targets should also be avoided or precisely determined if possible, which can be done with very clean and controlled synthesis processes from pure precursors.

4 Towards the mechanistic interpretation of the oxygen exchange far from equilibrium by combining EIS and XPS

4.1 Introduction

The electrochemical reactions occurring on the oxygen electrodes of SOCs are still poorly understood, despite numerous studies attempting to explain their mechanistic aspects, like the reaction kinetics and intermediate species. In the case of MIECs, where the oxygen reactions occur at the interface between the gaseous environment and the electrode material, the chemistry and structure of the electrode surface are of crucial importance. Chemical and structural inhomogeneities of the surface exposing more or less active phases or lattice planes, precipitation of insulating secondary phases or presence of impurities on the surface can and will all affect the reaction kinetics and need to be studied with highly sensitive *in situ* techniques in order to be correlated with the performance of the electrodes [28,90–92].

Another crucial parameter when studying the gas/solid electrochemical interface of MIEC electrodes is the surface potential, or rather its change with the applied overpotential. Since the electrochemical reactions occur at the electrode/gas interface, it is the change in surface potential due to the applied overpotential that acts as the driving force for the reactions. The relationship between overpotential and surface potential change is generally not known, as it can be influenced by the variation of adsorbate coverage, surface dipoles, or space charge layers. Fleig et al. set forward a model resulting in a number of possible relationships between surface potential and overpotential in different limiting cases for adsorbate coverages, maximum surface dipole moment and number of available adsorption sites, making the simplifying assumption that the electron transfer was the rate-limiting step in the oxygen reactions and the surface dipole layer could be treated as a simple plate capacitor. Experimental data are lacking, given the difficulty in accessing the surface potential with conventional analysis techniques[93–95].

In situ techniques with high surface chemical sensitivity are therefore very useful in the study of such electrochemical reactions, and in the last decades numerous efforts were made in order to perform XPS, traditionally a UHV-technique, at pressures closer to the operating conditions of electrochemical cells. The use of near-ambient pressure XPS (NAP-XPS) to study the surface reactions on SOC materials represents a great opportunity due to its high chemical sensitivity and possibility to tune different information depths by tuning the incident photon energy [43,44,96,97]. Additionally, Feng et al. established a procedure to measure the surface potential using NAP-XPS in grazing incidence, by monitoring the binding energy (BE) shifts of the gaseous species and comparing them to the ones of the lattice species [98].

The work described in the present paper employs in-operando NAP-XPS in an attempt to simultaneously probe electrochemical performance and surface chemistry of model $La_{0.58}Sr_{0.4}Co_{0.2}Fe_{0.8}O_{3-\delta}$ (LSCF) electrodes. Furthermore, the relationship between applied overpotential and variation in surface

potential is deduced for the first time for LSCF electrodes. Finally, lateral spatial inhomogeneities in the surface chemistry of model LSCF electrodes are mapped by NAP-SPEM close to relevant SOC operating conditions for the first time.

4.2 Experimental

4.2.1 Sample preparation

Similarly to other XPS studies conducted on SOC materials, the samples were designed with two main constraints in mind: first, the polarization resistance should be attributed only to the working electrode (WE) of the cell and second, the WE should be uniformly polarized[99,100].

Since the WE itself needed to be fully accessible for the surface measurements, the strategy adopted for the best current collection and uniform polarizability was that of a CC buried under the electrode film. For this reason, a 20 nm SDC layer was deposited with PLD on one side of 1 cm^2, 0.5 mm thick 9.5 mol% YSZ (9.5YSZ) single crystal substrates with (100) orientation (Crystal GmbH, Germany). Subsequently, a Pt pattern was deposited using lift-off photolithography and sputtering, before depositing the final LSCF film with PLD through an Inconel shadow mask of 2x2 mm^2 (Fotofab, ESPI Metals). The target production and PLD parameters for the LSCF (H.C. Starck) deposition can be found elsewhere (refer to other chapter/paper or to a unified materials and methods chapter?). The Pt pattern consisted of a 1.8x1.8 mm^2 grid of 5 µm-wide stripes with a spacing of 30 µm in one direction and 300 µm in the other.

In order to have a negligible contribution from the counter electrode (CE), two parameters could be tuned, namely the CE activity and its dimensions relative to the WE. To produce an efficient CE, Pt paste (Ferro) was painted on the other side of the YSZ substrates. The paste was then fired at 900 °C for 2 hours to create a porous backbone, which was well-adhering to the substrates. An in-house developed solution of praseodymium-doped ceria was used to infiltrate the backbone and was fired at 300 °C for 1 hour after each one of the two infiltration cycles. The CE produced with this procedure exhibited an ASR of around 7.5 Ωcm^2 in $1.3 \cdot 10^{-3}$ bar O_2 at 600 °C. As a comparison, the R_{surf} of LSCF at the same conditions was around 40 Ωcm^2. Additionally, the CE covered the entire YSZ substrate, resulting in an area of around 1 cm^2, while the WE measured 2x2 mm^2. Combining the two factors, the ratio between the WE and the CE polarization resistance exceeded 100, allowing the CE influence to be considered negligible (< 1 %). Even in 0.21 bar O_2, where the R_{surf} of LSCF before degradation was comparable to the ASR of the CE (0.3 Ωcm^2), the area factor itself guaranteed a factor of 25 between the resistances, bringing them into two different orders of magnitude.

4.3 Results

4.3.1 Characterization of pristine sample

4.3.1.1 SEM and AFM for microstructural characterization

Since the production of the WE followed the same path as the one used for the LSCF_09 sample in chapter 3, the considerations on the microstructure of the surface expressed in 3.4.2.2.4, referring to Figure 3.17, are considered valid also for the sample used in this study.

4.3.1.2 ToF-SIMS for chemical characterization

ToF-SIMS imaging of the surface of the as-deposited sample showed traces of Na, K and Ca on some areas of the electrode, as well as F and Cl on most of the surface. Traces of S were also found. The most relevant impurities are shown in Figure 4.1.

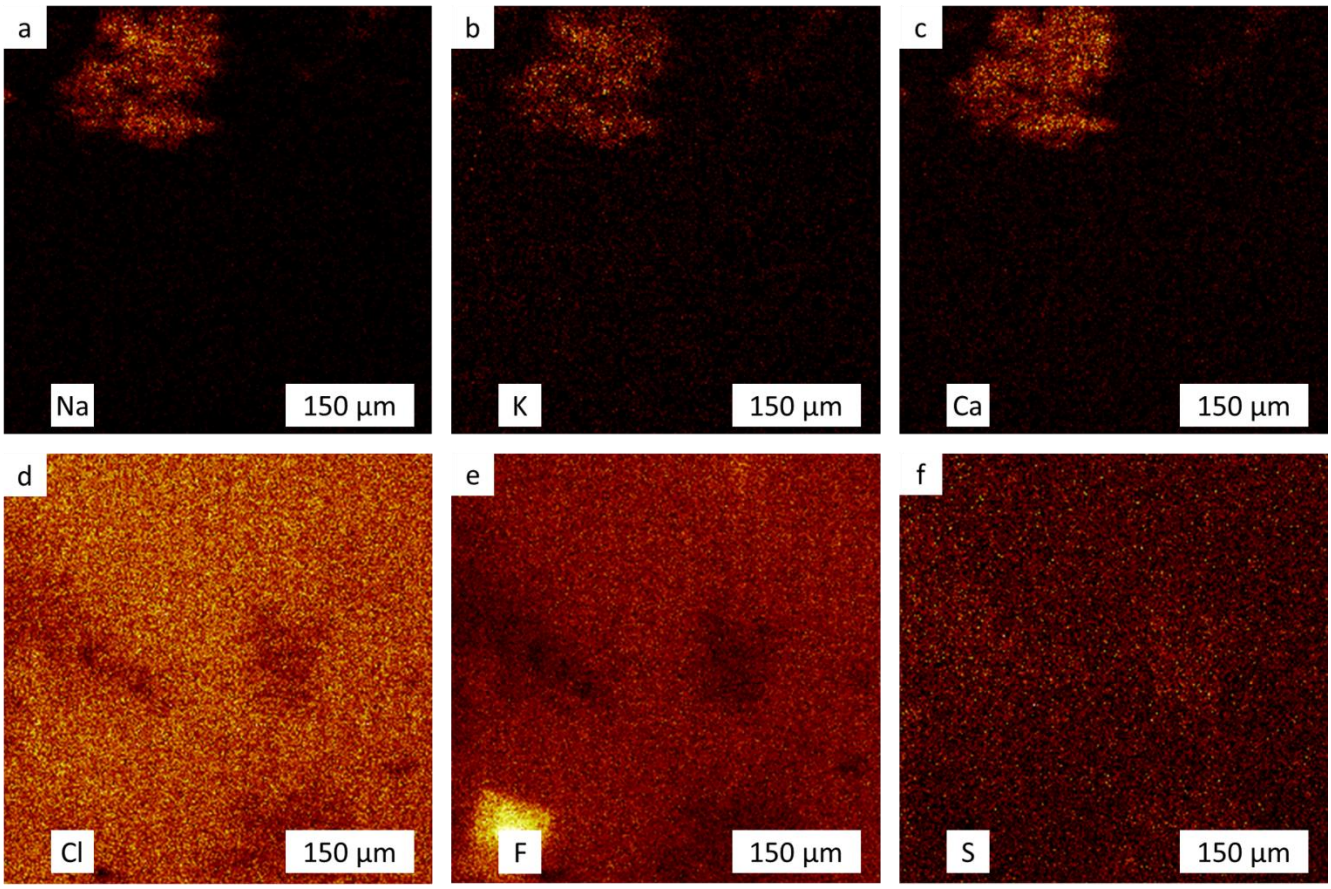

Figure 4.1. ToF-SIMS ion images of the main impurities evidenced on the LSCF film.

4.3.1.3 XRD for the determination of the crystal structure

XRD was performed on the as-deposited sample, to investigate the crystal structure of the LSCF film. Besides the lattice planes of the (100) group, which would be expected in the case of epitaxial growth on the

YSZ single crystal and SDC buffer layer, two main reflections could be seen, which are consistent with the LSCF (111) and (220) lattice planes, as seen in Figure 4.2.

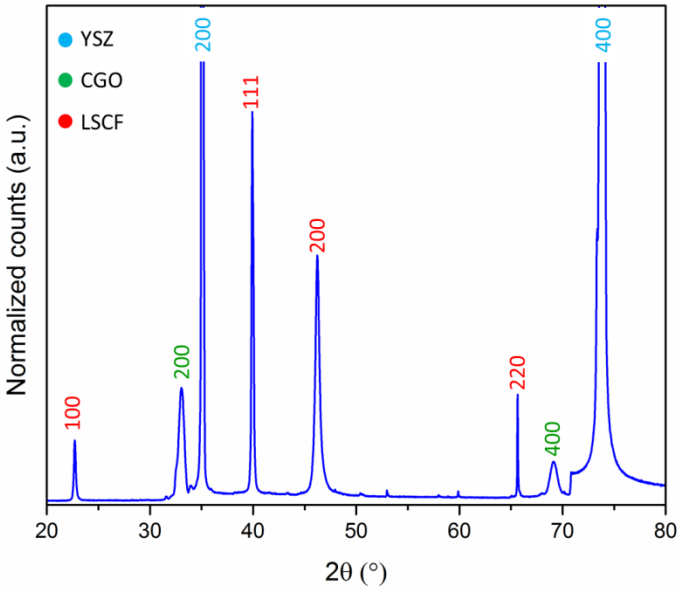

Figure 4.2. XRD pattern of the as-deposited sample.

4.3.2 Laboratory vs ALS beamline sample performance

4.3.2.1 Electrochemical measurements in the two environments.

Twin samples were tested at 600 °C, both in the laboratory setup, in order to establish the best testing conditions, as well as during the beamline experiment. In the laboratory the gas environment was varied between synthetic air (0.21% O_2 in Ar) and the minimum obtainable pO_2 of $1.3 \cdot 10^{-1}$ mbar. In the beamline experiment, instead, the pO_2 was varied between 1.3 mbar (1 Torr) and $1.3 \cdot 10^{-2}$ mbar (0.01 Torr). At each chosen value of pO_2, EIS was performed both at OCV and with up to 600 mV applied cell voltage both in anodic and cathodic direction. In both setups the contact to the WE was provided with Pt-Ir springs pressing down on Pt contact pads connected to the buried Pt CC.

The EIS spectra, of which an example is shown in Figure 4.3, showed a high-frequency (HF) series resistance attributed to the YSZ single crystal (R_S), a pO_2-independent medium-frequency (MF) arc and a pO_2-dependent low-frequency (LF) arc. The high-frequency arc was also observed in other studies, although without Ce-based buffer layer [24,54,88], and was attributed to an ion transfer resistance at the LSCF/YSZ interface. By analogy, given the pO_2 independence observed in this study, the HF arc was attributed to an interfacial ion transfer at the LSCF/CGO and/or the CGO/YSZ interface (R_I). The low-frequency arc instead was attributed to the LSCF film chemical capacitance and R_{surf}.

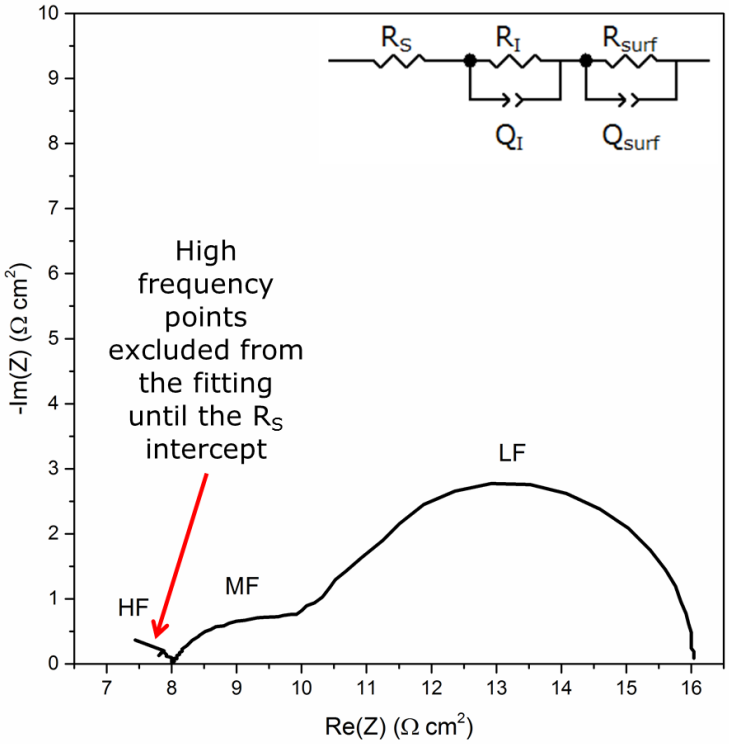

Figure 4.3. Typical EIS spectrum for the investigated samples.

In the laboratory experiment at low pO_2 (below 1.3 mbar) and anodic polarizations above +0.3 V), a third arc at even lower frequencies became evident. This arc was attributed to the CE (R_{CE}) showing a response because it could not incorporate enough oxygen to supply for the current flowing through the cell. In the beamline experiment, the third arc only appeared for the lowest pO_2 under anodic polarization.

In order to calculate the polarization actually applied to the WE, the contribution from all other elements, multiplied by the current flowing through the cell, was subtracted:

$$\eta = V - (R_S + R_I + R_{CE}) \cdot I \qquad 4.1$$

where η is the calculated overpotential of the WE, V is the cell voltage applied through the potentiostat, $R_{S,I,CE}$ are the resistances of the YSZ electrolyte, the interface layer and the CE (where present) and I is the measured current flowing through the cell.

By monitoring the current flowing through the sample during each EIS cycle and plotting them against the overpotential calculated from equation 4.1, the IV curves summarized in Figure 4.4 were obtained. Notably, the current values measured in the experimental chamber in the beamline were 5-10 times higher than the ones at the same overpotential in the laboratory experiment.

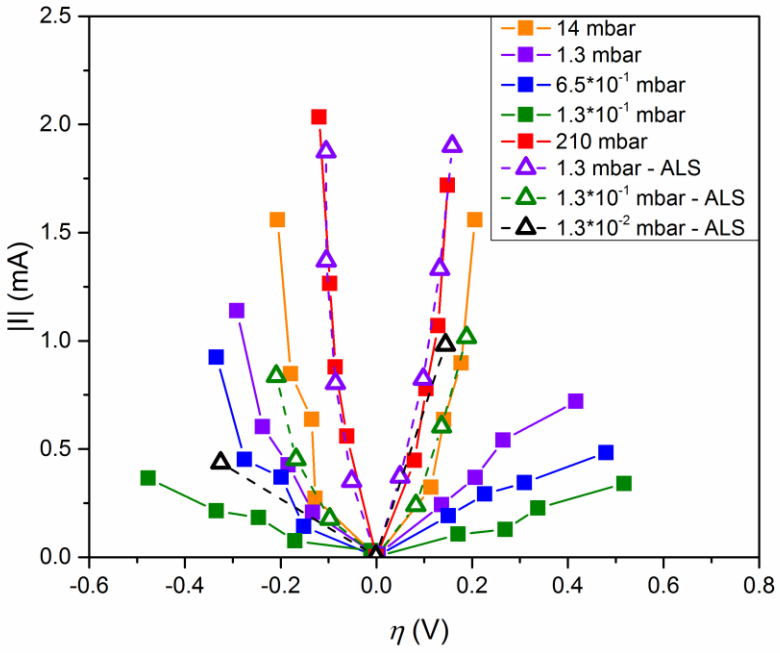

Figure 4.4. IV curves measured in the laboratory and in the beamline experiment at 600 °C.

4.3.2.2 Time and polarization dependence of the samples' performances

One of the twin samples was measured with EIS under polarization (-500 mV to +300 mV) in the laboratory setup, and R_{surf} was monitored with respect to both time and applied polarization. In the first part of the experiment, summarized in Figure 4.5a, the sample exhibited a R_{surf} of 0.2-0.3 Ωcm^2 at the beginning in synthetic air (210 mbar), both at OCV and with negative polarization. When switching to positive polarization, however, the R_{surf} exhibited an increase of 3-4 times and returned close to the starting value (0.5-0.6 Ωcm^2) when removing the polarization. In all other atmospheres, however, the R_{surf} decreased when polarizing the sample in both directions and recovered to approximately the starting values when returning to OCV. When returning to synthetic air (210 mbar – ret), the initial R_{surf} had increased to 2.6-2.7 Ωcm^2, and showed a behavior similar to the R_{surf} obtained at lower pO_2 values upon negative polarization. Upon positive polarization, instead, the R_{surf} increased initially but then decreased like in the cases at lower pO_2. The R_{surf} at the end of the second polarization cycle in synthetic air was 4.2-4.3 Ωcm^2, 15-20 times higher than the first measured value of 0.2-0.3 Ωcm^2. The sample was then left for 48 more hours in synthetic air at OCV, during which R_{surf} increased from 5.5 to 13.2 Ωcm^2 (Figure 4.5b).

A second experiment was performed on the same sample to investigate reproducibility and explore the effect of even lower pO_2 values (Figure 4.5c). The R_{surf} generally decreased upon polarization in all atmospheres, as was observed in the previous set of experiments at lower pO_2, and showed comparable values at 1.3 mbar and 6.5·10^{-1} mbar. After having polarized the sample in the lowest pO_2, the R_{surf} in synthetic air recovered to a slightly lower value (0.75 times) than the one observed at the end of the previous experiment.

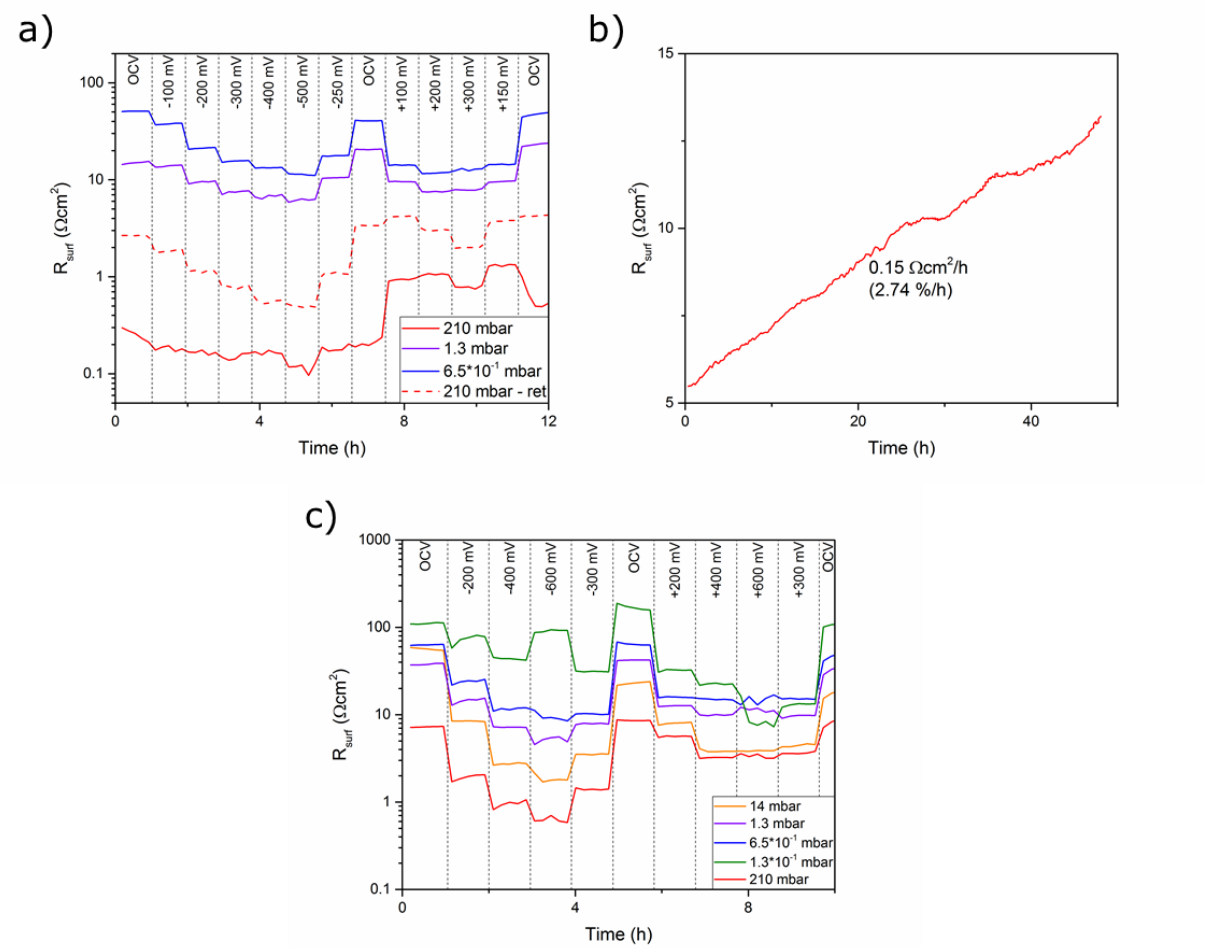

Figure 4.5. a) and c) The evolution of the R_{surf} over time at 600 °C in different atmospheres and at different polarizations for the same sample, and b) evolution of the R_{surf} at 600 °C in synthetic air at OCV.

In the beamline experiment on the second of the twin samples the polarization sequence was adapted to the more limited available time (two shifts of approximately 12 hours, with an interruption of 12 hours in between) and to the necessity of acquiring photoelectron spectra while polarizing the sample. EIS was recorded at OCV only when switching from negative to positive polarization, apart from the first polarization sequence at the highest pO_2 (1.3 mbar), where EIS at OCV was repeated after the positive polarization steps. Figure 4.6a shows that the R_{surf} at OCV recovered its original value after the first polarization sequence. EIS at OCV was also recorded for around 12 hours at the intermediate pO_2 ($1.3 \cdot 10^{-1}$ mbar) between the two available shifts in order to evaluate the degradation at OCV in the beamline setup (Figure 4.6b). The R_{surf} at OCV approximately doubled in this period, from 25-30 Ωcm^2 to 50-55 Ωcm^2. The evaluated degradation rate of 1.6 Ωcm^2/h, corresponding to approximately 5%/hour when compared to the starting value, is in line with the value measured in synthetic air in the laboratory experiment. When applying positive polarization to the sample, the R_{surf} value decreased again, as observed in the other cases.

Notably, when switching to the lowest *pO2* ($1.3 \cdot 10^{-2}$ mbar), the R_{surf} at OCV, recorded after the negative polarization steps, decreased significantly (Figure 4.6c), resulting in a value comparable to the one measured at higher pO_2 (respectively 25-26 Ωcm^2 and 25-55 Ωcm^2).

When comparing the results in Figure 4.5 and Figure 4.6 it can be observed that the R_{surf} values in the beamline experiments were 2-4 times lower than in the equivalent conditions in the laboratory experiment.

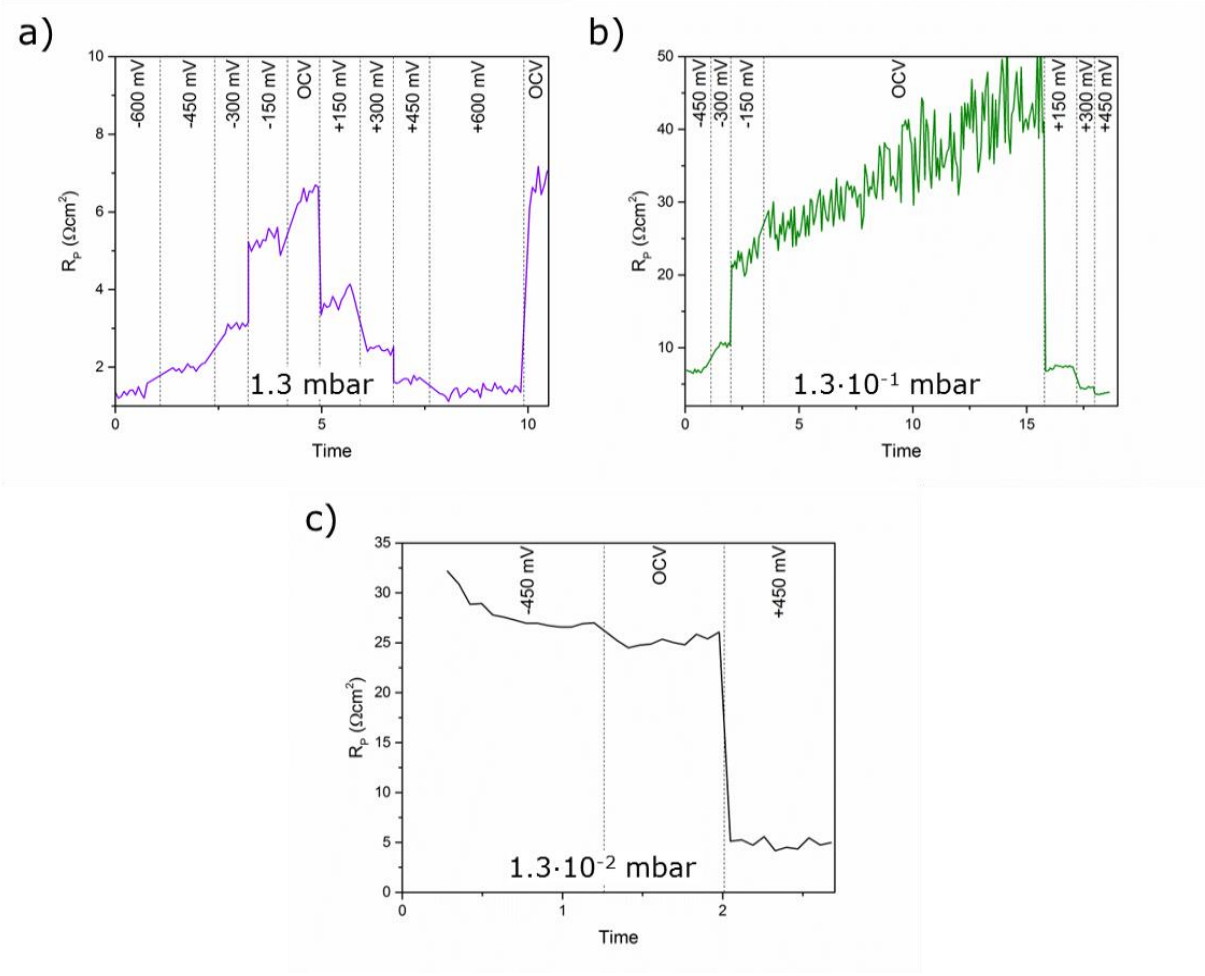

Figure 4.6. The evolution of the R_{surf} over time at 600 °C in different atmospheres and at different polarizations.

In conclusion, the samples proved to maintain their performance through changes in polarization in both atmospheres. Prolonged measurements at OCV showed that the samples progressively degraded in all the examined conditions of temperature and pO_2. When polarizing cathodically at low pO_2, in both environments a better performance was observed. This could be correlated with the formation of a secondary active phase, since the effective *pO2* obtained at the electrode reached values lower than 10^{-10}, which is the value where the perovskite with the chosen composition decomposes into a Ruddlesden-Popper phase and CoO [21]. This aspect was not investigated further, as it was out of the scope of this study.

4.3.3 XPS analysis

4.3.3.1 Description of the acquired XPS spectra

The purpose of the XPS analysis was to investigate both compositional variations at the surface of the LSCF electrode and BE shifts due to the applied polarization. Four different photon energies, namely 930 eV, 755 eV, 490 eV and 325 eV were chosen. The choice was motivated by the optimal photon flux ranges of the monochromator, as well as by a compromise between obtaining similar information depths for the different elements while containing the number of different energies, since for each energy change an Au reference spectrum had to be acquired for calibration. The chosen energies resulted in two main inelastic mean free path (IMFP) ranges for the emitted photoelectrons, namely 5.5-8.5 Å and around 15-16.5 Å.

The selected spectra, seen in the following Table 4.1 as the red lines, were fitted (curves with other colors) using the software CasaXPS [101] with a combination of 70% Gaussian and 30% Lorentzian peak shape function (the so-called GL(30)), which is common in XPS studies. The following fitting constraints for each spectrum were used, according to Moulder et al. [102] and to specific literature sources for the more complex spectra:

Table 4.1. Fitting constraints used for the analyzed XPS spectra.

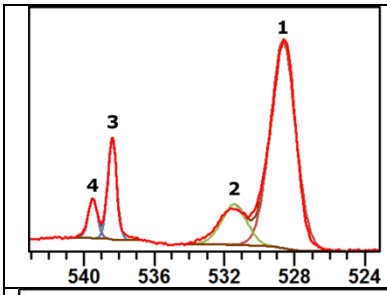	The O 1s lattice spectrum exhibited a main peak (1) and a secondary peak (2), attributed to a combination of adsorbates and surface sulfate, with a ~3 eV separation from the main peak. The only constraint which was applied was an equal FWHM between the two peaks. Also the gaseous O2 spectrum exhibited a characteristic doublet, represented by peaks 3 and 4 [103,104], which was similarly fitted with the only constraint of the same FWHM.
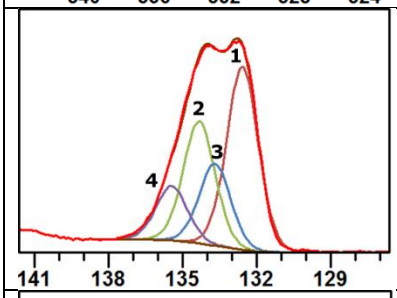	The Sr 3d spectrum exhibited a composite form attributed to two Sr $3d_{5/2\text{-}3/2}$ doublets, one belonging to the lattice Sr (peaks 1 and 2) and one belonging to surface Sr oxide and/or sulfate (peaks 3 and 4). Each doublet was fitted using the orbital splitting ratio of 2:3 for the d-orbitals, a peak separation of 1.75 eV and the same FWHM. The same procedure was applied in [105].
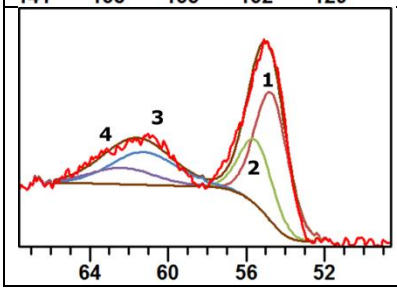	The Fe $3p_{3/2\text{-}1/2}$ (peaks 1 and 2) and Co $3p_{3/2\text{-}1/2}$ (peaks 3 and 4) spectra were acquired together, given their very close binding energies. For both spectra, the orbital splitting ratio of 1:2 of the p-orbitals was used. The peak separation was set to 0.8 eV for Fe and to 1.1 eV for Co, and the FWHM of each peak in the two doublets was set to be the same. The chosen parameters were selected using [106].

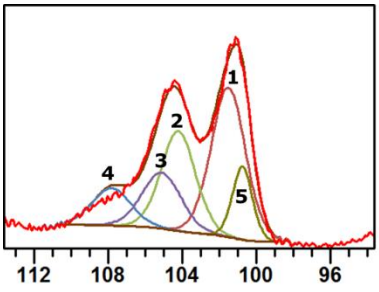	The La 4d spectrum represented a more complicated convolution of peaks. Besides the La $4d_{5/2\text{-}3/2}$ peak doublet (peaks 1 and 2), a doublet of satellite peaks (3 and 4) and the Si 2p peak (5) were all taken into account for an accurate fitting. For the 4d and the satellite peak doublets, the used orbital splitting ratio was 2:3 and the separation was set to 2.7 eV. The separation between each peak and its satellite was set to 3.6 eV according to [107,108]. The FWHM of each peak in the doublets was set to be equal. The Si2p peak was added without constraints and accounted for the additional area around 101 eV in BE.
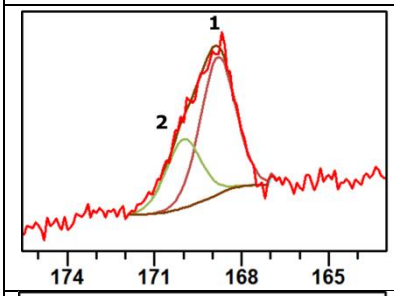	The S $2p_{3/2\text{-}1/2}$ spectrum also exhibits a peak doublet, which was fitted using the p-orbital splitting ratio of 1:2 and a peak separation of 1.18 eV. The FWHM of the two peaks was set to be the same.
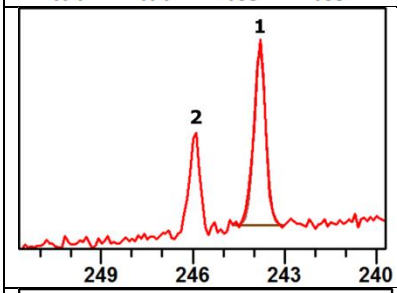	Since the two peaks in the Ar $2p_{3/2\text{-}1/2}$ spectrum are well-separated, only the $2p_{3/2}$ peak (1) was fitted for simplicity, therefore without the need for any constraints.
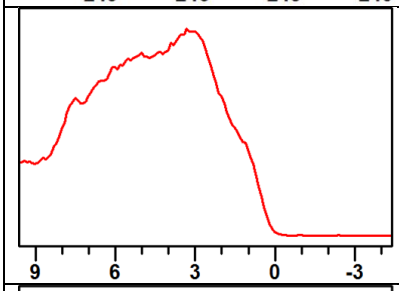	The valence band (VB), which as the name suggests consists of a convolution of low-energy photoelectrons originating from the valence levels of the surface atoms, was acquired but not fitted with any shape function. Instead, the shoulder at the lowest binding energies was fitted with a linear function and its intercept with the BE-axis was calculated for each spectrum.
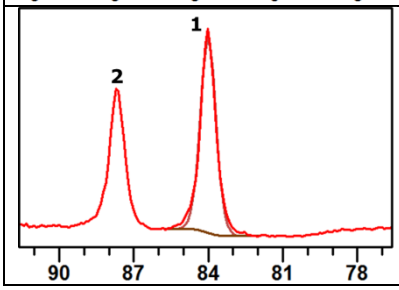	The Au $4f_{7/2\text{-}5/2}$ spectrum was acquired as a reference for each photon energy, polarization value and pO_2 that was used. This was necessary in order to eliminate measurement errors and ensure that the measured peak shifts were correct. The $4f_{7/2}$ peak (1) was fitted and the energy offset to 84 eV was calculated. The so-determined offset was then applied also to all other spectra acquired at the same conditions.

4.3.3.2 Peak shifts with polarization

After applying the correction factor obtained from the Au $4f_{7/2}$ peak, the peaks of all elements still exhibited small shifts, which varied with the applied polarization. As an example, the O 1s spectra acquired at positive and negative polarizations of 600 mV are shown in the following Figure 4.7. These spectra were chosen as an example, because they contain information both about the lattice and the gas phase.

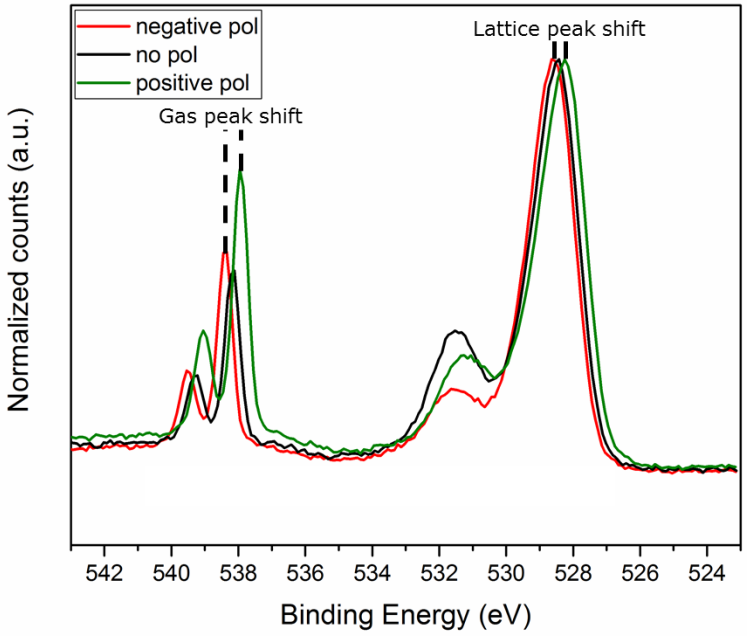

Figure 4.7. Peak shifts observed in the O 1s spectra under polarization in 1.3 mbar O_2.

The peak positions of all probed core electron spectra were mapped as a function of the applied polarization, and their slope was analyzed by linear regression and presented in Figure 4.8. The shifts of all of the lattice peaks except for Co exhibit a slope close to -1 eV/V, For Co the signal-to-noise ratio was too poor for a reliable peak fitting. All peaks showed two apparently different slopes, with the changing point at -0.1 V. Since the change was more evident for the Sr 3d and the VB intercept, the corresponding plots were fitted both with a single line and with two separate lines. The complete set of linear regression results are listed in Table 4.2.

It has been shown that a rigid BE shift of the core levels (slope of -1 eV/V) can be attributed to a shift of the Fermi level inside the band gap of the material with the applied polarization[98,100]. When oxygen vacancies are the majority charge carriers in the material , the BE shifts should exhibit a slope of -1 eV/V vs the applied overpotential [99], as is the case in this study.

The peaks corresponding to the gas phase exhibited a distinctly different behavior, as displayed in Figure 4.9 a and c. In this case, the slope of the BE shifts versus applied polarization was close to -1.5 eV/V. The change in the surface work function of the LSCF film, $-\Delta\Phi_S$, probed here through the BE shift of the gas species, relates to the change in the chemical potential of the electrons in the near surface region of the LSCF film, $\Delta\mu_e$,

a possible space charge potential change, $\Delta\psi_{SC}$, and the change in surface potential, $\Delta\chi$, through the following equation [98]:

$$-\Delta\Phi_S = \Delta\mu_e + e\Delta\psi_{SC} + e\Delta\chi \quad 4.2$$

where e is the electron charge. $\Delta\mu_e$ corresponds to the inding energy shift of the lattice species, probed experimentally here. The change in space charge potential, $\Delta\psi_{SC}$, with applied polarization does not appear to have a significant contribution in this case, since the BE shifts probed at different information depths for Sr and for the VB maximum do not show any substantial difference, and is thus assumed to be zero. The surface potential change, $\Delta\chi$, can therefore be deduced from Eq. 4.2, by substituting the binding energies and rearranging its terms, resulting in:

$$\Delta\chi = \frac{BE_{gas} - BE_{lat}}{e} \quad 4.3$$

To determine $\Delta\chi$, the O_{1s} lattice peak BE was subtracted from the corresponding gas peak BE and from the Ar_{2p} peak BE. In order to simplify the analysis of the shifts, the value without polarization was subtracted from all the others, obtaining the plots shown in Figure 4.9 b and d, which all pass through (0,0). In both cases the $\Delta\chi/\eta$ slope appears to be close to -0.5 eV/V. Also in this case, the results of linear regression analysis are listed in Table 4.2.

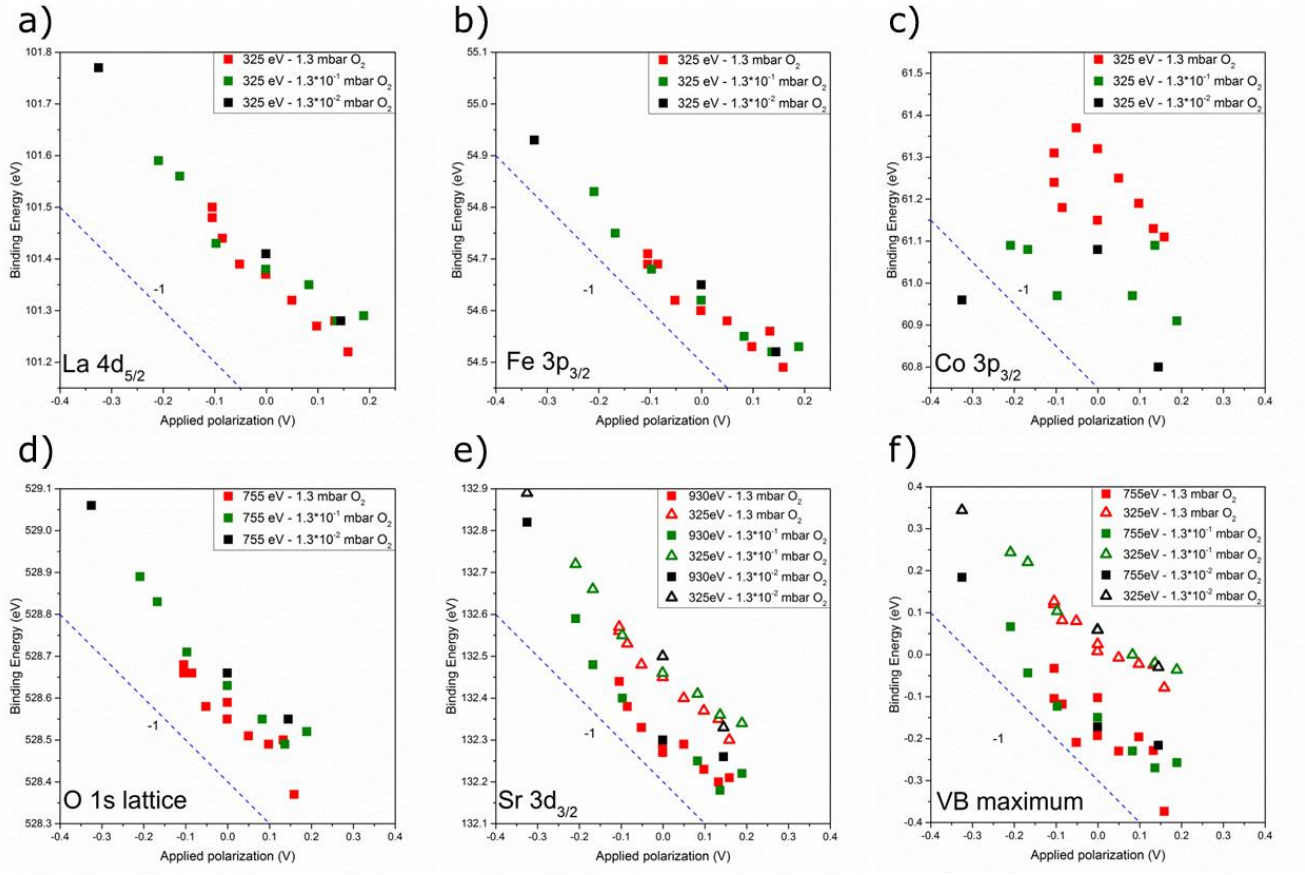

Figure 4.8. BE shifts of the lattice species versus applied polarization. The dashed line represents a slope of -1.

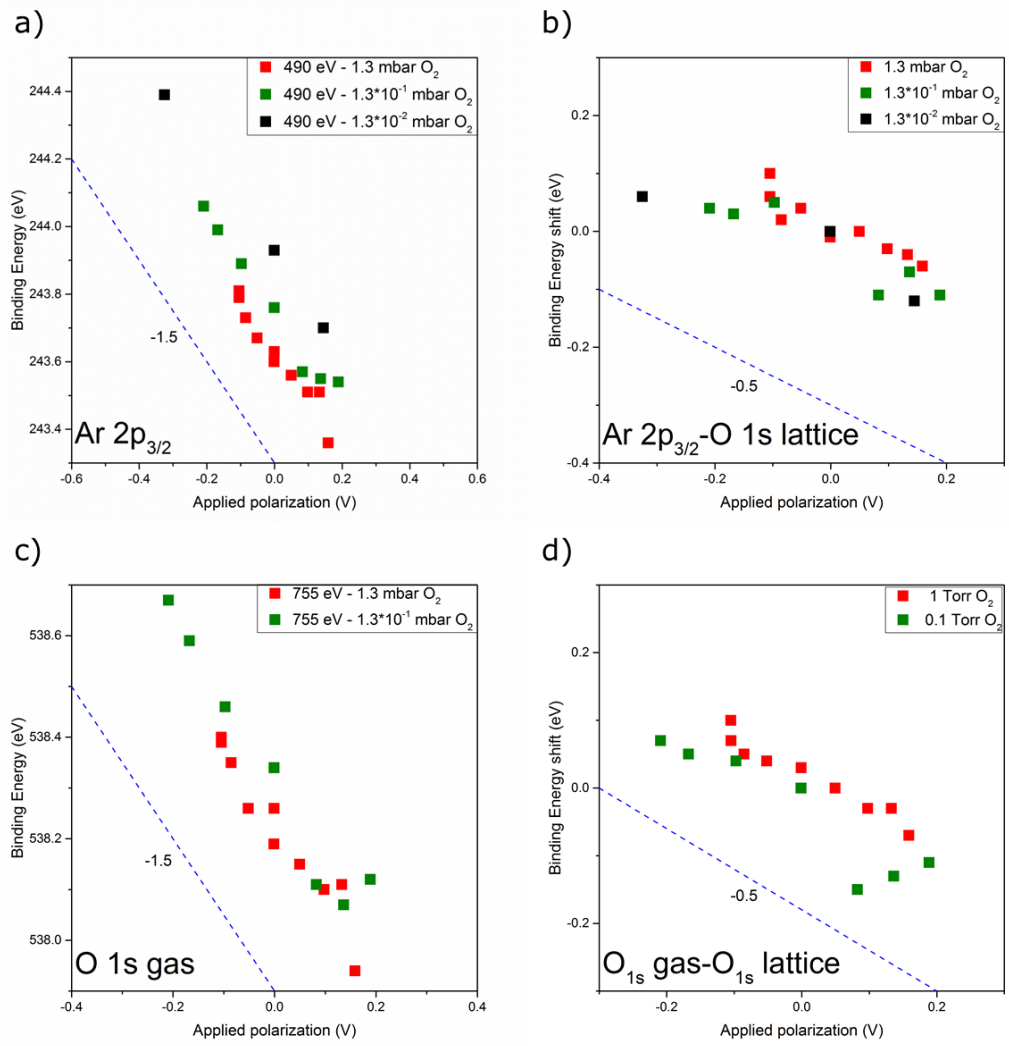

Figure 4.9. a), c) BE shifts of the gas species and b), d) their difference from the lattice oxygen BE versus applied polarization. The dashed lines represent slopes of -1.5 and -0.5 respectively.

Table 4.2. Fitting results (in eV/V) for all analyzed peak shifts. The values marked with * were obtained using only 2 data points, making it impossible to estimate an uncertainty.

	1 Torr	0.1 Torr	0.01 Torr
La_{4d} - 325 eV	-0.93±0.07	-0.78±0.09	-1.05±0.05
Fe_{3p} - 325 eV	-0.71±0.07	-0.75±0.08	-0.87±0.01
Co_{3p} - 325 eV	-0.55±0.25	-0.25±0.19	-0.22±0.54
O_{1s} -755 eV	-0.93±0.11	-0.99±0.10	-1.11±0.11
Sr_{3d} - 325 eV	-0.93±0.05	-0.95±0.07	-1.19±0.01
Sr_{3d} - 325 eV - neg	-1.05±0.19	-1.26±0.11	-1.20*
Sr_{3d} - 325 eV - pos	-0.89±0.07	-0.66±0.06	-1.17*
Sr_{3d} - 930 eV	-0.85±0.10	-0.94±0.12	-1.26±0.31
Sr_{3d} - 930 eV - neg	-1.46±0.23	-1.32±0.19	-1.60*
Sr_{3d} - 930 eV - pos	-0.53±0.13	-0.52±0.25	-0.27*
VB - 325 eV	-0.68±0.06	-0.72±0.07	-0.81±0.06
VB - 325 eV - neg	-1.04±0.16	-0.94±0.18	-0.88*
VB - 325 eV - pos	-0.48±0.11	-0.51±0.08	-0.60*
VB - 755 eV	-0.80±0.20	-0.76±0.10	-0.89±0.19
VB - 755 eV - neg	-1.33±0.55	-0.97±0.31	-1.10*
VB - 755 eV - pos	-1.02±0.40	-0.61±0.19	-0.30*
O gas	-1.44±0.14	-1.55±0.16	-
O gas-O_{1s} lattice	-0.51±0.05	-0.56±0.10	-
Ar gas	-1.38±0.12	-1.41±0.10	-1.46±0.04
Ar gas - O_{1s} lattice	-0.45±0.07	-0.42±0.08	-0.35±0.15

In order to assess how much of the gaseous atmosphere was affected by the surface potential, and thereby verify that the BE shifts in the gas phase correspond to the surface potential changes, as suggested by Feng et al. [98], an Au foil was placed on the sample holder and an electric potential was applied between the electron analyzer and the Au foil. The BE shifts of the Au peak and that of the Ar peak were monitored for polarizations ranging between -1 V and +1 V (Figure 4.10). As can be seen, the Ar peak shift varied linearly with the applied polarization, yielding a correction factor that can be applied to the measured shifts to obtain the change in surface potential. The correction factor is given by the ratio between the Au shift and the Ar shift slopes and corresponds therefore to 1.2.therefore, after applying the so-obtained correction factor, the $\Delta\chi/\eta$ value ranges between -0.4 and -0.7 eV/V.

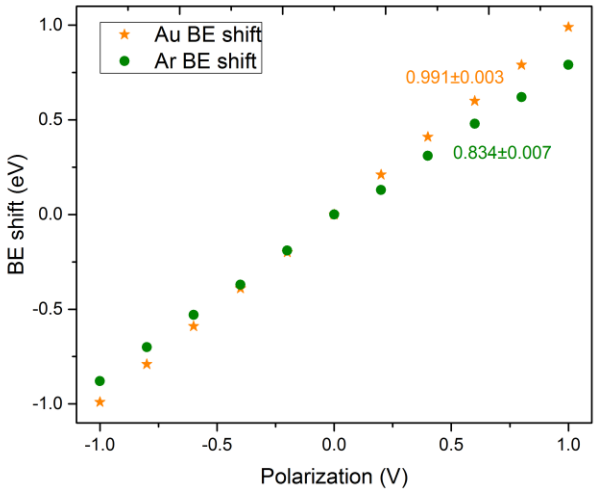

Figure 4.10. Au and Ar BE shifts calibration under polarization between the Au foil and the electron analyzer The slopes from the line fits are indicated for each peak shift.

4.3.3.3 Tracking surface chemical composition variations through the observed peak ratios

The area ratios of the main peaks associated with the LSCF components acquired at the same photon energy (325 eV) and of S and Si impurities versus respectively the Fe peak and the La peak acquired at the same photon energies (490 eV and 325 eV) were analyzed, in order to assess if polarization- or time-dependent variations in the near surface chemistry could be observed. It was chosen to compare them using the same photon energy rather than similar kinetic energies because the variation in the information depth did not change drastically, and more importantly the photon flux could be assumed to be the same for all spectra. As can be seen in Figure 4.11, both the La $4d_{5/2}$/Sr $3d_{5/2}$ peak area ratio and the A/B site ratio, calculated as the sum of the La $4d_{5/2}$ and Sr $3d_{5/2}$ peak areas over the sum of the Fe $3p_{3/2}$ and the Co $3p_{3/2}$ peak areas, show a time-dependent relaxation. This would be consistent with a mild progressive segregation of Sr to the surface, which becomes less pronounced as the pO_2 decreases. A similar behavior is seen for Si, again suggesting a progressive segregation to the surface.

The S content, on the other hand, seems to decrease with decreasing pO_2 and shows slightly higher values at positive polarization. No time effects could be observed in this case.

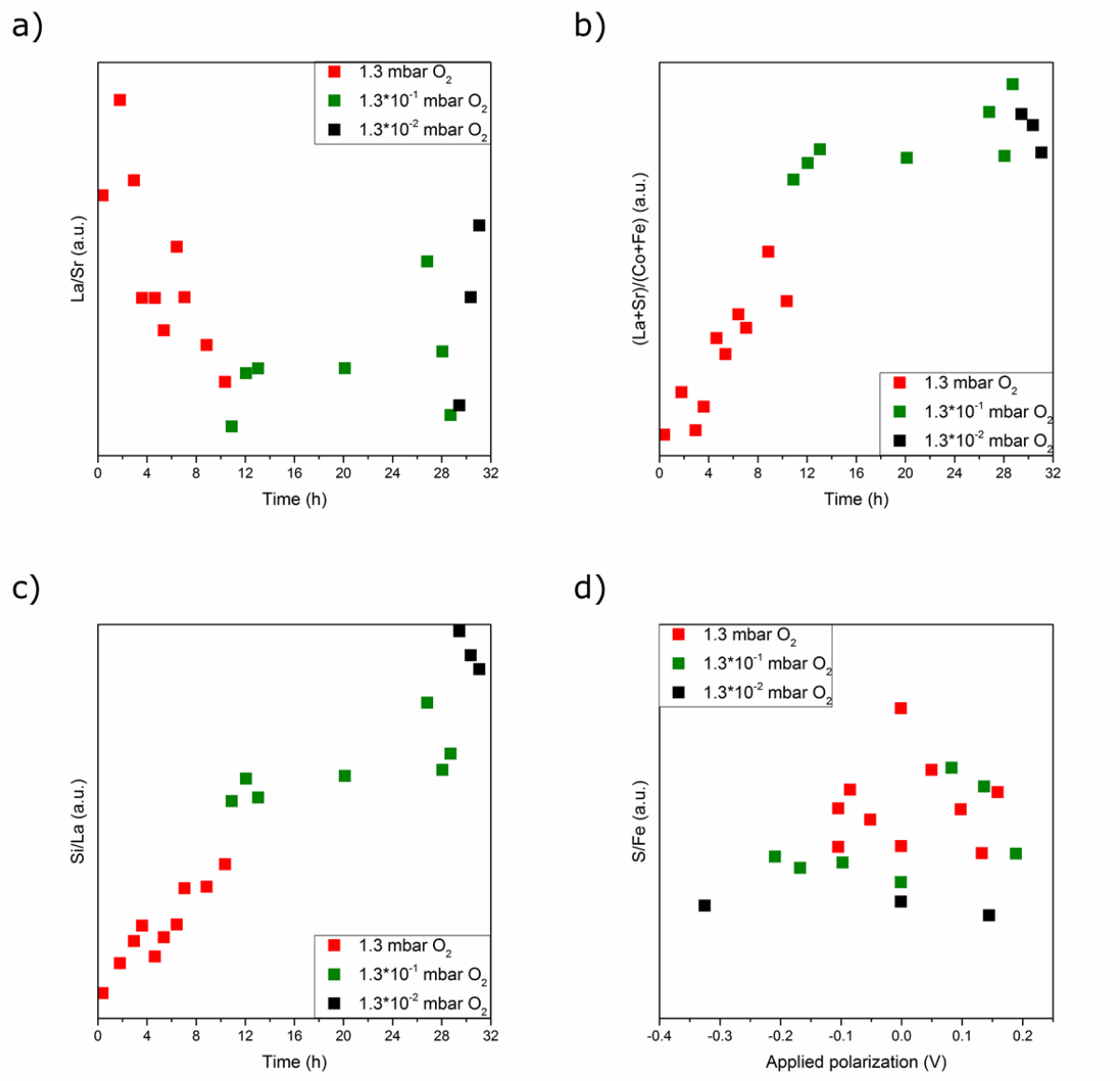

Figure 4.11. Peak area ratios between different species versus a), b) and c) time and d) polarization.

As mentioned in 4.3.3.1, both the O_{1s} and the Sr_{3d} spectra show a side peak component, attributed to adsorbed oxygen species and/or surface Sr oxide/sulfate, respectively. The side to main peak ratio was analyzed with respect to the applied polarization, resulting in the plots shown in Figure 4.12. The O_{1s} side peak shows an increasing importance with increasing *pO2* and positive polarization, which is compatible with an increased concentration of adsorbates under these conditions. The Sr_{3d} side peak is independent of polarization for the near-surface region (small information depth), while it appears to increase with polarization for the subsurface region (larger information depth). Additionally, the Sr_{3d} side peak is

independent of *pO2*. These observations suggest that the *pO2* and overpotential dependence of the O1s side peak is most likely associated with a varying concentration of adsorbed oxygen species at the surface.

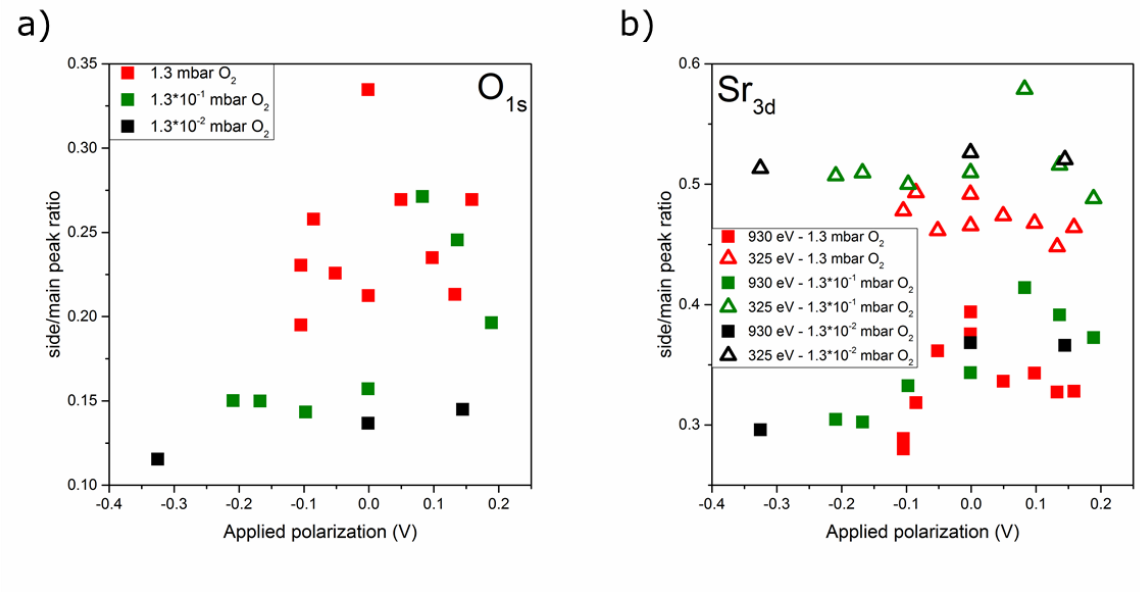

Figure 4.12. O and Sr side to main peak ratios versus polarization.

4.3.4 Post-testing characterization

4.3.4.1 ToF-SIMS of tested samples

Both the sample tested in the laboratory setup and the one tested in the beamline setup showed very similar distributions of impurities on the surface, although with slightly different intensities. Both samples showed an enrichment of Na and K, mostly outside the electrode area. On the film, the Na and K impurities were much lower and seemed to correlate to the underlying embedded Pt patterned CC grid (Figure 4.13). Similarly, both samples evidenced an enrichment of Cl and F on the surface, as well as presence of S (Figure 4.14).

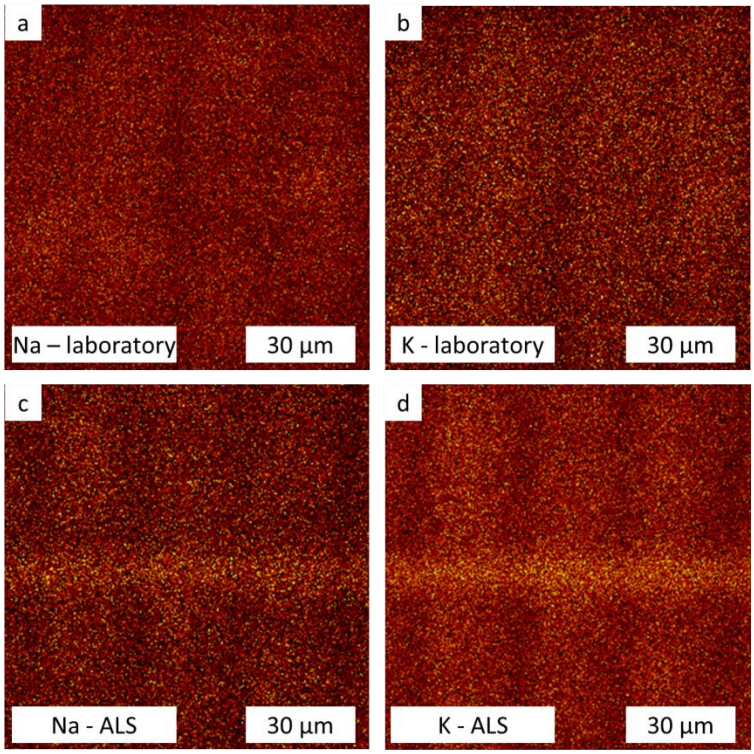

Figure 4.13. Na and K signal on the sample tested in the laboratory setup (a) and b)) and in the beamline (c) and d)).

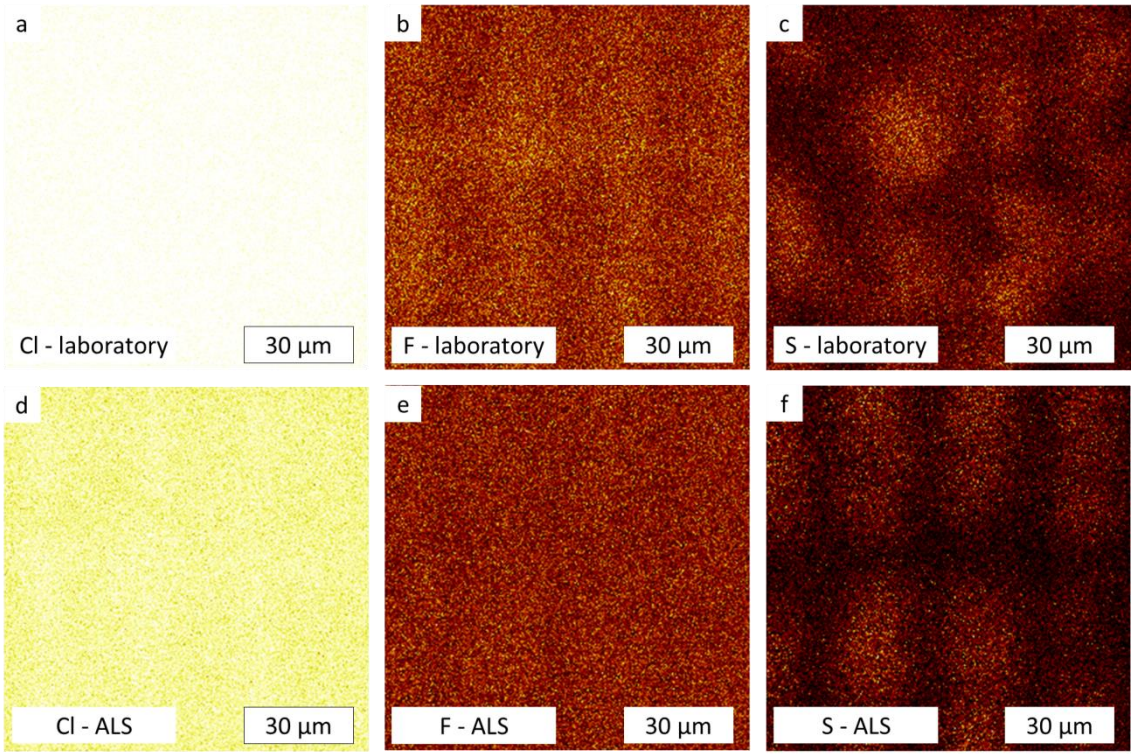

Figure 4.14. Cl, F and S signal on the sample tested in the laboratory setup (a - c) and in the beamline (d - f).

4.3.4.2 XRD after testing

Figure 4.15 shows the XRD spectra obtained on the two analyzed samples after testing, compared with the XRD spectrum obtained on the untested sample shown also in Figure 4.2. The sample tested in the laboratory setup only showed changes in the ratio between the YSZ (200) and (400) peak. For the beamline sample, however, a strong peak corresponding to the Pt (200) lattice plane appeared which might be caused by a crystallization of the Pt pattern under testing. Furthermore, a peak consistent with the SrO (220) peak also appeared.

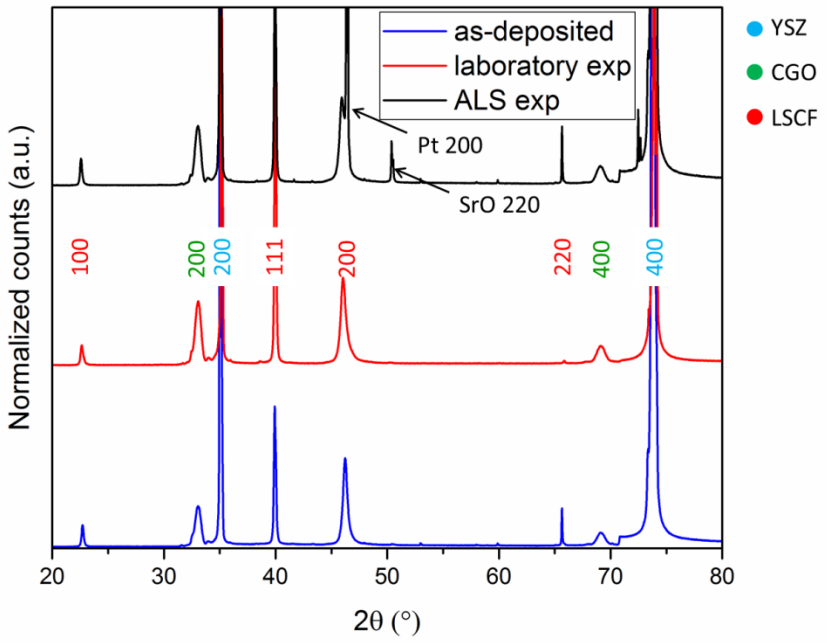

Figure 4.15. Comparison of XRD patterns of the as-deposited and tested samples.

4.3.5 SPEM analysis

4.3.5.1 Identification of lateral spatial inhomogeneities in near-surface composition

The sample which was tested in the ALS beamline 11.0.2 experiment was also used for further testing using the *in situ* NAP-SPEM at the Elettra ESCA Microscopy beamline. The chemistry of the sample surface was imaged with a lateral resolution of 150 nm, resulting in maps of the La4d, Sr3d and S2p intensity, and local spectra were obtained from selected positions on the LSCF film. This is the first time that this is realized *in situ* for model SOC electrodes at this level of spatial resolution.

The surface of the sample was investigated at room temperature and $5 \cdot 10^{-2}$ mbar O_2, to identify its surface composition. Islands where the La signal was lower and the Sr signal was higher were observed (Figure 4.16 a and c). Single spectra were also acquired on the positions of the Sr-rich islands and on the surrounding film (Figure 4.16 b and d). Motivated by the NAP-XPS results, the S spectrum was also acquired, in order to

investigate a correlation between the S and the Sr content (Figure 4.17). On the first two analyzed positions, marked A and B, the S spectrum was acquired as the last one. The peak was only weakly visible on position A, despite being a Sr-rich area on the map. For this reason, another island was chosen (C), and the S spectrum was acquired as the only one, resulting in a very clear peak. This behavior was a clear indication of the X-ray beam affecting the surface and removing the S contamination when illuminating one point of the sample for a prolonged period, which is necessary for the acquisition of spectra.

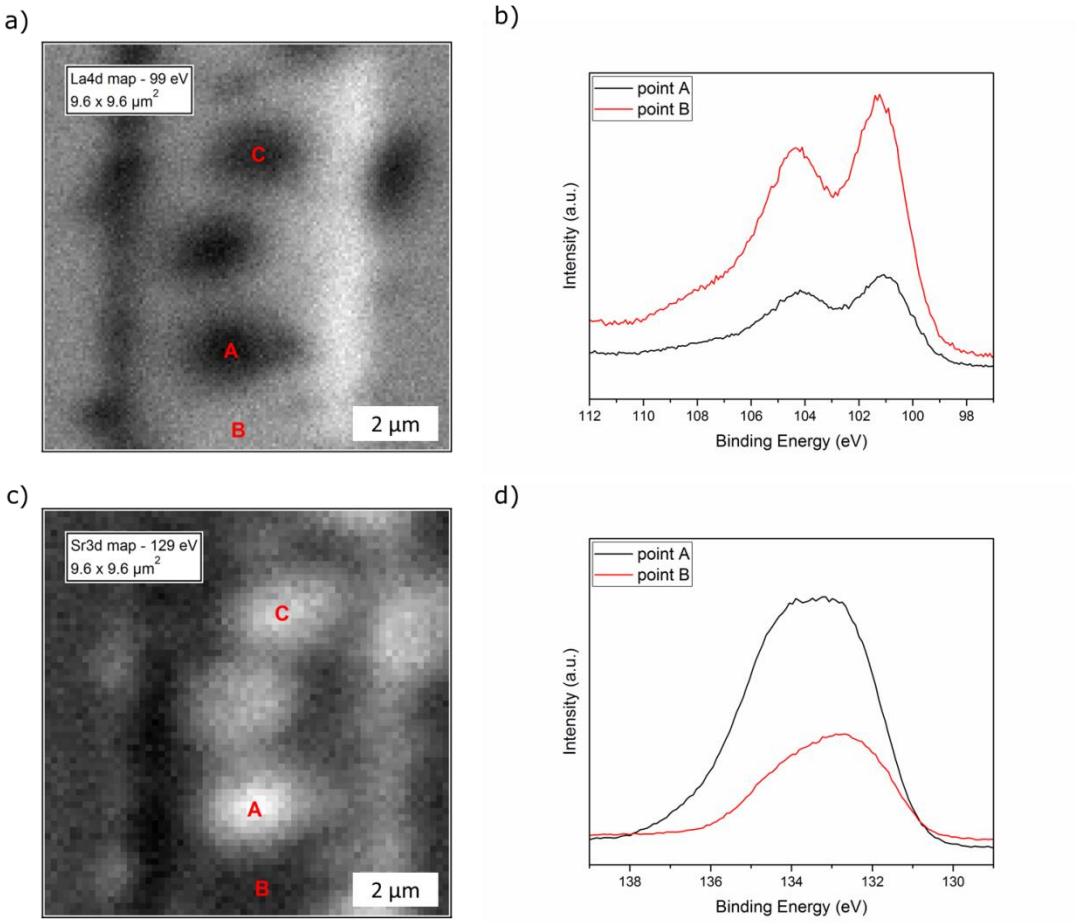

Figure 4.16. SPEM maps of a) La4d and c) Sr3d and spectra of b) La4d and d) Sr3d from the points A and B

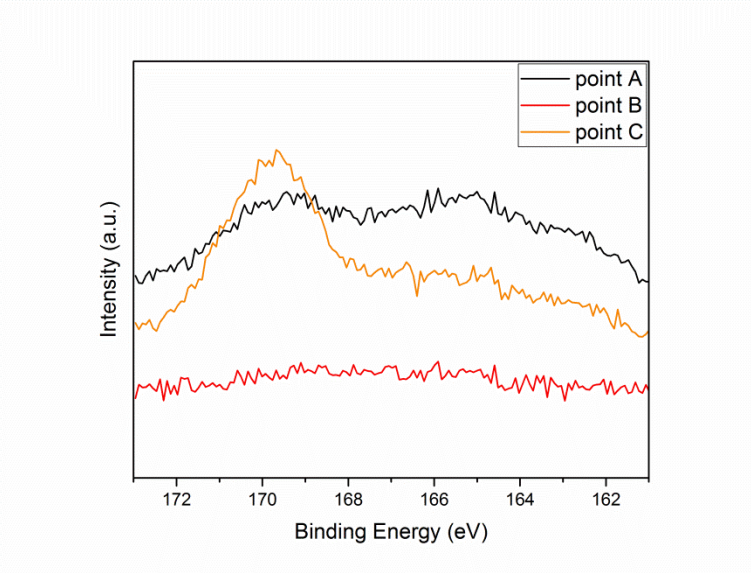

Figure 4.17. S2p spectra from points A, B and C identified on the SPEM maps in Figure 4.16.

The sample was then brought to 600 °C. The O_2 pressure was set to $2.6 \cdot 10^{-2}$ mbar and the sample was polarized both negatively and positively in order to assess the influence of temperature and polarization on the observed islands. Figure 4.18 shows that the islands remained the same for different polarizations.

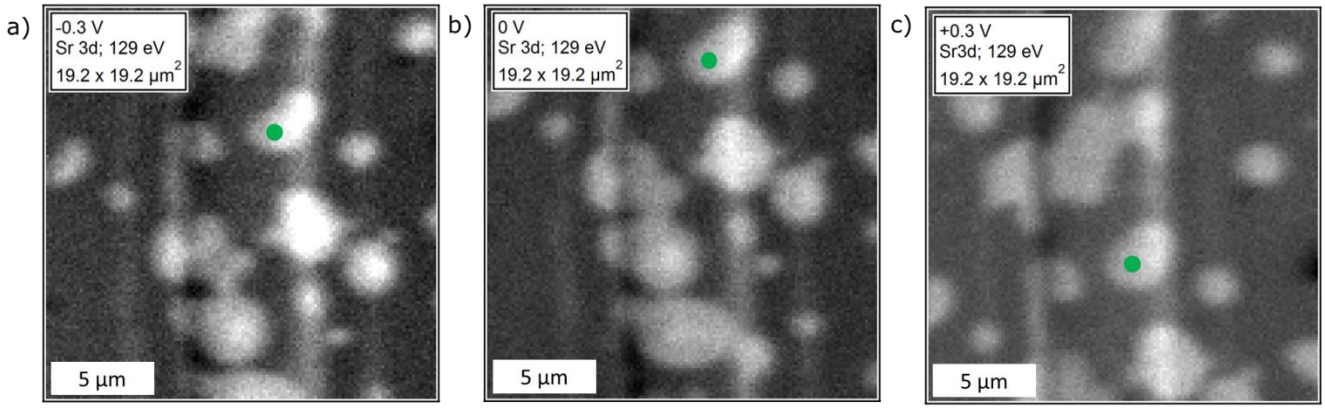

Figure 4.18. Sr3d maps at 600 °C with different polarizations.

Instead of using the spectra to determine the presence of S on the islands, since S spectra could not be observed at any polarization because of the beam-induced damage, mapping mode was used and the spectra extracted from the film areas were compared with the ones extracted from the island areas. An example can be found in Figure 4.19a and b, where the Sr and S maps are compared. In Figure 4.19c, spectra extracted from two different regions of Figure 4.19b are shown. The green square on the Sr map represents the position of the S map. In order to minimize the acquisition time of the S signal, and thereby increase the chances of acquiring the spectra, the S map was acquired on a smaller area and with a lower resolution.

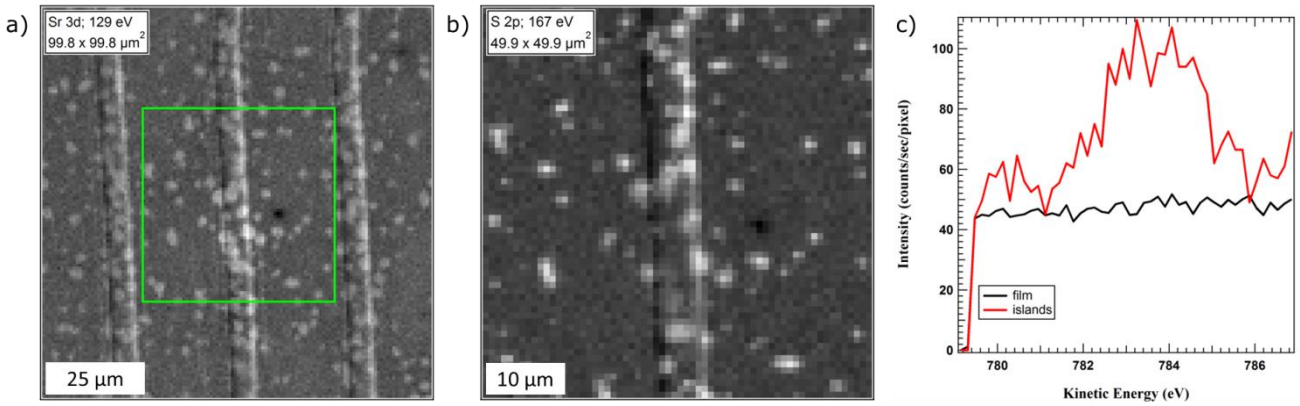

Figure 4.19. a) Sr map, b) S map and c) comparison between spectra in different positions on the S map.

Two important conclusions can be drawn from this investigation. First of all, the side peak contribution typically observed at the Sr3d core level spectra of LSCF (and associated perovskites) [105] can be attributed to the presence of Sr sulfate islands on the perovskite surface, rather than to the presence of surface SrO, which has been commonly assumed in the literature so far. Secondly, the X-ray beam is found to decompose the surface Sr sulfate islands into surface SrO islands, when combined with *in situ* probing at typical operating temperatures of 600 C, and in that way to clean the surface from S species. The importance of X-ray energy, beam intensity, atmosphere and polarization on the S-cleaning capacity of the beam remains unknown, as this was out of the scope of the current investigations.

Finally, H_2O was added to the gas mixture in equal amounts to O_2 (1:1 mixture, $2.5 \cdot 10^{-2}$ mbar each), in order to investigate its effect on the islands population. The electrode was kept at -300 mV for a 6 h period, and Sr maps were acquired at the beginning and at the end of the measurement. As can be seen from Figure 4.20, no change could be observed in these conditions either.

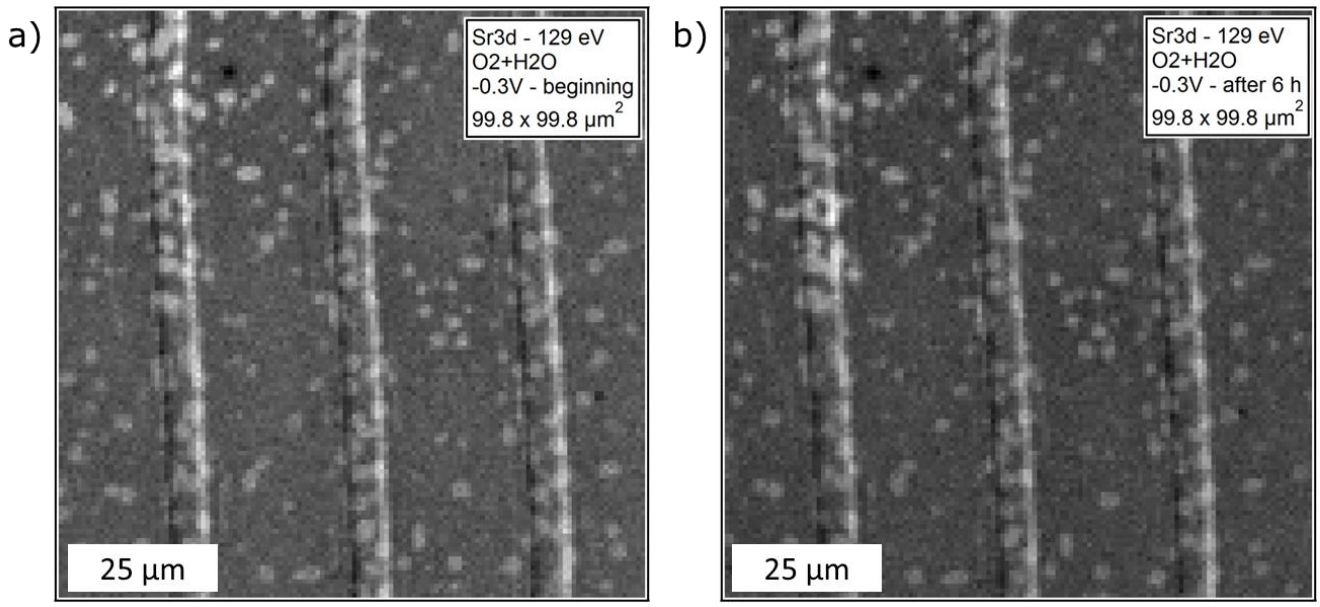

Figure 4.20. Sr 3d maps a) at the beginning and b) after 6 h of polarizing the sample with -300 mV in a 1:1 O_2-H_2O mixture at 600 °C.

4.3.5.2 Comparison with SEM

The sample was observed with SEM after the *in situ* NAP-SPEM experiments, in order to observe the features that were seen. When imaging the sample using only the secondary electrons, it was not possible to identify islands similar to the ones observed with NAP-SPEM (Figure 4.21a). When switching to the In-lens secondary electron detector, however, brighter spots composed of multiple nano-sized particles on the surface became obvious, resembling the ones observed with NAP-SPEM (Figure 4.21b). This suggests that the precipitated particles on the surfaceform only the outermost layers of the near-surface region. This was further confirmed when attempting to collect EDS spectra from the brighter spots, as it was impossible to distinguish them from the surrounding film (Figure 4.21c and d).

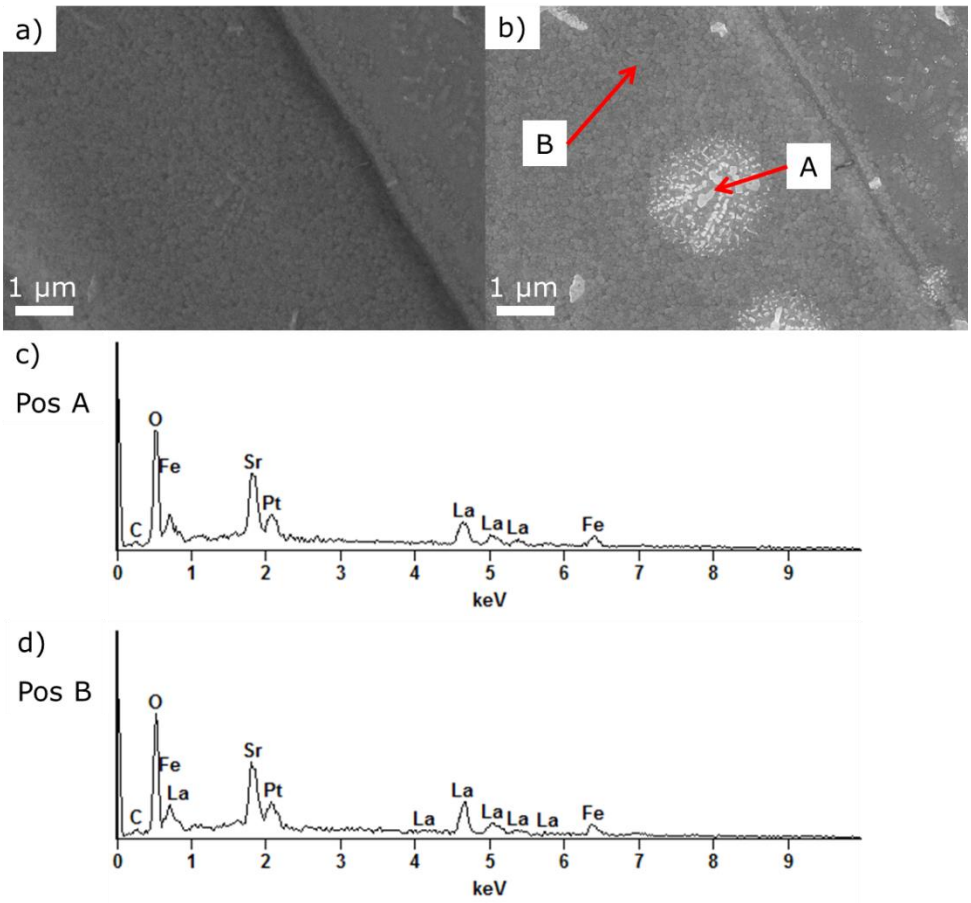

Figure 4.21. a) Secondary electron and b) in-lens SEM images of the sample tested in the beamline experiments, c) and d) EDS spectra obtained with a 10 kV electron beam from the islands and the surrounding film respectively.

4.4 Mechanistic interpretation of the oxygen incorporation

Guan et al. developed a model to interpret the current density associated with the oxygen incorporation reaction with respect to the oxygen partial pressure of the testing environment and the applied overpotential [109]. According to the developed model, the current density can be simplified with the following expression:

$$j \propto pO_2^{\frac{1}{n}} \cdot pO_{2,eff}^{\lambda} \cdot \exp\left(\frac{\left(\beta z - \frac{\gamma_{pre}}{n}\right) e\chi}{k_B T}\right) \quad 4.4$$

with

$$pO_{2,eff} = pO_2 \cdot \exp\left(\frac{4e\eta}{k_B T}\right) \quad 4.5$$

where *n* and λ are parameters which depend on the reaction mechanism and on the rate determining step (RDS), z is the total number of electrons/ions migrating through the gas-solid interface at the RDS, β is the

symmetry parameter of the RDS, γ_{pre} is the charge transfer coefficient that correlates the step preceding the equilibrium with the surface potential, χ is the surface potential, η is the overpotential, e is the electron charge, k_B is the Boltzmann constant and T is the temperature in Kelvin.

In particular, n indicates how many times the rate limiting step is repeated, while λ carries the contribution of all species (oxygen vacancies, electrons, holes,…) participating in the RDS and in the reaction following the RDS, and can be expressed as

$$\lambda = \sum_i \pm \left(\frac{\nu_{i1}}{n} + \nu_{i2}\right) \frac{\partial \ln a(i)}{\partial lnpO_2}|_{T,\eta} \quad 4.6$$

where i represents the species taken into consideration, ν_{i1} and ν_{i2} the coefficients of the considered species respectively for all steps before and at the RDS, $a(i)$ the activity of the considered species and the ± sign depends on which side of the reaction equation the considered species occupies.

By deriving the current density expression with respect to both η and pO_2, the following expressions can be obtained:

$$\frac{\partial lnj}{\partial lnpO_2}|_{T,\eta} = \frac{1}{n} + \lambda \quad 4.7$$

and

$$\frac{\partial lnj}{\partial \eta}|_{T,pO_2} = \frac{4e}{k_B T}\lambda + \frac{\left(\beta Z - \frac{\gamma_{pre}}{n}\right)e}{k_B T}\frac{\partial \chi}{\partial \eta} \quad 4.8$$

which can be simplified as

$$\frac{\partial lnj}{\partial \eta}|_{T,pO_2} = \frac{4e}{k_B T}\left(\lambda + \frac{\beta'}{4}\frac{\partial \chi}{\partial \eta}\right) \quad 4.9$$

if

$$\beta' = \left(\beta Z - \frac{\gamma_{pre}}{n}\right) \quad 4.10$$

Furthermore, the XPS results allowed a simplified correlation between χ and η, namely $\chi \sim \frac{1}{2}\eta$. This correlation was considered adequate for the sake of this study, but would need to be studied further in the higher pO_2 ranges. By substituting it in equation 4.9, an additional simplification could be made, obtaining

$$\frac{\partial lnj}{\partial \eta}|_{T,pO_2} = \frac{4e}{k_B T}\left(\lambda + \frac{\beta'}{8}\right) \quad 4.11$$

By fitting the $ln|I|$ versus η curves obtained from the EIS measurements in the laboratory and in the beamline, it was possible to determine an expression of $ln|I|$ at any given value of η as a function of $pO2$, and therefore calculate both partial derivatives seen in equations 4.7 and 4.11.

The results can be found in the following Table 4.3, Table 4.4 and Table 4.5, divided by experimental setup in the first two cases. Since the ALS results were obtained only at 2 pO_2 values, only the results of the laboratory experiments were used to calculate the values reported in Table 4.5.

Table 4.3. Partial derivatives over *η* calculated for the laboratory experiment.

pO_2 (mbar)	$\lambda + \frac{\beta'}{8}$
210	-0.425
14	-0.333
1.3	-0.194
$6.50 \cdot 10^{-1}$	-0.171
$1.30 \cdot 10^{-1}$	-0.088

Table 4.4. Partial derivatives over *η* calculated for the ALS experiment.

pO_2 (mbar)	$\lambda + \frac{\beta'}{8}$
1.3	-0.539
$1.30 \cdot 10^{-1}$	-0.260

Table 4.5. Partial derivatives over pO_2 calculated for the laboratory experiment.

η (V)	$\frac{1}{n} + \lambda$
-0.1	0.38085
-0.2	0.62812
-0.3	0.8754
-0.4	1.12268
-0.5	1.36996

As can be seen, in none of the cases a simple expression for any of the fitting parameters could be found. However, some simplifications can be implemented. In particular, the value of *n* can be assumed to be either 1 or 2, as the oxygen incorporation could occur through the adsorption of molecular O_2, and therefore the RDS would occur only once, or through the adsorption of atomic O, therefore repeating the RDS twice.

The possible values of λ as a function of η are reported in Table 4.6. As can be seen, all values shift towards the positive direction with increasing negative overpotential. The same trend can be observed for decreasing pO_2 values in Table 4.3 and Table 4.4, although the value of β' is unknown.

Table 4.6. Possible values of λ as a function of η calculated for the laboratory experiment.

η (V)	$\frac{1}{n}+\lambda$	$\lambda, if\ n=1$	$\lambda, if\ n=2$
-0.1	0.38085	-0.61915	-0.11915
-0.2	0.62812	-0.37188	0.12812
-0.3	0.8754	-0.1246	0.3754
-0.4	1.12268	0.12268	0.62268
-0.5	1.36996	0.36996	0.86996

In order to be able to identify possible candidates for the RDS, the defect chemistry of the LSCF surface with respect to the oxygen incorporation needs to be considered. In particular, the concentration of the oxygen vacancies and the holes needed to be determined, as they are the species participating in the oxygen incorporation on LSCF [110].

The hole concentration could be determined experimentally using O K-edge X-ray absorption spectroscopy (XAS). Two features, associated with the $e_g\uparrow$ and $t_{2g}\downarrow$ states of the oxygen valence electrons, could be observed when varying η, and thereby the effective pO_2 of the electrode surface. By integrating the area of the two features, and calculating their ratio, the hole concentration for all the range of effective pO_2 could be determined. Subsequently, by applying the charge conservation, the oxygen vacancy concentration could be calculated for all examined pO_2 values:

$$[V_O^{\bullet\bullet}] = \frac{[Sr'_{La}] - [h^{\bullet}]}{2} \qquad 4.12$$

The results are shown in the following Figure 4.22. The combined scatter plots of the three different pO_2 ranges were fitted with a polynomial curve, in order to obtain an estimate of their derivatives and thereby estimate the corresponding values of λ.

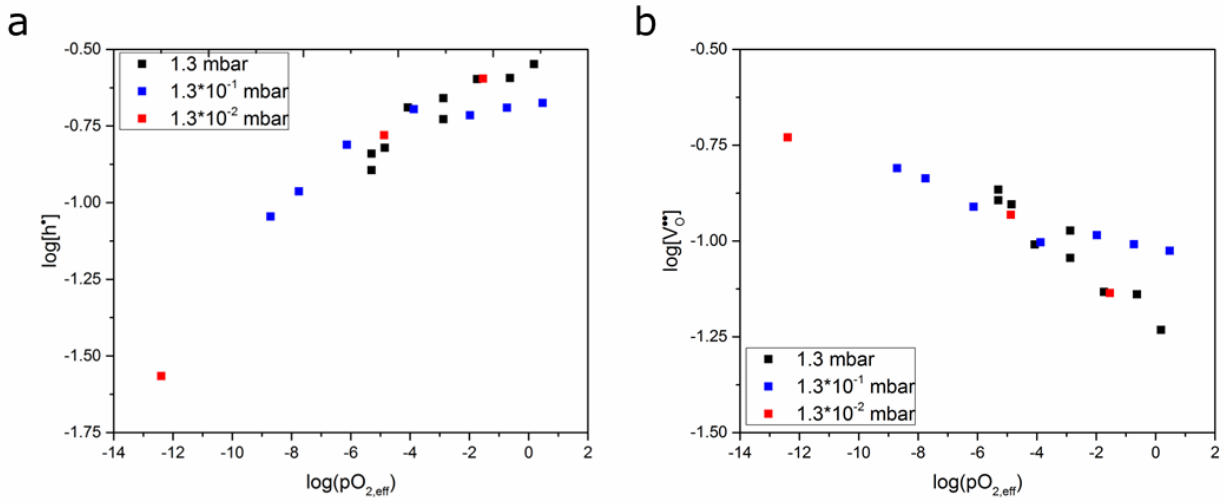

Figure 4.22. Plots of a) the hole concentration, determined in the ALS experiment with XAS and b) the oxygen vacancy concentration calculated from Equation 4.12versus effective pO_2.

The possible reaction steps of the two identified mechanisms are the following:

Atomic incorporation:

A-1 $$O_2 \rightleftharpoons 2O_{ad}$$ 4.13

A-2 $$2 \times (O_{ad} + V_O^{\bullet\bullet} \rightleftharpoons h^{\bullet} + O_O^{\bullet})$$ 4.14

A-3 $$2 \times (O_O^{\bullet} \rightleftharpoons O_O^{\times} + h^{\bullet})$$ 4.15

Molecular incorporation:

M-1 $$O_2 \rightleftharpoons O'_{2,ad} + h^{\bullet}$$ 4.16

M-2 $$O'_{2,ad} + V_O^{\bullet\bullet} \rightleftharpoons O_O^{\times} + O_{ad} + h^{\bullet}$$ 4.17

M-3 $$O_O^{\times} + O_{ad} + V_O^{\bullet\bullet} \rightleftharpoons O_O^{\times} + O_O^{\bullet} + h^{\bullet}$$ 4.18

M-4 $$O_O^{\times} + O_O^{\bullet} \rightleftharpoons 2O_O^{\times} + h^{\bullet}$$ 4.19

The possible values of λ were therefore calculated using the appropriate coefficients for the oxygen vacancies and holes for all identified steps (equation 4.6), and summarized in the following Table 4.7. As can be seen, all values shift towards more negative values with decreasing pO_2, contrarily to what was observed in the experimental data. However, all values are negative, which allows the determination of at least the type of pathway. When considering the possible values of λ listed in Table 4.6, namely, the atomic pathway requires positive values of λ for all values of η except -0.1 V. For the molecular pathway, however, λ is negative for all η values until -0.3 V, and turns positive only afterwards.

Table 4.7. Possible values of λ for all identified processes as the limiting step.

log(pO_2)	A1	A2	A3	M1	M2	M3	M4
2	0	-0.0158	-0.0386	-0.0114	-0.0272	-0.043	-0.0544
1	0	-0.0287	-0.0559	-0.0136	-0.0423	-0.071	-0.0846
0	0	-0.041	-0.075	-0.017	-0.058	-0.099	-0.116
-1	0	-0.0527	-0.0959	-0.0216	-0.0743	-0.127	-0.1486
-2	0	-0.0638	-0.1186	-0.0274	-0.0912	-0.155	-0.1824
-3	0	-0.0743	-0.1431	-0.0344	-0.1087	-0.183	-0.2174
-4	0	-0.0842	-0.1694	-0.0426	-0.1268	-0.211	-0.2536
-5	0	-0.0935	-0.1975	-0.052	-0.1455	-0.239	-0.291
-6	0	-0.1022	-0.2274	-0.0626	-0.1648	-0.267	-0.3296
-7	0	-0.1103	-0.2591	-0.0744	-0.1847	-0.295	-0.3694
-8	0	-0.1178	-0.2926	-0.0874	-0.2052	-0.323	-0.4104
-9	0	-0.1247	-0.3279	-0.1016	-0.2263	-0.351	-0.4526
-10	0	-0.131	-0.365	-0.117	-0.248	-0.379	-0.496
-11	0	-0.1367	-0.4039	-0.1336	-0.2703	-0.407	-0.5406
-12	0	-0.1418	-0.4446	-0.1514	-0.2932	-0.435	-0.5864
-13	0	-0.1463	-0.4871	-0.1704	-0.3167	-0.463	-0.6334
-14	0	-0.1502	-0.5314	-0.1906	-0.3408	-0.491	-0.6816

4.5 Discussion

For the first time, a correlation between the surface potential change and the applied overpotential on LSCF electrodes has been established, for the pO_2 range between $1.3 \cdot 10^{-2}$ and 1.3 mbar. The found correlation suggests that the surface potential changes with a factor of 0.5 with respect to the overpotential. This could have multiple explanations, as evidenced by Feng et al. [98]. One of the possible explanations could be a change in adsorbate coverage. The O_{1s} spectrum does not offer a clear interpretation of the presence or absence of adsorbates for different polarization values, since the observed side peak could be explained by surface Sr sulfate, as evidenced by SPEM. However, since the Sr side/main peak ratio appears to be independent on polarization and pO_2, it can be assumed that the Sr sulfate contribution to the O_{1s} side peak should be constant as well. Therefore, the changes in the O side/main peak ratios would be correlated with changes in the adsorbate coverage.

Another possibility would be a change in the surface layer structure due to the bonding of the adsorbates on the LSCF surface. However, also in this case the convolution of the Sr sulfate-related O side peak with the possible adsorbate peaks does not allow an identification of possible BE shifts of the adsorbate species. Therefore, a conclusive answer is out of reach at the time being.

Even though the origin of the correlation between surface potential and overpotential remains unclear, the established relation can nevertheless be used to attempt a mechanistic interpretation of the oxygen

incorporation reaction. Using the simplified expression $\Delta\chi \sim 0.5\eta$ and the procedure proposed by Guan et al. in [109], the pathway for the oxygen incorporation reaction from the measured I-V curves was deduced. The reaction appears to proceed through the molecular pathway, in accordance with the simulations performed by Wang et al. [27], but the precise determination of the RDS was not possible due to the discrepancy between the experimental data and the simulated parameters. The surface potential contribution resulted in only a very small contribution to the fitting of the I-V curves, therefore the result was considered sufficiently acceptable as a preliminary study.

Degradation was observed under prolonged testing in absence of polarization, and was partially recovered under cathodic polarization at low pO_2 values. Sr segregation towards the surface was observed, which could be one of the reasons for the degradation, as described in literature [74,91]. However, no significant change in the Sr oxide/sulfate to lattice Sr ratio was observed, which was also confirmed by NAP-SPEM, although on an already tested sample. This could be due to a simple reorganization of the surface layers which would keep the element ratios but organize the surface species into islands rather than continuous layers. In order to assess if the surface morphology changed in the first part of the experiment, NAP-SPEM should be performed on a pristine sample, and its evolution monitored over time.

Concerning the polarization and pO_2 dependence of the Sr sulfate island population and size, our *in situ* NAP-SPEM investigations suggest that there is no pronounced dependence on either of the two parameters, in the probed range of -300 to +300 mV of applied polarization, neither in $2.6\text{-}5\cdot10^{-2}$ mbar O_2 nor in H_2O+O_2. The formation of these islands is therefore likely depending on the abundance of S at the LSCF surface. This is in line with the results from the ALS-based measurements presented in Figure 4.12b, also suggesting a polarization and pO_2 independent Sr side peak/Sr lattice peak ratio. This conclusion is of great significance, as it supports the allocation of the polarization and pO_2 dependence of the O side peak/O lattice peak ratio to an increase in oxygen adsorbate coverage with increasing pO_2 and anodic polarization, an important conclusion in attempting to understand the observed overpotential dependence of the surface potential change and the mechanism of oxygen surface exchange on LSCF.

Finally, the sample tested in the beamline setup exhibited a 10 times better performance than the sample tested in the laboratory setup. The reason for this behavior is still unclear, but one hypothesis might lie in the different heating strategies in the two setups. While in the laboratory setup the whole sample environment is kept at the same temperature, allowing desorption of impurities from the Al_2O_3 components to the sample, in the beamline setup the sample is the only heated element and the experimental chamber is baked out in UHV after every experiment, resulting in the cleanest possible environment. This difference might explain the different performance in corresponding atmospheres in the two setups.

4.6 Conclusions

The oxygen reactions on LSCF electrodes were successfully studied employing electrochemical measurements far from equilibrium performed *in situ* both in laboratory and beamline experiments. The electrode performance was evaluated in terms of I-V curves at different pO_2 values, and was correlated with the surface chemistry of LSCF under operation, as measured in two separate beamline setups.

In both cases, the presence of surface Sr and S containing islands was observed, without exhibiting large variations with respect to atmosphere or polarization. A shift in the binding energies of both the core levels and the valence band was observed, consistent with a shift of the Fermi level inside the band gap of LSCF.

For the first time a shift in the surface potential with varying overpotential was experimentally determined for LSCF for pO_2 values between 10^{-2} and 1 mbar, allowing a derivation of the oxygen incorporation reaction mechanism from the I-V curves at varying pO_2, and the determination of a probable reaction pathway.

In order to corroborate the results, further measurements at higher pO_2 values will need to be performed, extending the surface potential – overpotential correlation to real operating conditions, and thereby verifying the assumptions made from the results obtained at lower pO_2.

5 Mapping of SOC potentials using SPEM

5.1 Introduction

The electrodes in SOCs possess complex composite microstructures in order to enhance the active area for the electrode reactions and thereby reduce the overpotential losses. However, this introduces chemical and morphological inhomogeneities, which complicate their characterization and the study of the processes occurring in the electrodes and at the electrode-electrolyte interfaces. The characterization of the electrodes is further complicated by the possibility of complex distributions of the electromotive potential (π) in the electrodes and the Galvani potential (φ) in the electrolyte, resulting in overpotential distributions (defined as $\eta=\pi-\varphi$) that cannot be investigated with conventional analysis techniques [9,111]. Finally, the electrode and electrolyte materials undergo chemical modifications under operation, which can be accelerated both by the high operating temperatures and by the local overpotentials.

It is therefore important to be able to investigate all these factors at once, with techniques that are sensitive to the surface chemistry and to the electric potentials and are capable to provide time-resolved information, while probing the SOC materials at (or close to) their relevant operating conditions.

In this study, model electrodes in the form of GDC and LSCF thin films arranged in a planar cell setup were designed, with the specific goal of realizing a simplified model system that could reproduce the chemistry of realistic composite electrodes. Since LSCF is a MIEC, the oxygen reactions will occur on the whole surface of the electrodes rather than only at the three phase boundary with the gaseous environment and the GDC electrolyte. In order to be able to study both the LSCF and the GDC behavior under the presence of an electric potential difference, simulating the operation in SOFC or SOEC mode, the electrodes were patterned, exposing regions of the underlying electrolyte. This allowed monitoring the chemistry of both the electrode and the electrolyte materials under operation, while evaluating the distributions of π and φ using NAP-SPEM.

5.2 Experimental

5.2.1 Sample preparation

For the sample used in this study, a 50-100 nm film of GDC followed by a 450 nm film of LSCF were deposited by PLD on 10x10x0.5 mm^3 $NdGaO_3$ (NGO) substrates with (110) orientation (Crystal GmbH, Germany). NGO is widely used as a substrate for model PLD studies because it is an electronic and ionic insulator and it has been proven to have a good lattice parameter compatibility with GDC and LSCF [81].

After the PLD, the samples were spin-coated with positive photoresist (S1818, MicroResist Technology GmbH) and exposed subsequently to UV light through two differently patterned photomasks, using a Karl Suss MJB-3 mask aligner: the first pattern consisted of a 10 µm line, that was aligned with the center of the sample (Figure 5.1a), while the second pattern was an array of holes, placed in a square symmetry, with diameters of 10 µm and spacing between their centers of 20 µm (Figure 5.1b).

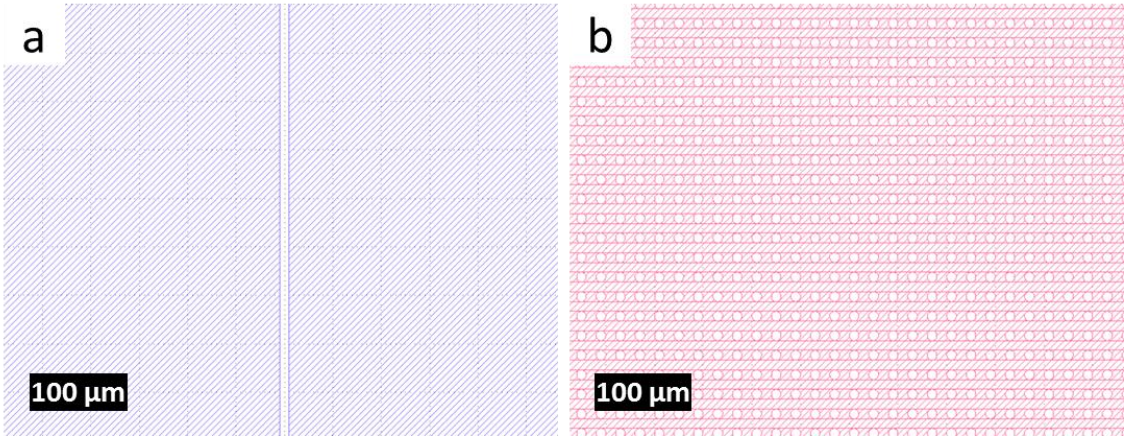

Figure 5.1. Photomasks used for the sample production.

After developing the photoresist by dipping the sample in the appropriate developer solution (MF-319, MicroResist Technology GmbH), the sample was characterized by AFM to study the morphology of the remaining photoresist layer. As can be seen in Figure 5.2a, the photoresist layer had not been completely developed on the central line. The sample was therefore exposed to oxygen plasma in a Fischione Model 1020 plasma cleaner, periodically examining the sample with AFM, until the desired morphology was observed, as visible in Figure 5.2b.

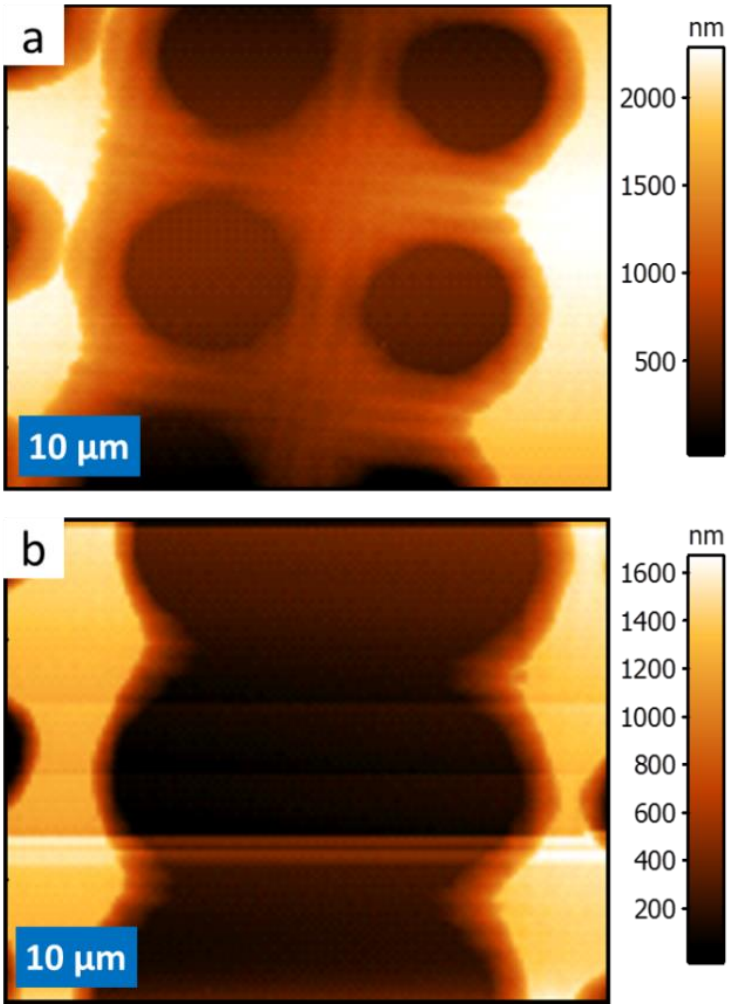

Figure 5.2. AFM images of the photoresist layer a) after UV-light exposure through the two photomasks described in the text and development and b) after subsequent oxygen plasma treatment.

Subsequently, the LSCF layer was removed through the openings in the photoresist using Ar-ion etching (Oxford Instruments Ionfab 300). The sample was exposed to a 30 cm ion beam, generated from an Ar-plasma obtained with a radiofrequency (RF) field of 400 V and 500 mA, and accelerated with 400 V. Since Ar-ion etching is a physical etching procedure which can etch all types of material, albeit at different speeds, the sample was periodically observed through an optical microscope to determine the necessary time for complete etching of the LSCF layer.

Finally, the sample was cut to a 4·8 mm^2 rectangle using a diamond coated saw (Struers Minitom) in order to be better suitable for the planned SPEM measurements. Afterwards, the remaining photoresist was removed first with acetone (analytical grade, Emsure – Sigma Aldrich) and then with isopropanol (99.5%, Alfa Aesar), before removing all remaining traces of organic material using oxygen plasma cleaning for 10 minutes (Fischione Model 1020).

5.3 Results

5.3.1 Characterization of pristine sample

5.3.1.1 SEM-EDS, AFM and ToF-SIMS

The sample was analyzed with SEM, exhibiting the expected surface microstructure, namely perforated planar electrodes separated by a 20-25 µm stripe, partially connected to the holes of one or both electrodes (Figure 5.3). EDS performed on the sample after Ar-ion etching showed the desired chemical composition, namely elements corresponding to the LSCF films on the electrode and elements corresponding to the GDC electrolyte in the holes and in the separation region. Figure 5.3a shows the topographic contrast between the patterned electrodes and the underlying CGO film as seen using the secondary electron (SE) detector, while Figure 5.3b shows the distribution of Sr and Figure 5.3c the distribution of Ce. Due to the low sensitivity of EDS, the presence of LSCF on the GDC areas could not be completely excluded, while on the other hand the Ce signal confirmed the presence of the electrolyte in the desired regions.

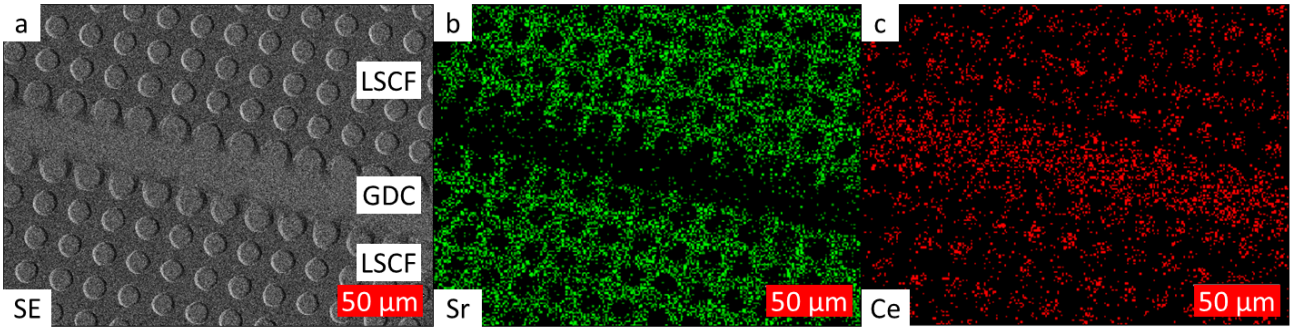

Figure 5.3. a) SEM secondary electron image and EDS mapping of b) of Sr and c) Ce on the sample after the Ar-ion etching.

ToF-SIMS provided a better-resolved and more importantly, surface sensitive elemental distribution, showing only the presence of GDC in the electrode holes and in the electrolyte region separating the two electrodes (Figure 5.4a), and LSCF on the electrodes; in particular, the La-signal (Figure 5.4c) showed an anomalous distribution, seeming to be affected by an edge enhancement of the signal, while the Sr-signal (Figure 5.4d) showed a more homogeneous distribution over the electrode surface. Notably, Na was also found in the GDC areas (Figure 5.4b).

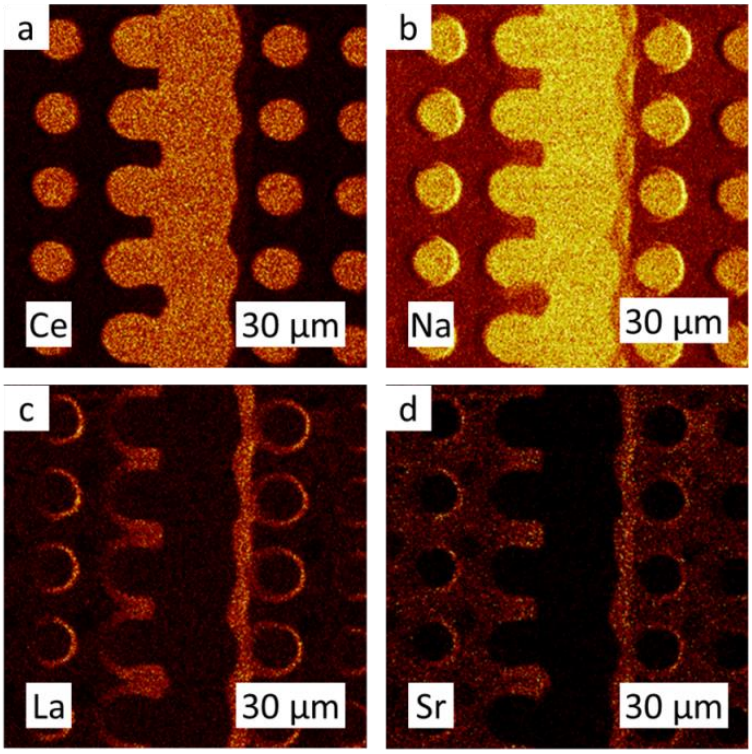

Figure 5.4. ToF-SIMS images of a) Ce, b) Na, c) La, and d) Sr on a region of the sample containing the electrodes and the electrolyte stripe.

5.3.2 SPEM analysis

The sample was placed inside the NAP-cell and was aligned under the optical microscope with the electrolyte region somewhat off-center so as to be able to access a large portion of one of the electrodes through the 400 µm X-ray pinhole, as shown in Figure 5.5a. The scratch visible in the bottom electrode did not extend over the whole electrode and therefore the two apparent sections were interconnected, as can be seen in Figure 5.5b. For this reason, and since the mounting process was time-consuming and delicate, the sample was not re-aligned. Throughout the study, the investigated positions below the electrolyte stripe will be considered positive, and the applied potential differences will be given as V_{bottom} - V_{top}.

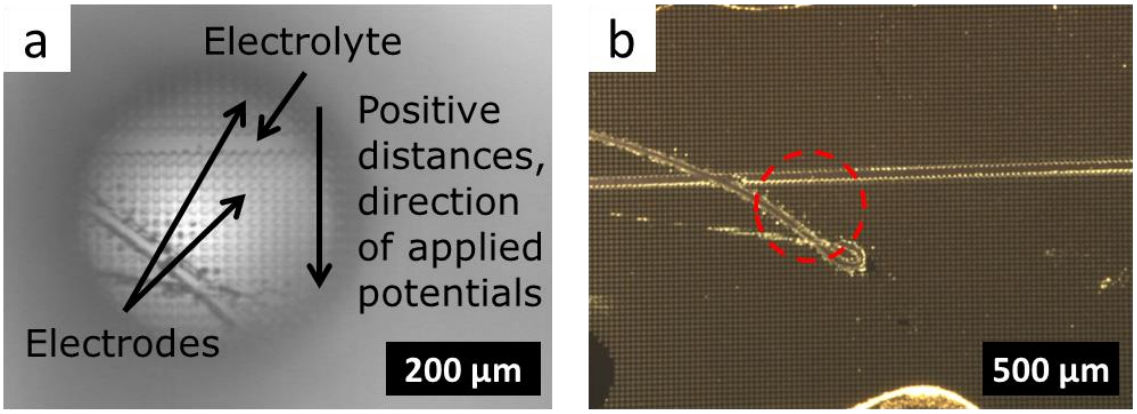

Figure 5.5. Optical images of the sample a) mounted inside the NAP-cell, as seen with an optical microscope through the X-ray pinhole and b) after removing it from the chamber. The red circle evidences the approximate position of the pinhole.

EIS was performed on the sample while applying the potential between the two electrodes, resulting in spectra like the ones visible in Figure 5.6. The two main features that could be identified were a high-frequency (HF) arc, associated with the GDC electrolyte stripe, and a low-frequency (LF) response which varied strongly with the applied potential difference, and was identified as the electrode response. Given the complex, and often poorly resolved shape of the LF part, only the HF arc was fitted in order to estimate approximate values of conductivity for the GDC film.

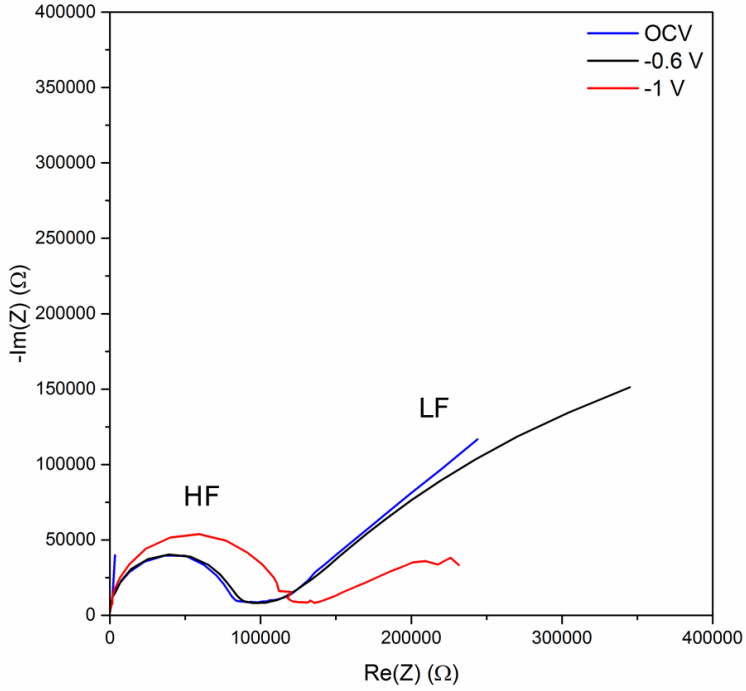

Figure 5.6. Impedance spectra recorded with different applied potential differences.

The sample was heated to approximately 600 °C for the electrochemical measurements. A temperature calibration of the heater was obtained previously using a thermocouple on a different sample with the same thickness. The precise temperature during the performed experiments could therefore not be known. However, the HF arc could be used to estimate the temperature of the sample, by assuming a simple geometry for the CGO electrolyte between the electrodes with a length of 20 µm, a width of 3.5 mm and a thickness of 50 nm. The conductivity values obtained with this strategy, ranging between $5 \cdot 10^{-3}$ and $2 \cdot 10^{-2}$ S/cm, were consistent with a sample temperature between 500 and 650 °C [112].

The pO_2 was monitored during the experiment, and its value was kept between $4.3 \cdot 10^{-2}$ mbar and $6.6 \cdot 10^{-2}$ mbar.

5.3.2.1 Microspectroscopy – XPS peaks

Four elements were chosen for the acquisition of localized spectra on selected points of the sample, namely Ce, O, La and Sr. Ce and O spectra were acquired on electrolyte areas, while O, La and Sr spectra were acquired on electrode areas. The XPS spectra, visible in the following Table 5.1 as the red lines, were fitted using the CasaXPS© software [101] with a variable number of 30%gaussian-70% lorentzian peaks (GL30), using constraints derived from Moulder et al. [102] and specific sources for each element.

Table 5.1. List of peaks and constraints applied to the XPS spectra.

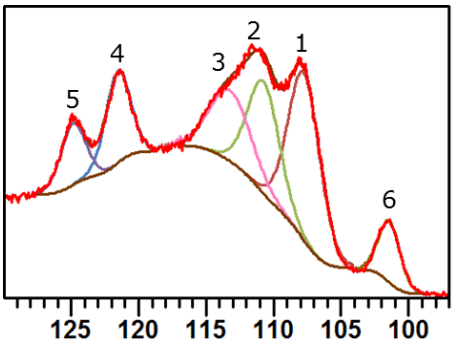	In the case of the Ce 4d spectrum, five peaks corresponding to Ce (1-5) and one corresponding to Si (6) were fitted, following the peak assignment by Mullins et al. [113,114], even though more complex assignments can be found in literature [115]. For the doublet peaks represented by peaks 1,2 and 4,5, a 3:2 area ratio was applied as a constraint for the d-orbital splitting, as well as a peak separation between peak 1 and 2 of 3 eV [102].
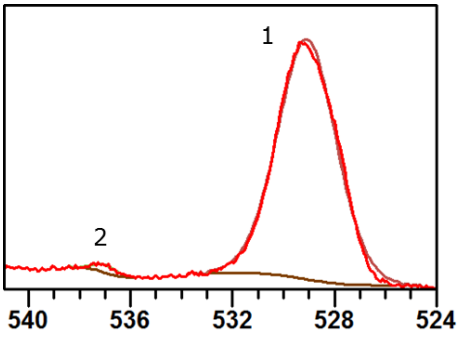	For the O 1s spectrum, the main peak (1) was identified, as well as a small, poorly resolved peak (2) likely belonging to the small amount of gas phase O_2 [103].

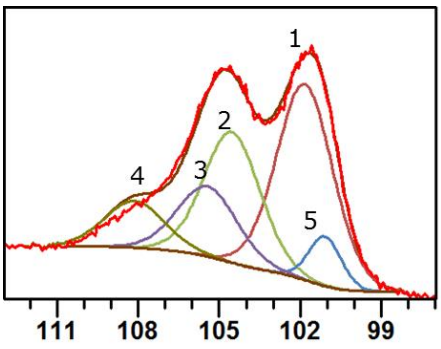	In the case of La, two main peaks corresponding to the La $4d_{5/2\text{-}3/2}$ states (1,2) and two satellite peaks (3,4) were identified [107], as well as a contribution from Si (5). Both for peaks 1,2 and 3,4 the same 3:2 area ratio was applied (d-orbital splitting). The separation between each of the coupled peaks (1,2 and 3,4) was set to 2.7 eV and the separation between each satellite peak and the corresponding main peak (1,3 and 2,4) was set to 3.6 eV.
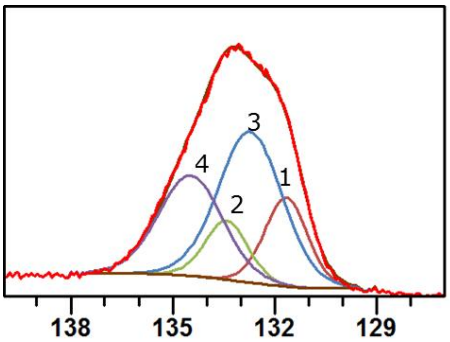	In the case of Sr, two peak doublets corresponding to the Sr $3d_{5/2\text{-}3/2}$ states, namely 1,2 and 3,4, were identified [105]. For both doublets, an area ratio of 3:2 (d-orbital splitting) and a separation of 1.75 eV were applied.

Besides the listed peaks, full surveys were acquired both on the electrodes and on the electrolyte at different stages of the experiment, in order to monitor the surface chemical composition. For the surveys, no fitting was performed but the peaks were identified using the handbook by Moulder et al. [102].

5.3.2.2 BE peak shifts under applied potential

The BE shifts of the main peaks (all those marked as 1 in Table 5.1) of the different elements were evaluated as a function of the applied potential difference and the distance of the investigated points from the center of the electrolyte The BE shifts in the elements constituting the electrodes represent changes in the electromotive potential across the sample, while the shifts in the electrolyte represent the Galvani potential shifts, if the chemical potential of the electrons in the electrolyte can be considered constant [116].

The results are shown in Figure 5.7. As can be seen, in all the cases the measured potential difference, in terms of BE shift, was less than half of the applied DC potential, and varied between the investigated elements. Furthermore, while in the electrode components the shift was mostly localized between the two analyzed points closest to the electrolyte stripe, the shift in the GDC appeared to be more gradual, being distributed over the whole observable length of the electrode. The maximum potential differences were deducted from the graphs plotted in Figure 5.7 and reported in Table 5.2. The La 4d shift will be used from now on to indicate the actual potential difference and will be referred to as V_{BE}.

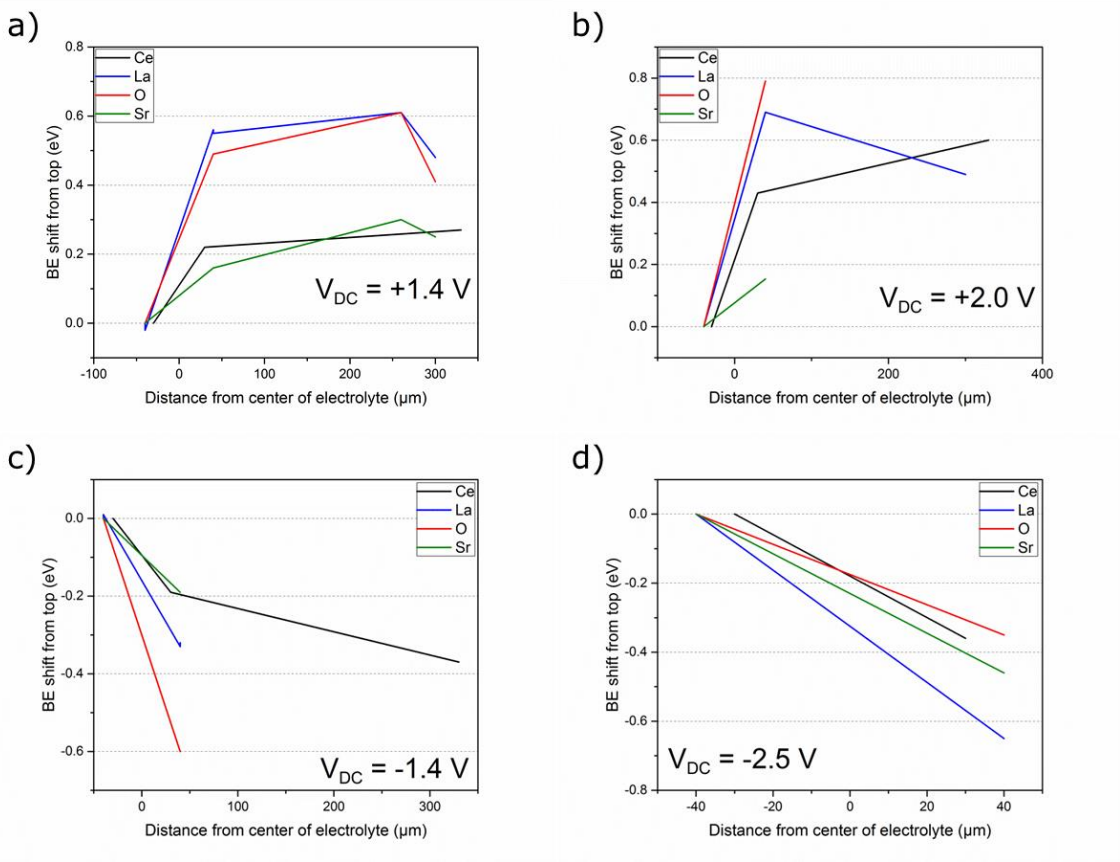

Figure 5.7. Peak shifts of the main elements as a function of distance from the center of the electrolyte stripe at different polarizations

Table 5.2. Summary of applied cell voltages and corresponding potential differences deduced from the BE shifts of the investigated materials.

Applied potential (V_{DC})	Measured potential (V_{BE})			
	La	Sr	O	Ce
+1.4 V	+0.61 V	+0.31 V	+0.61 V	+0.27 V
+2 V	+0.69	+0.15 V	+0.79 V	+0.6 V
-1.4 V	-0.33 V	-0.19 V	-0.6 V	-0.37 V
-2.5 V	-0.65 V	-0.46 V	-0.35 V	-0.36 V (interface)

5.3.2.3 Spectromicroscopy – spatially resolved chemical characterization and peak shift measurements

Element maps were also acquired for La, Sr, Ce and O, both in the area containing the electrolyte stripe and the interfaces with the two electrodes and further away from the electrolyte stripe in the bottom electrode. The purpose of these maps was to observe changes in the surface chemistry of the sample, if present, while also enabling obtaining a spatially resolved mapping of the peak positions for the different elements, which again could be used to map more accurately the distribution of the electromotive potential in the electrodes and the Galvani potential in the electrolyte.

Given the lower signal-to-noise ratio of the spectra in this case, however, the fitted peak positions are prone to a larger uncertainty. In order to perform the fitting, an automated procedure was developed in the Igor software, which extracted the photoelectron spectrum from each acquisition point and fitted it with a Gaussian peak for simplicity. The peak position was then plotted using color maps. Using a Gaussian peak instead of the conventional GL30 peak introduces an error in the fitting, and so does using a single peak where multiple peaks were convoluted, but given the high number of points and the low signal-to-noise ratio this simplifying compromise was considered acceptable.

Finally, since the fitting procedure was automatized, it was performed on the whole investigated area. For this reason, the color plots presented in the following sections were masked off on the areas where the signal was not relevant, in order to facilitate the interpretation of the images.

As can be seen from Figure 5.8, Figure 5.10 and Figure 5.12 the peak positions of all elements in the two electrodes with all examined applied potential differences showed uniform values, as was expected also from the more accurate peak positions shown in Figure 5.7. This was also confirmed by probing the Sr peak deeper into the bottom electrode, as seen in Figure 5.10c.

Similarly, the trends observed in the Ce maps and in the electrolyte areas of the O maps were also consistent with the results presented in Figure 5.7, exhibiting a gradual change when moving down along the bottom electrode.

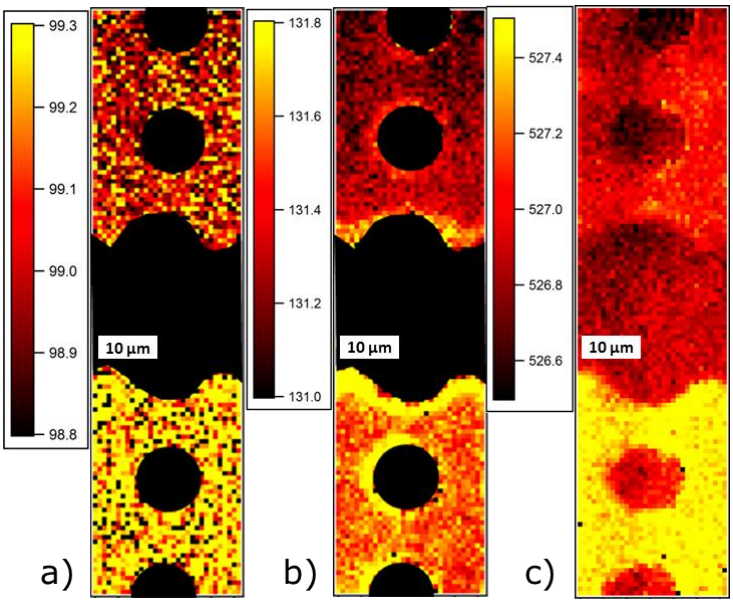

Figure 5.8. a) La, b) Sr and c) O peak positions with V_{BE} = +0.61 V.

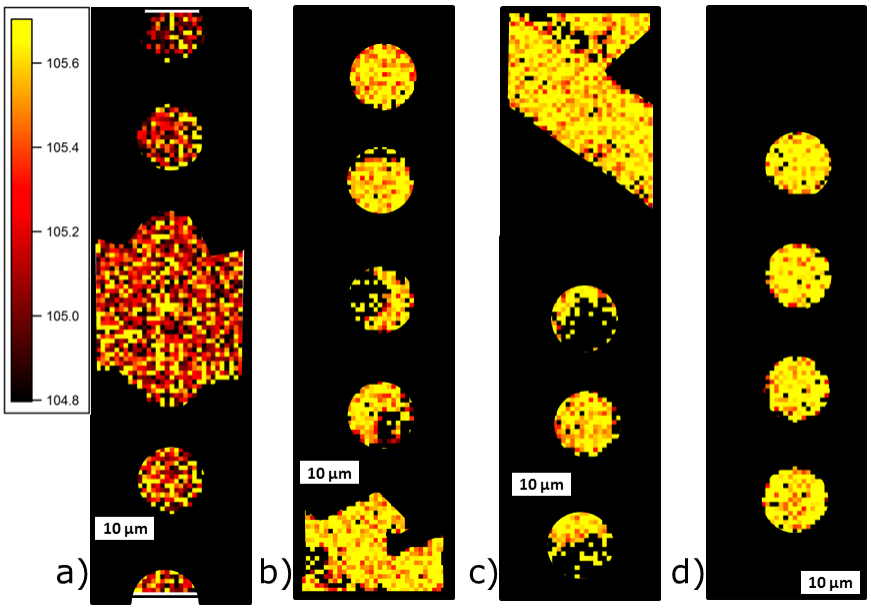

Figure 5.9. Ce peak position with V_{BE} = +0.61 V. The vertical distance between the centers of each of the images is 100 µm.

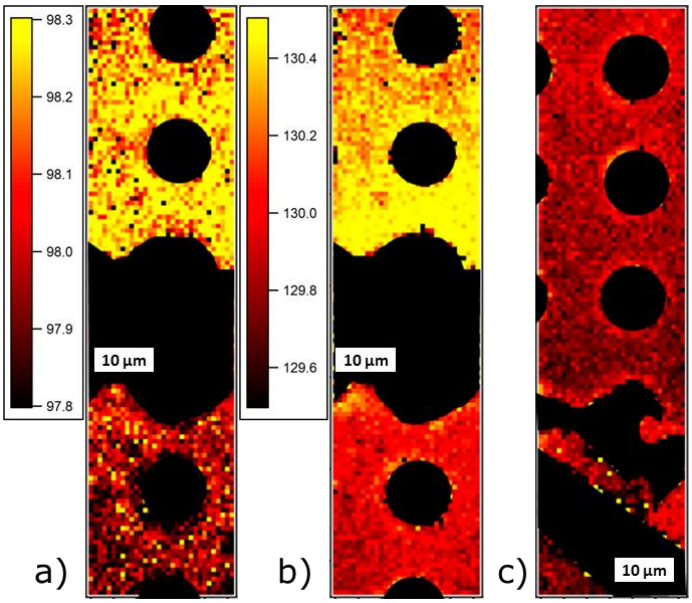

Figure 5.10. a) La, b) and c) Sr peak positions with V_{BE} = -0.65 V. The vertical distance between image b and c is 100 µm.

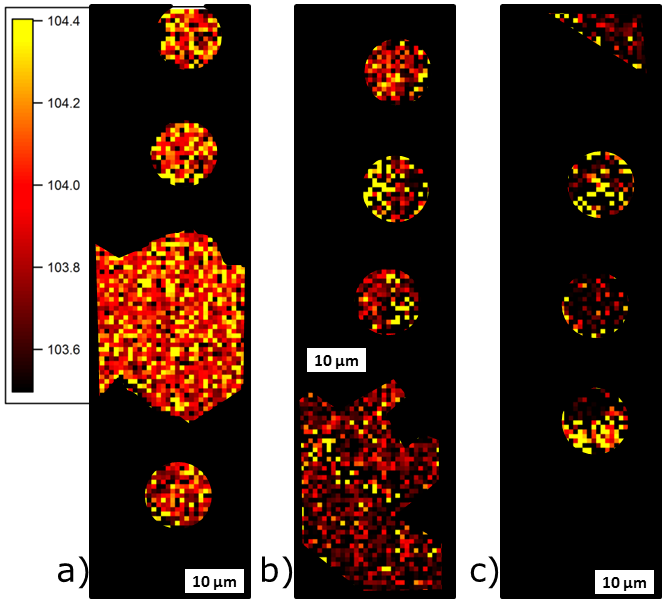

Figure 5.11. Ce peak position with V_{BE} = -0.65 V. The vertical distance between the centers of each of the images is 100 µm.

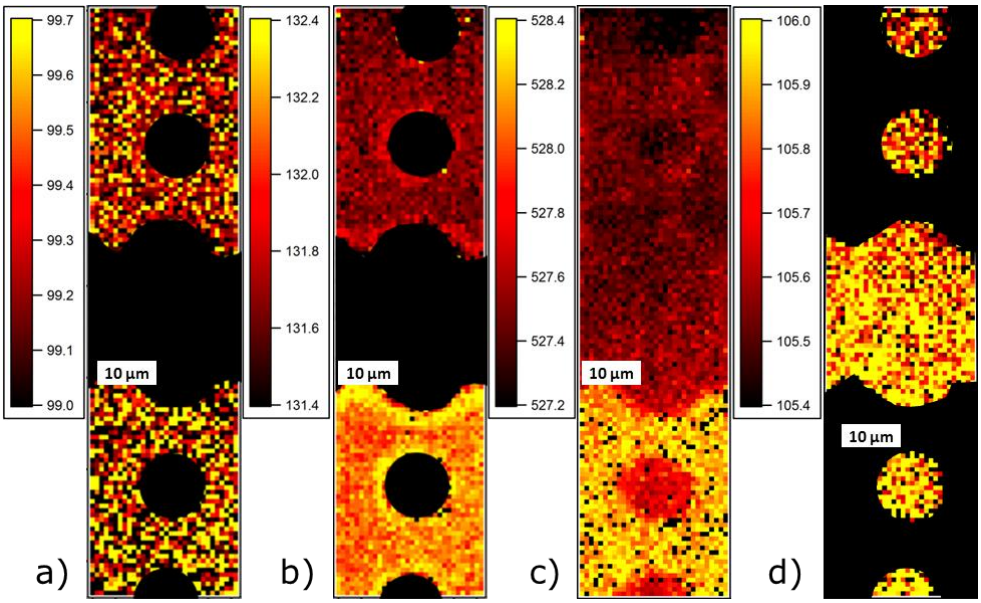

Figure 5.12. a) La, b) Sr, c) O and d) Ce peak positions with V_{BE} = +0.69 V.

5.3.2.4 Peak position plots extracted from the element maps

Average spectra were extracted from approximately 5x5 µm^2 wide regions of the element maps, in order to obtain more finely distributed peak shift measurements than the ones presented in Figure 5.7. The results are shown in Figure 5.13. As can be seen, the values are very scattered and do not reach the same values as the ones measured from the spectra, but they exhibit the already mentioned trends in the electrode materials and in the electrolyte. In particular, Figure 5.13a was obtained by extracting spectra from the maps shown in Figure 5.8 and Figure 5.9, Figure 5.13b was obtained from the maps shown in Figure 5.10 and Figure 5.11, and Figure 5.13c was obtained from the maps shown in Figure 5.12.

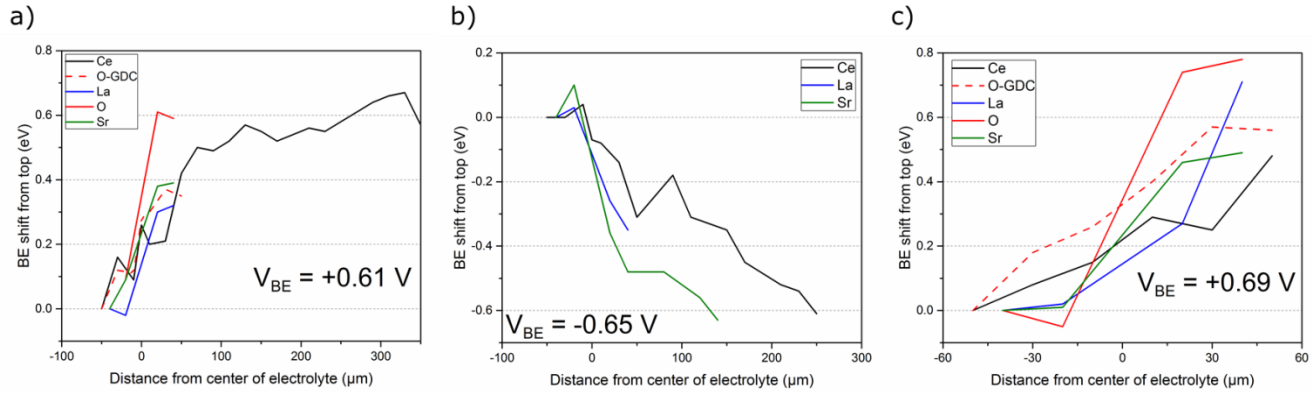

Figure 5.13. peak shifts from the top position extracted from the element maps with V_{BE} values of a) +0.61 V, b) -0.65 V and c)+0.69 V.

5.3.2.5 Simulation of overpotential distribution and comparison with obtained results

A simplified model was realized in COMSOL Multiphysics® v. 5.3 [117], in order to simulate the potential distributions in the electrodes and in the electrolyte. The model consisted of two electrodes, of which one was perfectly grounded and the other was subject to the applied potential, connected by a thin electrolyte layer. The thicknesses of the electrodes and the electrolyte and the separation between the electrodes were chosen according to the real dimensions of the sample. In order to simulate the mixed conducting nature of the electrode, it was modeled as a porous medium with its own electronic and ionic conductivity, while the electrolyte only possessed ionic conductivity. The reaction on the porous electrode was modeled using the linearized Butler-Volmer kinetics. The properties of the materials were chosen accordingly to literature sources and measured values for the relevant temperature, both for LSCF and GDC. In particular, the electrical conductivity of LSCF was set to 300 S/cm [19], its ionic conductivity to 0.01 S/cm [23] and the R_{surf} to 100 Ωcm^2, as determined by chapters 3 and 4. The ionic conductivity of GDC was set to 0.02 S/cm, representing the highest value measured from EIS during the experiment.

As an example, the electrolyte and electrode potential distributions obtained with an applied potential of +0.61 V are shown in Figure 5.14. As can be seen, the electrolyte potential drop can be observed in the electrode region, as observed in the experiments, while the electrode potential does not change significantly over the whole simulated length.

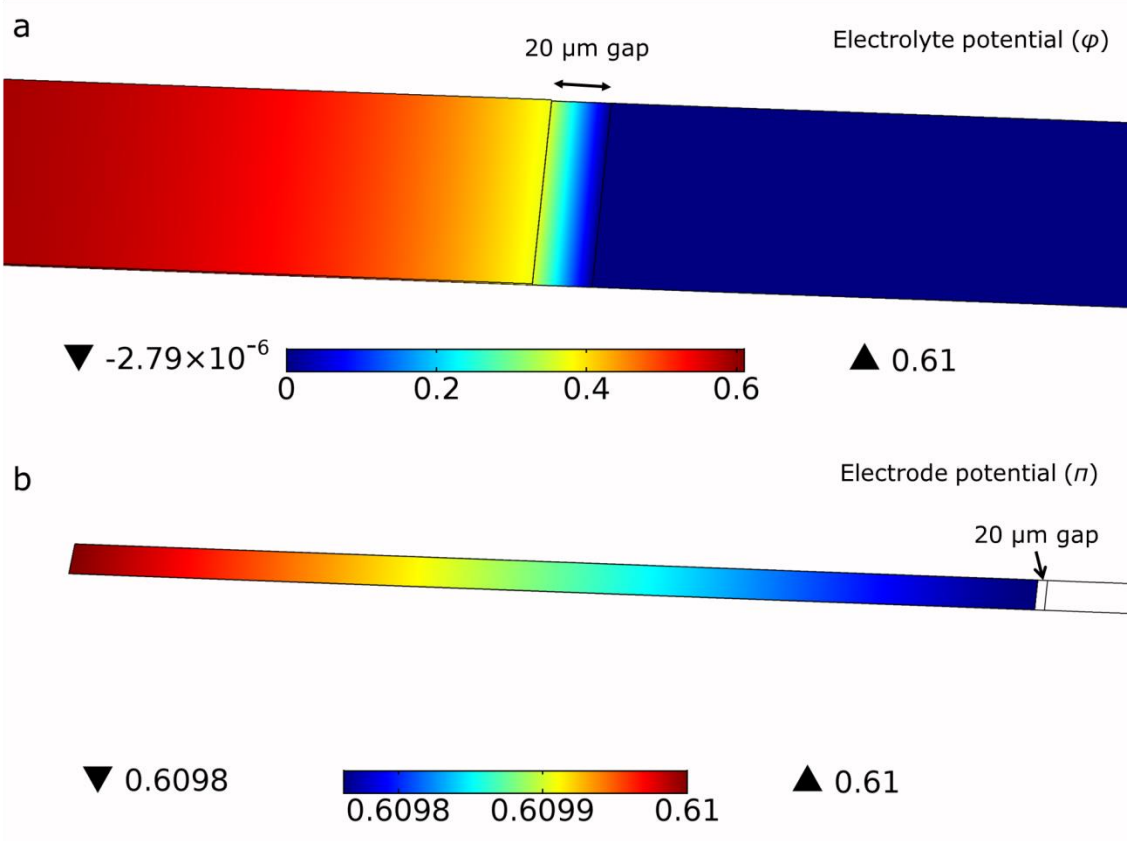

Figure 5.14. a) Electrolyte potential and b) electrode potential distributions simulated with the COMSOL model.

These results, even though obtained on a simplified model, were in line with the experimental results. The plots obtained from the Ce maps were used to obtain overpotential profiles, which were then compared with the overpotential profiles derived from the model. In order to do so, two simplifying assumptions needed to be made: first, the value of π was assumed to be equal to V_{BE}, and second, the BE peak shift for Ce was assumed to correspond to the distribution of φ, which was set to be equal to π at the lowest point observable in the NAP-cell ($\eta_{\sim 300\mu m}$=0). The results can be seen in Figure 5.15. Inside the electrode, the value of π-φ corresponds to the overpotential, while in the electrolyte stripe the change in φ is due to the ohmic drop. As can be seen, the experimental values showed comparable trends to the results of the simulation, despite deriving from a more complex system than the simulated one.

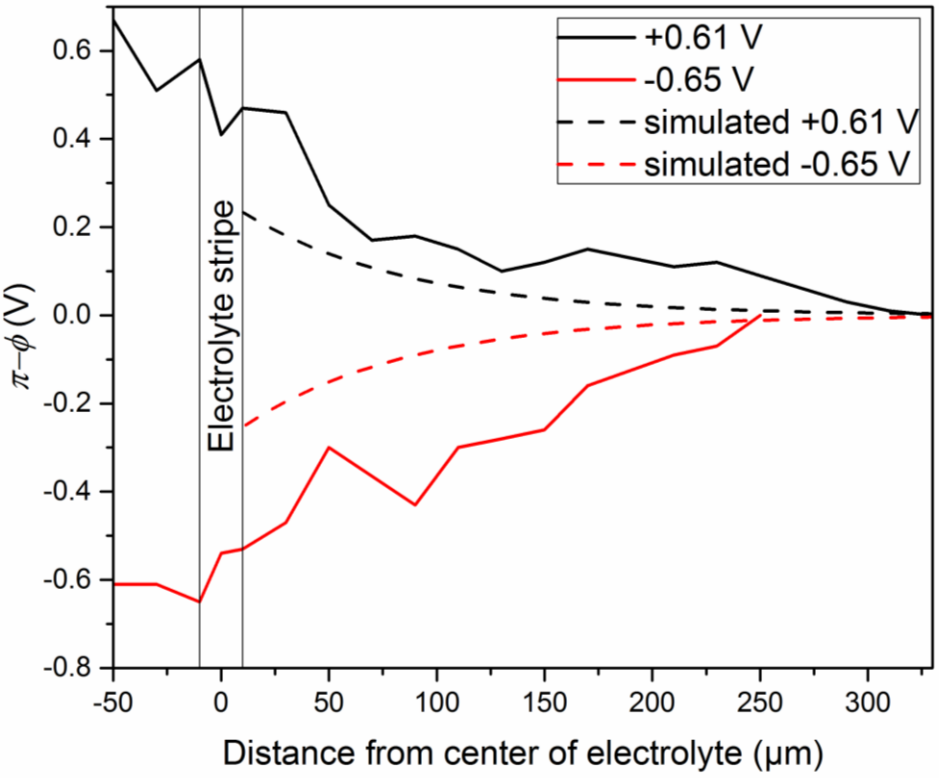

Figure 5.15. Values of π-φ as a function of the distance from the electrolyte stripe, compared with the simulated values for the overpotential distribution.

5.3.2.6 Surface chemical characterization

The element maps could also be used to map the surface chemistry as a function of applied potential difference. However, no difference between the electrodes could be observed in any condition, as can be seen for the case of La (Figure 5.16a) and Sr (Figure 5.16b) in the conditions investigated in this study, excluding therefore surface modifications of the electrodes in the investigated potential range.

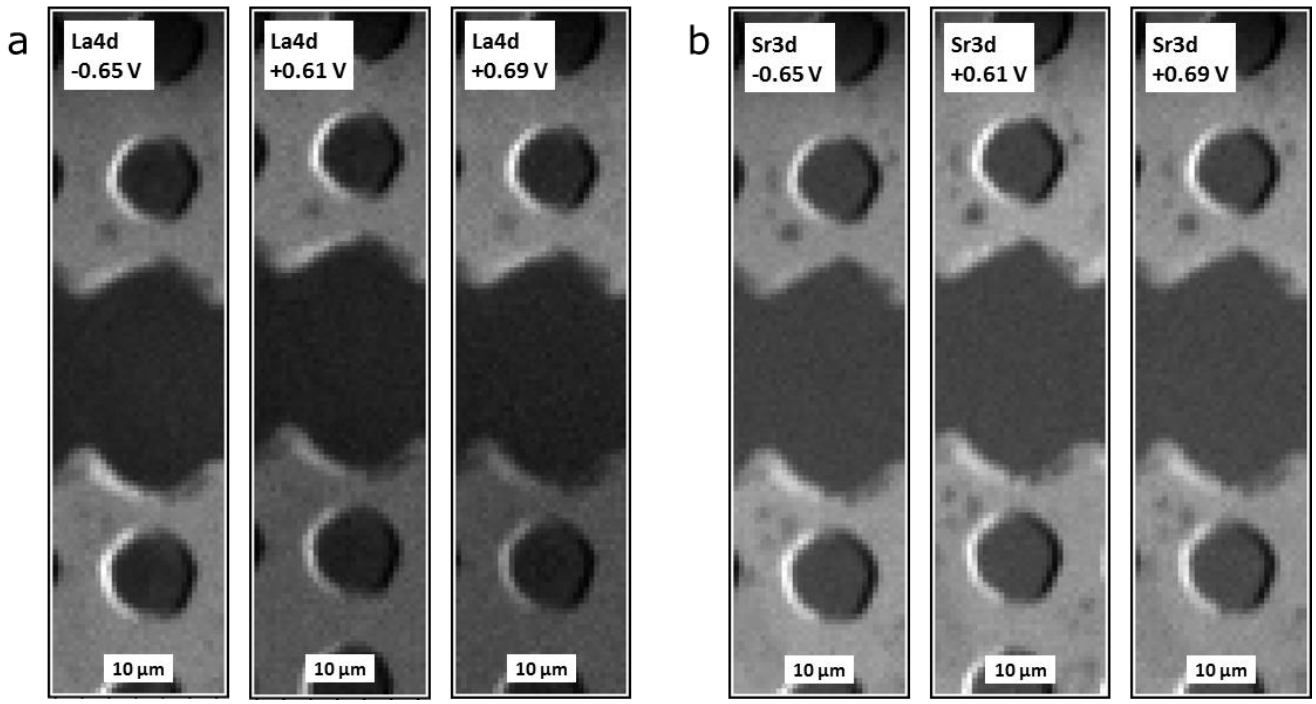

Figure 5.16. a) La maps and b) Sr maps at different applied potential differences.

5.3.2.7 Discussion

The analysis of the BE peak position of the elements constituting the electrodes and the electrolyte, performed both by acquiring point spectra and by fitting the element maps acquired with SPEM, allowed mapping the electric potential distributions in both materials under various applied potentials. In all cases, the LSCF electrodes exhibited an abrupt potential difference at the two edges of the electrolyte stripe that separated them, and uniform potentials along the electrode surfaces. The observed potential differences were less than half the applied values, but represented an accurate reading of the real potentials, and could therefore be compared with the distributions in the electrolyte, in order to deduce the overpotential distributions.

The electric potential in the GDC electrolyte showed a more gradual shift extending in the region under the electrodes in the whole observable region, and reached values close to the ones in the electrodes when moving further away from the central electrolyte stripe. This behavior, which was expected also in light of finite element modelling simulations on a simplified version of the observed sample, resulted in a spatial overpotential distribution between the electrodes and the electrolyte, which could be studied in order to identify overpotential-dependent surface modifications of both materials, if present. However, no compositional differences could be observed in any of the experimental conditions. Longer experiment times or higher temperatures might be needed in order to stimulate observable surface modifications.

The difference between the applied potentials and the measured values could not be explained, but could likely be attributed to non-linear voltage drops caused by contact resistances, that could be concealed in the HF EIS arc attributed to the GDC due to its low capacitance (~10^{-10} F). Indeed, when comparing the Ohmic drops measured across the electrolyte stripe using the spectra with the expected values calculated taking into

account the current flowing through the cell and the resistance measured by EIS, a difference of 2-5 times between the two values was observed, as can be seen from the following Table 5.3 for the four investigated potential values.

Table 5.3. Comparison between expected and measured values of IR drop over the electrolyte, together with the applied and measured potentials.

Applied potential	Measured potential	Expected IR drop	Measured IR drop
+1.4 V	+0.61 V	+0.4 - +0.7 V	+0.22 V
+2 V	+0.69	+1.6 V	+0.43 V
-1.4 V	-0.33 V	-0.55 - -0.8 V	-0.19 V
-2.5 V	-0.65 V	-1.6 - -1.8 V	-0.37 V

5.4 Conclusions

Electrochemical measurements were successfully performed on model thin film LSCF/GDC composite electrodes in a NAP-SPEM setup. This allowed the contemporary observation of the surface chemistry and the electric potential distributions in both materials under applied potential differences, allowing establishing experimentally determined overpotential distributions that followed the trends expected from finite element modelling simulations.

The results confirmed the presence of a wide electroactive area extending under the electrode material, which increased with increasing applied potential, while no changes in the electrode chemistry could be observed in any of the testing conditions.

6 Towards *in operando* characterization of SOC devices using KPFM

6.1 Introduction

The electrodes of SOCs possess complex composite and/or porous microstructures, resulting in spatial chemical and morphological inhomogeneities that influence the electrodes' performance and active regions. Common analysis techniques used in the characterization of SOCs, such as EIS, IV-curves or CV, despite often being combined with post-mortem SEM characterization, are unable to investigate and monitor the evolution of the microstructure, chemistry and active regions of such electrodes during operation [28].

One possible solution, which is capable of unifying electrochemical characterization of SOC materials in realistic operating conditions with spatially resolved surface mapping of topography and electrical properties, is represented by the controlled atmosphere high temperature scanning probe microscope (CAHT-SPM), developed by Danish Micro Engineering (DME – now Semilab) for DTU Energy, described in chapter 2.7 [39]. In particular, this study focuses on exploring the capabilities of KPFM in relevant temperature and atmosphere ranges for SOC materials. KPFM is a technique widely used in the characterization of semiconducting devices [34,118–122] and in corrosion science [123], typically at room temperature, but high-temperature KPFM has also been attempted on SOC materials [124].

Given the complex nature of the signal acquired by KPFM, which contains chemical information, in terms of work function (Φ) of the materials, as well as electrical information, in terms of rigid shifts of the Fermi level due to the local electrochemical potential imposed on the sample [125,126], standard calibration samples of gradually increasing complexity need to be developed before attempting *in situ* studies of realistic SOC electrodes. This work represents a first attempt in this direction, by producing a capacitor-like sample with materials capable of operating at high temperature. The simple design should allow the separation of chemical and electrical contributions while establishing the lateral spatial and energetic resolution of KPFM under realistic SOC operating conditions.

6.2 Experimental

6.2.1 Sample preparation

In order to produce a high-temperature capacitor test sample, a 120-140 nm $LaNi_{0.6}Fe_{0.4}O_3$ (LNF) thin film was deposited by PLD on (100)-oriented MgO substrates. LNF was chosen for being a good EC, with reported conductivities of 300-600 S/cm with weak temperature dependence in the 600-900 °C range [127,128], while MgO is a common choice as an insulating substrate for perovskite thin film studies [54,129,130]. The depositions were performed at 600 °C in 0.1 mbar O_2 with a laser fluency of 3-4 J/cm^2 and a substrate-target distance of 60-70 mm.

After the PLD process, the sample was spin-coated with positive photoresist (S1818, MicroResist Technology GmbH) and thereafter exposed to UV light through a photomask with a 10-µm line, aligned with the center of the sample, using a Karl Suss MJB-3 mask-aligner.

After the development of the photoresist by dipping the exposed sample in the appropriate developer (MF 319, MicroResist Technology GmbH), the LNF was removed from the so-obtained line using Ar-ion etching (Oxford Instruments Ionfab 300). The samples were periodically inspected using an optical microscope to determine when the LNF layer had been fully removed.

Finally, in order to obtain a good electrical contact to the LNF electrodes, Au paste (DuPont) was applied near the outer edges of the electrodes and calcined at 600 °C for 1 h before the experiment.

6.2.2 CAHT-KPFM

The sample was placed onto the heating element of the CAHT-SPM, and electrical contact to the electrodes was realized by pressing two Pt wires onto the gold pads using the spring-loaded Al2O3 pins designed to hold the sample in place. The experiment was performed at 400 °C and 600 °C, both in N_2 flow and in O_2 flow.

The connection scheme is shown in Figure 6.1. Using an externally connected potentiostat (Gamry FAS2 Femtostat), the potential difference between the electrodes could be controlled and was set to either 0 (OCV), ±200 mV or ±400 mV, while measuring the leak current flowing through the sample.

The ground lead of the potentiostat was also connected to the ground lead of the KPFM Digital Programmable Waveform Analyzer (DiProWa - DME), in order to avoid cross-talk between the two instruments during the experiment. The SPM probe was connected to the other end of the DiProWa, where the DC potential compensating the CPD was applied.

The probes used for the topography and surface potential measurements were Aspire CFM probes, with a resonance frequency of 75 kHz, consisting of n-doped Si.

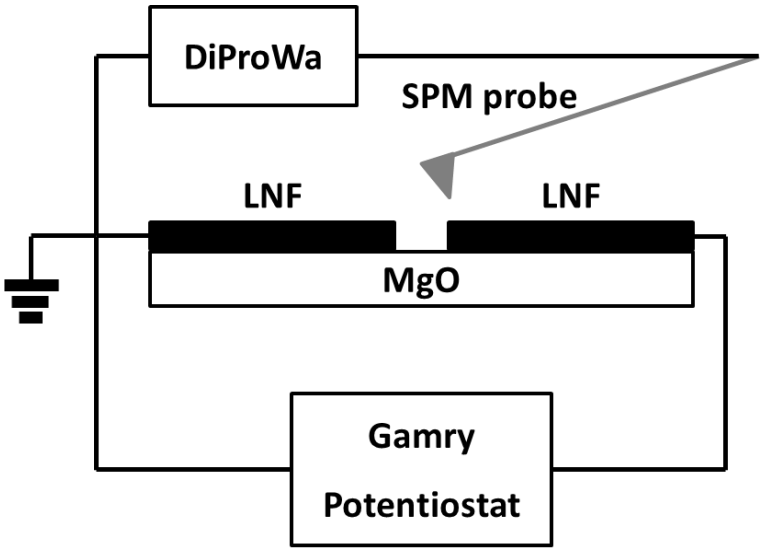

Figure 6.1. Connection scheme for the performed KPFM measurements.

6.3 Results and discussion

6.3.1 CAHT-KPFM analysis

Chronoamperometry measurements were performed at both examined temperatures and in the two different atmospheres, showing currents in the 10^{-13}-10^{-10} A range under polarization of up to 400 mV, thereby confirming the insulating nature of the substrate.

Figure 6.2 shows images of the topography of the sample (a), where the two electrodes are visible, as well as KPFM measurements performed at OCV and under ±200 mV and ±400 mV applied potential difference (b-f) at 600 °C in N_2 flow. Profiles of the topography and the potential distributions were extracted and plotted against the position on the sample in Figure 6.3a. The OCV potential profile was subtracted from the profiles under applied polarization, resulting in the plots in Figure 6.3b. As can be seen, the potential difference between the electrodes showed values smaller than the applied potential difference both before and after subtracting the OCV potential profile, settling at 100-150 mV when the applied potential difference was 200 mV, and at 200-250 mV when the applied potential difference was 400 mV.

Similarly, the topography and potential images acquired at 400 °C in O_2 flow are shown in Figure 6.4a-d, with the extracted profiles in Figure 6.5a. Again, the OCV potential distribution was subtracted from the profiles under polarization, obtaining the plots in Figure 6.5b. When a potential difference of 200 mV was applied to the sample, the initial profiles in the two directions appeared different. However, when subtracting the OCV potential distribution, which was asymmetric across the sample, the two profiles appeared similar, reaching values close to the applied potential difference.

Measurements at 600 °C in O_2 flow were also attempted, proving more difficult due to instabilities during the scans, but nevertheless KPFM was successfully performed under polarization, resulting in the distribution shown in Figure 6.6 b and c. The OCV potential distribution was asymmetric, as can be seen in

Figure 6.7a, and showed an increase at the edge between the MgO stripe and the electrode with applied potential. This increase could also be seen when applying a potential difference between the electrodes. The observable potential difference between the electrodes, once corrected for the OCV value settled at 150 mV with an applied potential difference of 400 mV, as seen in Figure 6.7b.

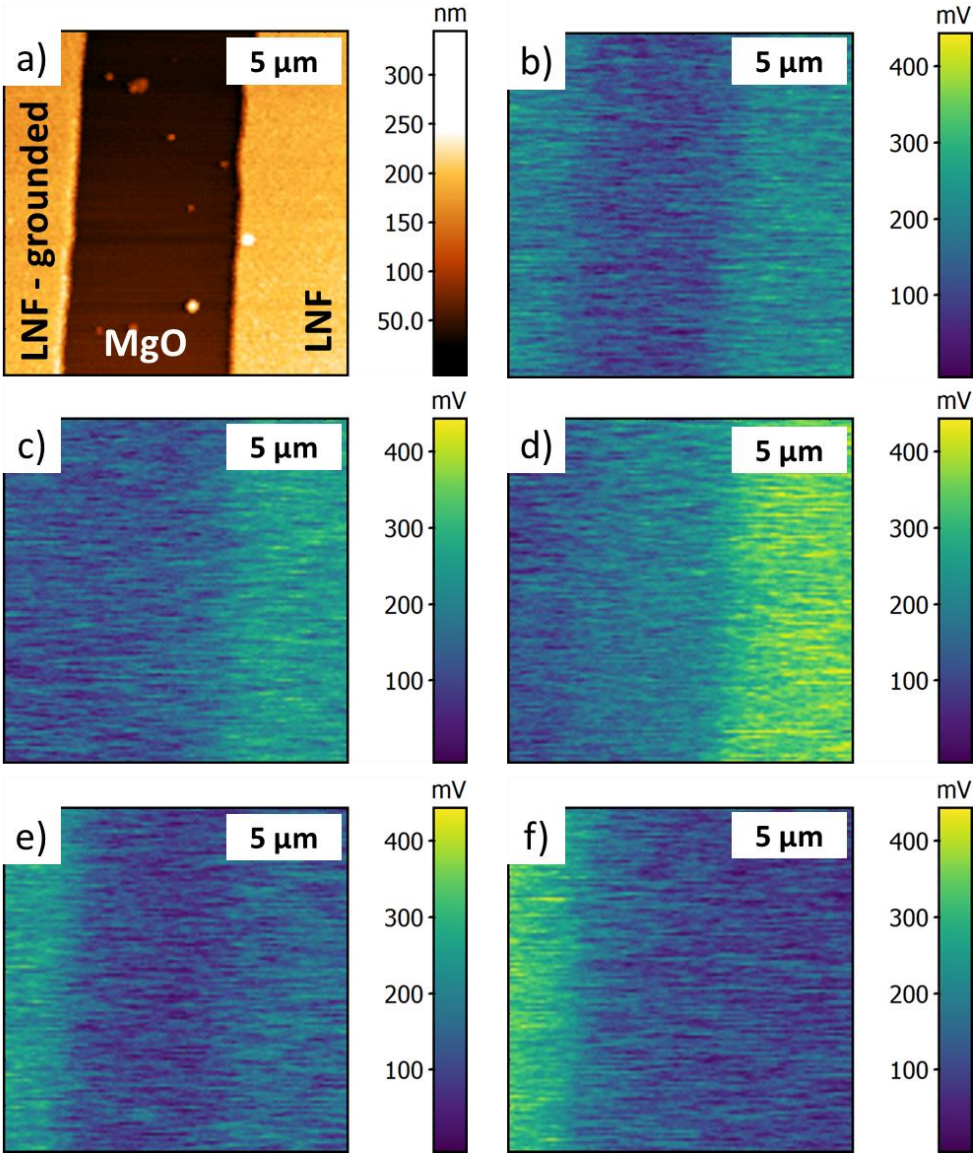

Figure 6.2. Images acquired at 600 °C in flowing N_2 of a) topography and potential distribution at b) OCV, c) +200 mV, d) +400 mV, e) -200 mV, f) -400 mV.

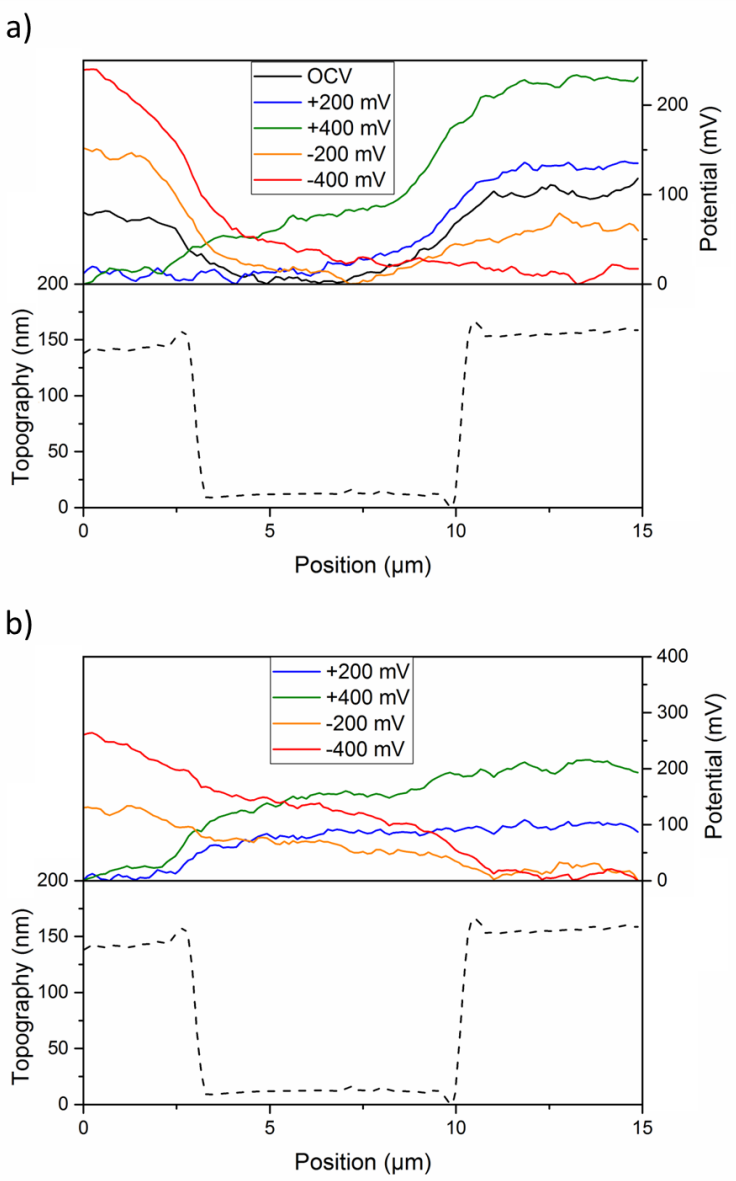

Figure 6.3. Profiles extracted from the central region of Figure 6.2b-f. The OCV potential distribution showed in a was subtracted from the other distributions to obtain the plots in b.

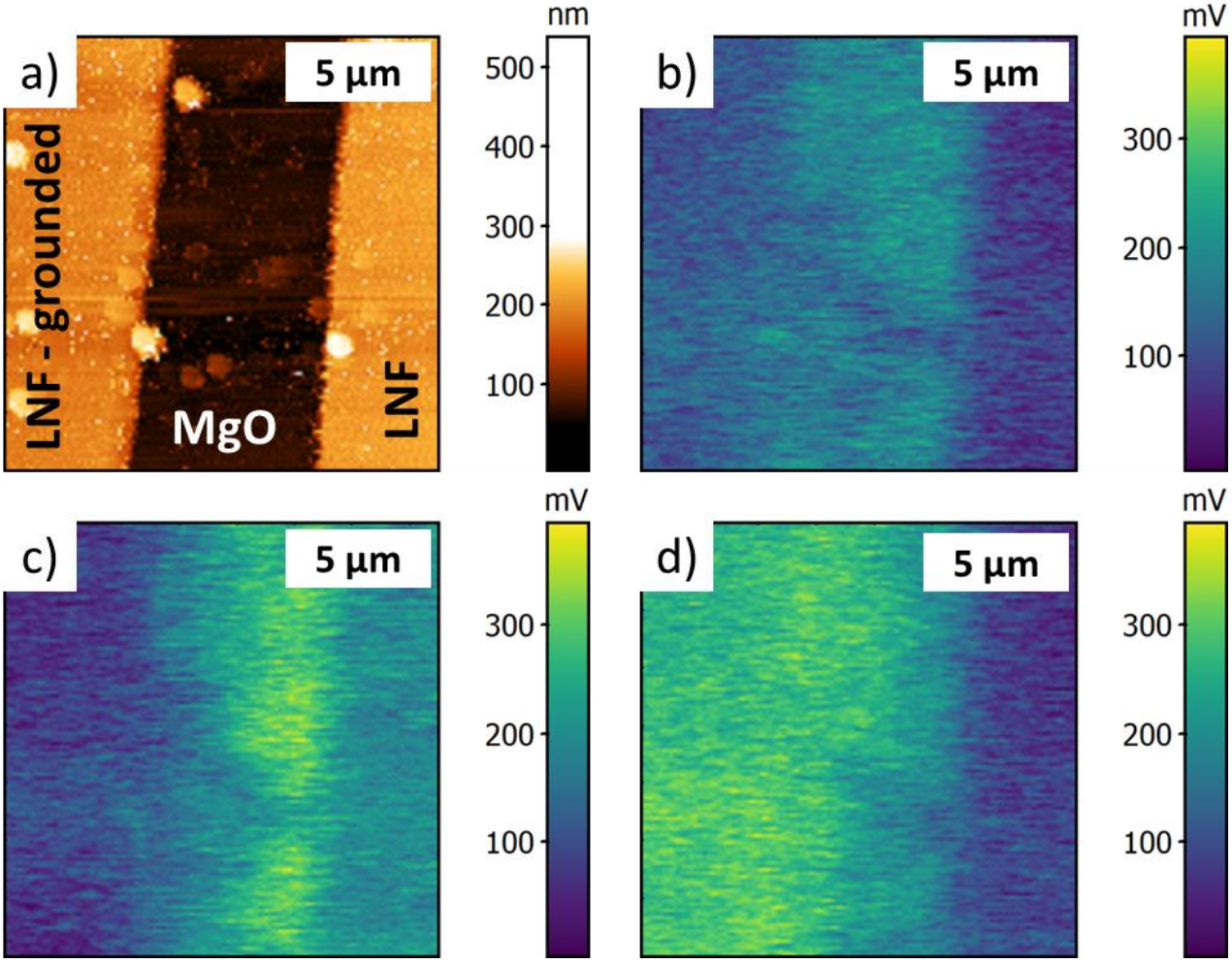

Figure 6.4. Images of a) topography and potential distribution at b) OCV, c) +200 mV, d) -200 mV.

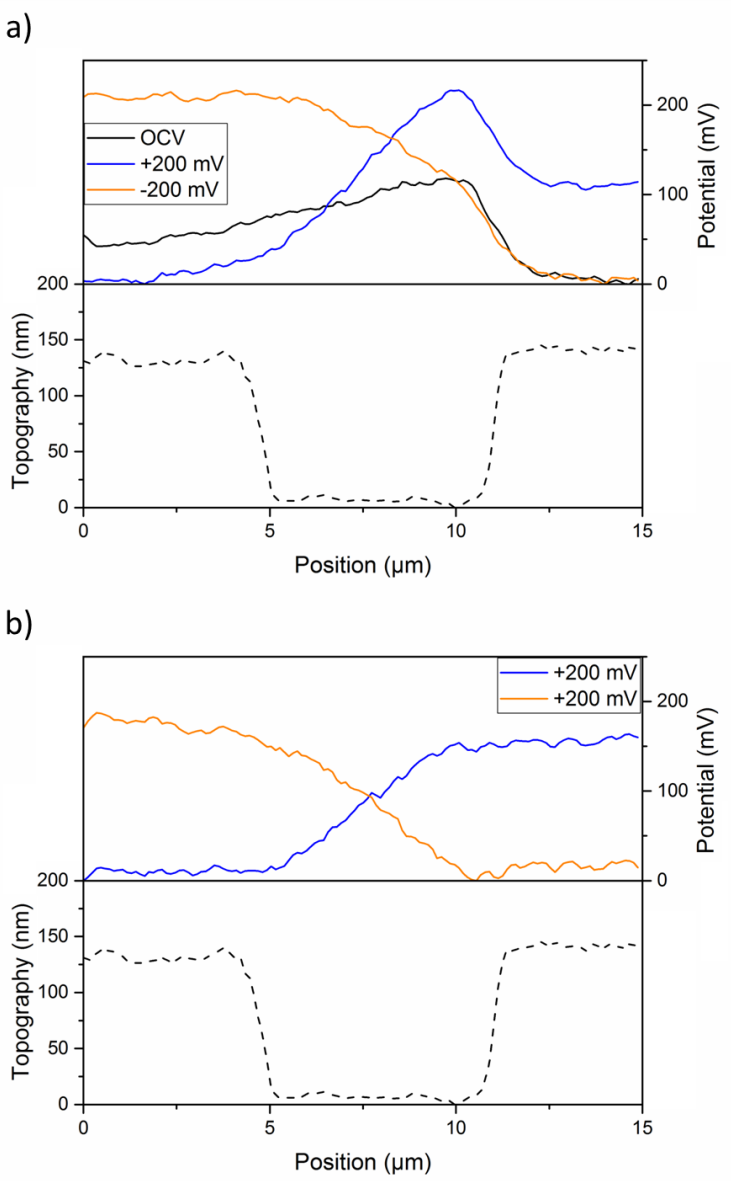

Figure 6.5. Profiles extracted from the central region of Figure 6.4b-d. The OCV potential distribution showed in a was subtracted from the other distributions to obtain the plots in b.

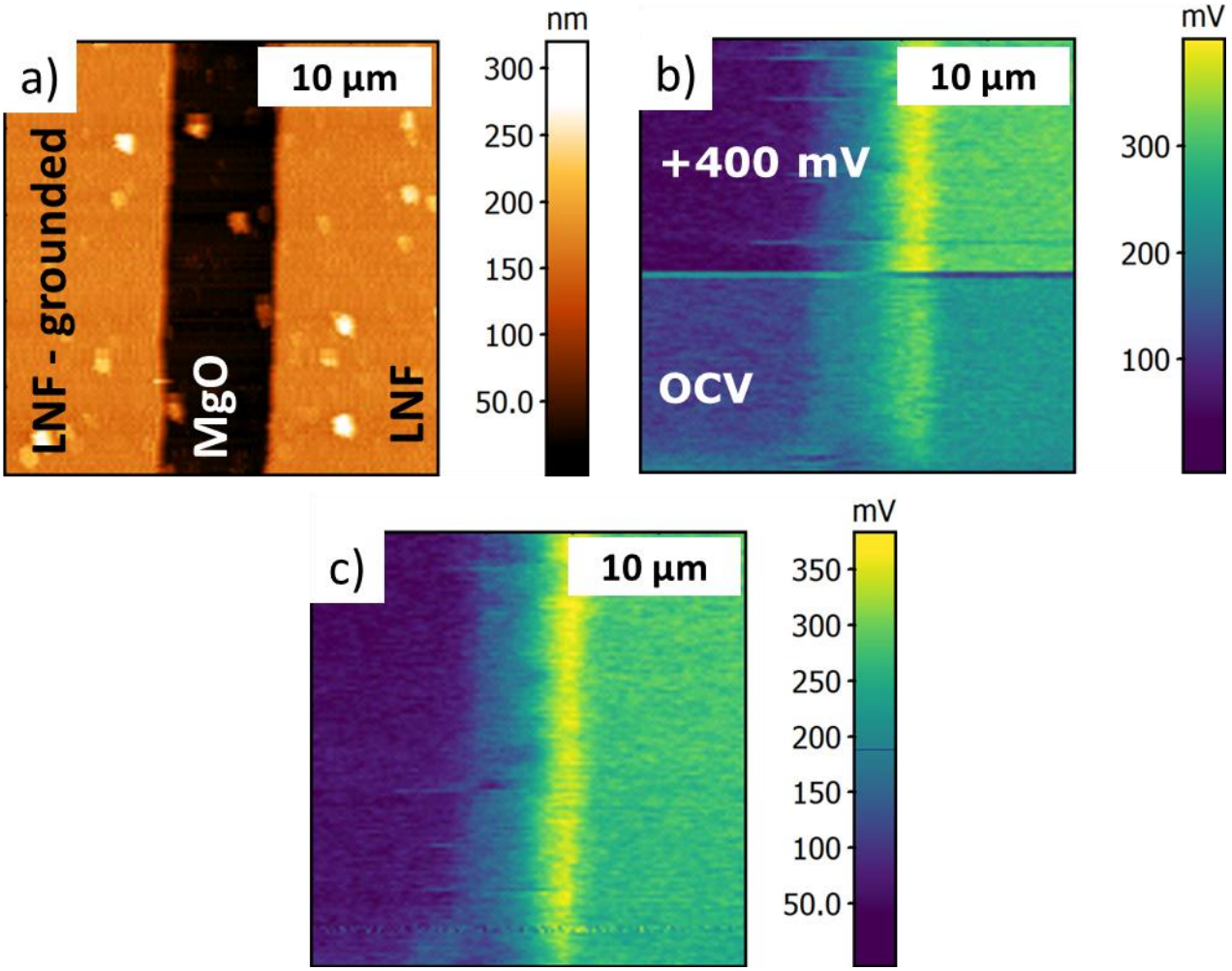

Figure 6.6. Images of a) topography, b) potential distribution at OCV in the bottom part of the image and +400 mV in the top part and c) potential distribution at +400 mV.

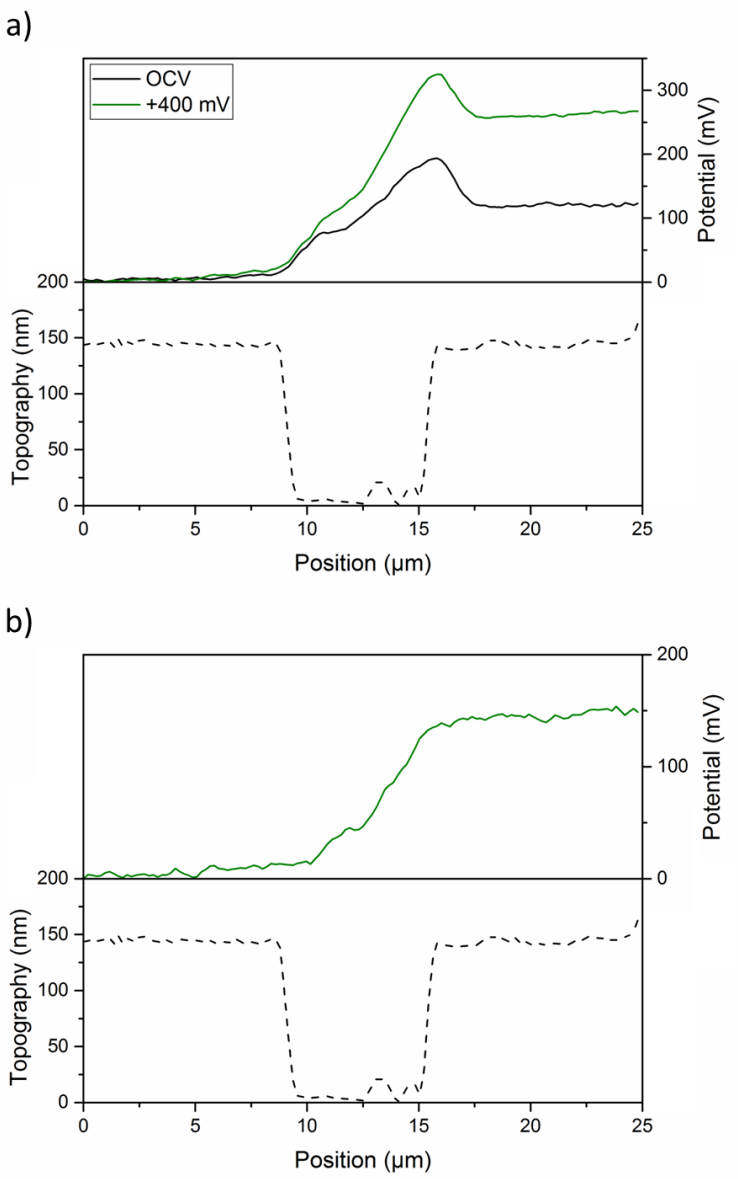

Figure 6.7. Profiles extracted from the two regions in Figure 6.6b. The OCV distribution shown in a was subtracted from the one with applied potential to obtain the plot in b.

6.4 Discussion

Since KPFM is a technique sensitive both to different chemistries and to electric potential distributions, separating the two contributions is not straightforward. The measured potential difference (V_{DC}), in fact, is a sum of the CPD, which corresponds to the difference between the work functions of the tip and the sample (Φ_T and Φ_S), and the potential difference applied to the sample (V_{appl}), as shown in the following Figure 6.8.

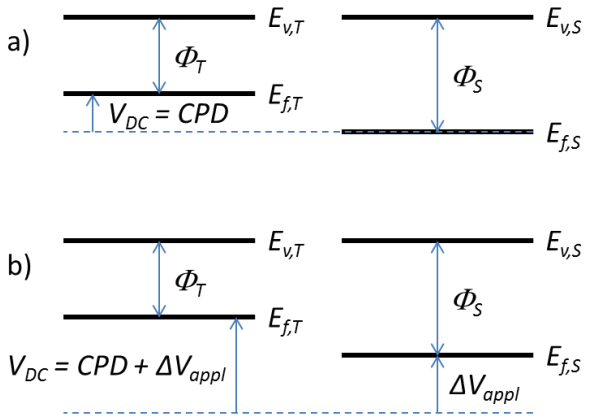

Figure 6.8. Diagram of the energy levels of the tip and the sample, a) without and b) with applied polarization to the sample.

The only possibility to distinguish between the effect of chemistry and potential using only the KPFM measurements is to subtract the surface potential distributions measured at OCV from the ones with applied polarization. The results of this procedure are shown for the potential maps acquired at 400 °C in O_2 flow, resulting in Figure 6.9a for the case with +200 mV applied potential difference and Figure 6.9b for the case with -200 mV applied potential difference.

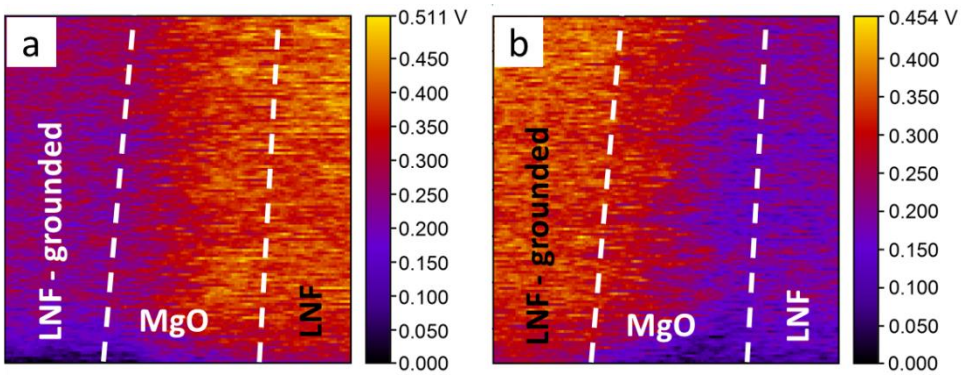

Figure 6.9. OCV-corrected potential distributions at 400 °C in O_2 flow, obtained by subtracting Figure 6.4b from a) Figure 6.4c and b) Figure 6.4d.

The plots in Figure 6.3b, Figure 6.5b and Figure 6.7b were obtained by applying a similar procedure to the potential profiles instead of the entire images.

The measured potential difference between the electrodes was smaller (in magnitude) than the applied values in most of the cases. This could be caused either by contact losses between the Pt wires and the LNF electrodes or by chemical changes on the surface of the electrodes under polarization, which would affect Φ_S.

Regarding the chemistry of the sample, an interesting behavior can be observed when comparing Figure 6.2b and Figure 6.4b. The chemical contrast in absence of polarization shows in fact two opposite

behaviors in the two examined atmospheres. In N_2, the CPD decreased over the central MgO stripe, while in O_2 it increased with respect to the LNF electrodes. This can also be deducted from the potential distribution at OCV at 600 °C in O_2 (Figure 6.6b). These different behaviors can probably be explained by the two different gas atmospheres interacting with the MgO and forming a surface adsorbate layer. The precise determination of the origin of the different behaviors was outside of the scope of this study, but represents another potential application of CAHT-KPFM for future works.

6.5 Conclusions

KPFM has successfully been performed in N_2 and O_2 containing atmospheres at temperatures up to 600 °C, proving its relevance for *in situ* studies of SOC materials. Topography scans at high temperature exhibit sub-µm resolution, and the different materials constituting the sample can be distinguished in the surface potential maps. Furthermore, surface potential changes between the electrodes consistent with the externally applied electric potentials can be observed, despite not always reaching the expected values.

In particular, commercial probes proved to be adequate for high temperature measurements, even in strongly oxidizing conditions. Further testing with other commercial probes or modified ones will be performed in order to find the most suitable candidates, but the obtained results are already very promising.

Future developments of the technique will include the characterization of model SCs with relevant materials for the investigation of SOC reactions, as well as the investigation of the surface potential variations with known applied overpotential on specifically designed samples, with the final goal of investigating realistic SOC electrodes in operando.

7 Outlook

The oxygen reactions occurring on SOC electrodes were studied with a number of different techniques, to investigate the factors governing the electrode activity and degradation, as well as attempt a deeper study of the reaction mechanisms. Many valuable results were obtained, leading to further questions, which can serve as an inspiration for further work in the analysis of the complex phenomena occurring at the materials' surfaces and interfaces.

The work presented in chapter 3 allowed establishing a set of useful guidelines in order to measure the intrinsic activity of the electrode surfaces with respect to the oxygen reactions on model thin film samples. Further possible studies could include systematic studies over a larger number of samples with different film thicknesses and CC mesh sizes, as well as a controlled poisoning of the surface in order to identify the importance of the elements found in post-mortem analysis on the surface exchange in real time.

The work presented in chapter 4 resulted in the determination of two important parameters for the mechanistic interpretation of the oxygen reactions, namely the correlation between the surface potential of the electrodes and the applied overpotential in the 10^{-2}-1 mbar O_2 range and the most probable reaction pathway for the oxygen incorporation. Further developments would include the determination of the surface potential-overpotential relation until ambient pressure, as well as the investigation of the causes of the surface potential changes with applied overpotential. Furthermore, the interpretation of the RDS for the oxygen incorporation should be integrated with more experimental data.

The work presented in chapter 5 proved the great potential of SPEM in the simultaneous determination of surface chemistry and potential distributions in SOC materials while operating at high temperature and in 10^{-2}-10^{-1} mbar O_2 with externally applied potential differences. Further efforts would be needed to increase the possible operating pressures and reduce the electrical losses in order to control the operating parameters more accurately.

The work presented in chapter 6 proved the capabilities of high temperature KPFM in controlled atmospheres using commercial probes on a model standard sample. Further developments would include the identification of the most suitable probes to obtain the best spatial and signal resolution, and differentiate between high temperature chemistry evolution studies and potential distribution studies. Furthermore, KPFM would represent an ideal candidate to replicate the studies performed in chapters 4 and 5, both at the already examined pO_2 ranges and at real operating pressures, providing the chemical and electrical contributions can be distinguished.

8 Bibliography

[1] D.J.L. Brett, A. Atkinson, N.P. Brandon, S.J. Skinner, Intermediate temperature solid oxide fuel cells, Chem. Soc. Rev. 37 (2008) 1568. doi:10.1039/b612060c.

[2] R.M. Ormerod, Solid oxide fuel cells, Chem. Soc. Rev. 32 (2003) 17–28. doi:10.1039/b105764m.

[3] B.C.H. Steele, A. Heinzel, Materials for fuel-cell technologies, Nature. 414 (2001) 345–352. doi:10.1038/35104620.

[4] K. Kendall, M. Kendall, High-temperature Solid Oxide Fuel Cells for the 21st Century: Fundamentals, Design and Applications, 2015. https://books.google.co.uk/books?id=INCcBAAAQBAJ.

[5] Y. Wang, T. Liu, L. Lei, F. Chen, High temperature solid oxide H2O/CO2co-electrolysis for syngas production, Fuel Process. Technol. 161 (2017) 248–258. doi:10.1016/j.fuproc.2016.08.009.

[6] S.D. Ebbesen, S.H. Jensen, A. Hauch, M.B. Mogensen, High temperature electrolysis in alkaline cells, solid proton conducting cells, and solid oxide cells, Chem. Rev. 114 (2014) 10697–10734. doi:10.1021/cr5000865.

[7] S.Y. Gómez, D. Hotza, Current developments in reversible solid oxide fuel cells, Renew. Sustain. Energy Rev. 61 (2016) 155–174. doi:10.1016/j.rser.2016.03.005.

[8] J. Larminie, A. Dicks, Fuel Cell Systems Explained, 2001. doi:10.1016/S0378-7753(00)00571-1.

[9] J.T.S. Irvine, D. Neagu, M.C. Verbraeken, C. Chatzichristodoulou, C. Graves, M.B. Mogensen, Evolution of the electrochemical interface in high-temperature fuel cells and electrolysers, Nat. Energy. 1 (2016) 15014. doi:10.1038/nenergy.2015.14.

[10] S.B. Adler, Factors governing oxygen reduction in solid oxide fuel cell cathodes, Chem. Rev. 104 (2004) 4791–4843. doi:Doi 10.1021/Cr020724o.

[11] V. Brichzin, J. Fleig, H.U. Habermeier, G. Cristiani, J. Maier, The geometry dependence of the polarization resistance of Sr-doped $LaMnO_3$ microelectrodes on yttria-stabilized zirconia, Solid State Ionics. 152–153 (2002) 499–507. doi:10.1016/S0167-2738(02)00379-X.

[12] W. Khan, A.H. Naqvi, M. Gupta, S. Husain, R. Kumar, Small polaron hopping conduction mechanism in Fe doped $LaMnO_3$, J. Chem. Phys. 135 (2011) 1–7. doi:10.1063/1.3615720.

[13] J. Richter, P. Holtappels, T. Graule, T. Nakamura, L.J. Gauckler, Materials design for perovskite SOFC cathodes, Monatshefte Fur Chemie. 140 (2009) 985–999. doi:10.1007/s00706-009-0153-3.

[14] T. Noh, J. Kim, Y. Kim, H.O.H. Chun, M. Jeon, Mn valence state and electrode performance of perovskite-type cathode $La_{0.8}Sr_{0.2}Mn_{1-x}Cu_xO_{3-\delta}$ (x=0 , 0.2) for intermediate-temperature solid oxide fuel cells, 36 (2013) 1261–1266.

[15] K. Świerczek, M. Gozu, Structural and electrical properties of selected $La_{1-x}Sr_xCo_{0.2}Fe_{0.8}O_3$ and $La_{0.6}Sr_{0.4}Co_{0.2}Fe_{0.6}Ni_{0.2}O_3$perovskite type oxides, J. Power Sources. 173 (2007) 695–699. doi:10.1016/j.jpowsour.2007.05.052.

[16] M. Mogensen, D. Lybye, N. Bonanos, P. V. Hendriksen, F.W. Poulsen, Factors controlling the oxide ion conductivity of fluorite and perovskite structured oxides, Solid State Ionics. 174 (2004) 279–286. doi:10.1016/j.ssi.2004.07.036.

[17] K. Momma, F. Izumi, *VESTA3* for three-dimensional visualization of crystal, volumetric and morphology data, J. Appl. Crystallogr. 44 (2011) 1272–1276. doi:10.1107/S0021889811038970.

[18] T. Ishihara, Perovskite Oxide for Solid Oxide Fuel Cells, 2009. doi:10.1007/978-0-387-77708-5.

[19] L.W. Tai, M.M. Nasrallah, H.U. Anderson, D.M. Sparlin, S.R. Sehlin, Structure and Electrical-Properties of $La_{1-x}Sr_xCo_{1-y}Fe_yO_3$ .Part 1. The System $La_{0.8}Sr_{0.2}Co_{1-y}Fe_yO_3$, Solid State Ionics. 76 (1995) 259–271.

doi:http://dx.doi.org/10.1016/0167-2738(94)00244-M.
[20] L.W. Tai, M.M. Nasrallah, H.U. Anderson, D.M. Sparlin, S.R. Sehlin, Structure and electrical properties of $La_{1-x}Sr_xCo_{1-y}Fe_yO_3$. Part 2. The system $La_{0.8}Sr_{0.2}Co_{1-y}Fe_yO_3$, Solid State Ionics. 76 (1995) 273–283. doi:10.1016/0167-2738(94)00244-M.
[21] S.I. Hashimoto, Y. Fukuda, M. Kuhn, K. Sato, K. Yashiro, J. Mizusaki, Oxygen nonstoichiometry and thermo-chemical stability of $La_{0.6}Sr_{0.4}Co_{1-y}Fe_yO_{3-\delta}$ (y = 0.2, 0.4, 0.6, 0.8), Solid State Ionics. 181 (2010) 1713–1719. doi:10.1016/j.ssi.2010.09.024.
[22] M. Kuhn, Y. Fukuda, S. Hashimoto, K. Sato, K. Yashiro, J. Mizusaki, Oxygen Nonstoichiometry and Thermo-Chemical Stability of Perovskite-Type $La_{0.6}Sr_{0.4}Co_{1-y}Fe_yO_{3-\delta}$ (y = 0, 0.2, 0.4, 0.5, 0.6, 0.8, 1) Materials, J. Electrochem. Soc. 160 (2012) F34–F42. doi:10.1149/2.050301jes.
[23] Y. Teraoka, H.M. Zhang, K. Okamoto, N. Yamazoe, Mixed ionic-electronic conductivity of $La_{1-x}Sr_xCo_{1-y}Fe_yO_{3-\delta}$ perovskite-type oxides, Mater. Res. Bull. 23 (1988) 51–58. doi:10.1016/0025-5408(88)90224-3.
[24] F.S. Baumann, J. Fleig, G. Cristiani, B. Stuhlhofer, H.-U. Habermeier, J. Maier, Quantitative Comparison of Mixed Conducting SOFC Cathode Materials by Means of Thin Film Model Electrodes, J. Electrochem. Soc. 154 (2007) B931. doi:10.1149/1.2752974.
[25] E.D. Wachsman, G. Cohn, Y.L. Huang, C. Pellegrinelli, From in-Situ to in-Operando Evaluation of SOFC Cathodes for Enhanced ORR Activity and Durability, ECS. 78 (2017) 835–845.
[26] L. Wang, R. Merkle, F.S. Baumann, J. Fleig, J. Maier, $(Ba_xSr_{1-x})(Co_yFe_{1-y})O_{3-\delta}$ Perovskites as SOFC Cathode Material: Electrode-Electrolyte Reactions and Electrochemical Characterisation, Society. 7 (2007) 1015–1024. doi:10.1149/1.2729197.
[27] L. Wang, R. Merkle, Y. a. Mastrikov, E. a. Kotomin, J. Maier, Oxygen exchange kinetics on solid oxide fuel cell cathode materials—general trends and their mechanistic interpretation, J. Mater. Res. 27 (2012) 2000–2008. doi:10.1557/jmr.2012.186.
[28] M.L. Traulsen, C. Chatzichristodoulou, K.V. Hansen, L.T. Kuhn, P. Holtappels, M.B. Mogensen, Need for In Operando Characterization of Electrochemical Interface Features, ECS Trans. 66 (2015) 3–20.
[29] D.B. Chrisey, I. Boyd, Pulsed laser deposition of thin films, 2003. doi:doi:10.1201/NOE0750309608.ch89.
[30] P. Plonczak, A. Bieberle-Hütter, M. Søgaard, T. Ryll, J. Martynczuk, P.V. Hendriksen, L.J. Gauckler, Tailoring of $La_x Sr_{1-x} Co_y Fe_{1-y} O_{3-\delta}$ Nanostructure by Pulsed Laser Deposition, Adv. Funct. Mater. 21 (2011) 2764–2775. doi:10.1002/adfm.201100251.
[31] M.L. Machala, Surface Cation Heterogeneity in Perovskite Oxides Connected to Catalytic Activity and Stability, 2017.
[32] J. Goldstein, D.E. Newbury, D.C. Joy, C.E. Lyman, P. Echlin, E. Lifshin, L. Sawyer, J.R. Michael, Scanning Electron Microscopy and X-ray Microanalysis, 2003. doi:10.1007/978-1-4615-0215-9.
[33] S. Sadewasser, T. Glatzel, Kelvin Probe Force Microscopy, 2011. doi:10.1007/978-3-642-22566-6.
[34] W. Melitz, J. Shen, A.C. Kummel, S. Lee, Kelvin probe force microscopy and its application, Surf. Sci. Rep. 66 (2011) 1–27. doi:10.1016/j.surfrep.2010.10.001.
[35] U. Zerweck, C. Loppacher, T. Otto, S. Grafström, L.M. Eng, Accuracy and resolution limits of Kelvin probe force microscopy, Phys. Rev. B - Condens. Matter Mater. Phys. 71 (2005) 1–9. doi:10.1103/PhysRevB.71.125424.
[36] T. Glatzel, S. Sadewasser, M.C. Lux-Steiner, Amplitude or frequency modulation-detection in Kelvin probe force microscopy, Appl. Surf. Sci. 210 (2003) 84–89. doi:10.1016/S0169-4332(02)01484-8.
[37] L. Nony, F. Bocquet, C. Loppacher, T. Glatzel, On the relevance of the atomic-scale contact potential difference by amplitude-modulation and frequency-modulation Kelvin probe force microscopy., Nanotechnology. 20 (2009) 264014. doi:10.1088/0957-4484/20/26/264014.
[38] Z. Ma, J. Mu, J. Tang, H. Xue, H. Zhang, C. Xue, J. Liu, Y. Li, Potential sensitivities in frequency modulation and heterodyne amplitude modulation Kelvin probe force microscopes, (2013) 1–6.

[39] K. V. Hansen, Y. Wu, T. Jacobsen, M.B. Mogensen, L. Theil Kuhn, Improved controlled atmosphere high temperature scanning probe microscope, Rev. Sci. Instrum. 84 (2013) 1–8. doi:10.1063/1.4811848.
[40] M.E. Orazem, B. Tribollet, Electrochemical Impedance Spectroscopy, 2005. https://books.google.com.br/books?hl=pt-BR&lr=&id=8hNkOWO_DLwC&oi=fnd&pg=PR5&dq=electrical+impedance+spectroscopy+review&ots=kQyjBc-wiV&sig=9UtOzxMFT62oUYZAQQc1XivpdhI#v=onepage&q=electrical impedance spectroscopy review&f=false.
[41] E. Barsoukov, J.R. Macdonald, Impedance Spectroscopy Theory, Experiment and Applications, 2005.
[42] J.F. Watts, J. Wolstenholme, An Introduction to Surface Analysis by XPS and AES 1st Edition, 2003. doi:10.1002/0470867930.
[43] E.J. Crumlin, H. Bluhm, Z. Liu, In situ investigation of electrochemical devices using ambient pressure photoelectron spectroscopy, J. Electron Spectros. Relat. Phenomena. 190 (2013) 84–92. doi:10.1016/j.elspec.2013.03.002.
[44] E.J. Crumlin, Z. Liu, H. Bluhm, W. Yang, J. Guo, Z. Hussain, X-ray spectroscopy of energy materials under in situ/operando conditions, J. Electron Spectros. Relat. Phenomena. 200 (2015) 264–273. doi:10.1016/j.elspec.2015.06.008.
[45] M.K. Abyaneh, L. Gregoratti, M. Amati, M. Dalmiglio, M. Kiskinova, Scanning Photoelectron Microscopy: a Powerful Technique for Probing Micro and Nano-Structures, E-Journal Surf. Sci. Nanotechnol. 9 (2011) 158–162. doi:10.1380/ejssnt.2011.158.
[46] B. Bozzini, M. Amati, L. Gregoratti, C. Mele, M.K. Abyaneh, M. Prasciolu, M. Kiskinova, In-situ photoelectron microspectroscopy during the operation of a single-chamber SOFC, Electrochem. Commun. 24 (2012) 104–107. doi:10.1016/j.elecom.2012.09.001.
[47] M. Amati, M.K. Abyaneh, L. Gregoratti, Dynamic High Pressure: a novel approach toward near ambient pressure photoemission spectroscopy and spectromicroscopy, J. Instrum. 8 (2013) T05001–T05001. doi:10.1088/1748-0221/8/05/T05001.
[48] H. Sezen, M. Al-Hada, M. Amati, L. Gregoratti, *In situ* chemical and morphological characterization of copper under near ambient reduction and oxidation conditions, Surf. Interface Anal. (2017). doi:10.1002/sia.6276.
[49] T. Kawada, J. Suzuki, M. Sase, A. Kaimai, K. Yashiro, Y. Nigara, J. Mizusaki, K. Kawamura, H. Yugami, Determination of Oxygen Vacancy Concentration in a Thin Film of $La_{0.6}Sr_{0.4}CoO_{3-\delta}$ by an Electrochemical Method, J. Electrochem. Soc. 149 (2002) E252. doi:10.1149/1.1479728.
[50] G.C. Kostogloudis, C. Ftikos, Properties of A-site-deficient $La_{0.6}Sr_{0.4}Co_{0.2}Fe_{0.8}O_{3-\delta}$ based perovskite oxides, Solid State Ionics. 126 (1999) 143–151. doi:10.1016/S0167-2738(99)00230-1.
[51] D. Mantzavinos, A. Hartley, I.S. Metcalfe, M. Sahibzada, Oxygen stoichiometries in $La_{1-x}Sr_xCo_{1-y}Fe_yO_{3-\delta}$ perovskites at reduced oxygen partial pressures, Solid State Ionics. 134 (2000) 103–109. doi:10.1016/S0167-2738(00)00718-9.
[52] L.W. Tai, M.M. Nasrallah, H.U. Anderson, Thermochemical Stability, Electrical-Conductivity, and Seebeck Coefficient of Sr-Doped $LaCo_{0.2}Fe_{0.8}O_{3-\delta}$, J. Solid State Chem. 118 (1995) 117–124.
[53] B.A. Boukamp, N. Hildenbrand, H.J.M. Bouwmeester, D.H.A. Blank, Impedance of thin film cathodes: Thickness and current collector dependence, Solid State Ionics. 283 (2015) 81–90. doi:10.1016/j.ssi.2015.10.013.
[54] P. Plonczak, M. Søgaard, A. Bieberle-Hütter, P.V. Hendriksen, L.J. Gauckler, Electrochemical Characterization of $La_{0.58}Sr_{0.4}Co_{0.2}Fe_{0.8}O_{3-\delta}$ Thin Film Electrodes Prepared by Pulsed Laser Deposition, J. Electrochem. Soc. 159 (2012) B471. doi:10.1149/2.043204jes.
[55] N.J. Simrick, A. Bieberle-hütter, T.M. Ryll, J.A. Kilner, A. Atkinson, J.L.M. Rupp, An investigation of the oxygen reduction reaction mechanism of $LaLa_{0.6}Sr_{0.4}Co_{0.2}Fe_{0.8}O_3$ using patterned thin films, Solid State

Ionics. 206 (2012) 7–16. doi:10.1016/j.ssi.2011.10.029.
[56] P. Ried, E. Bucher, W. Preis, W. Sitte, P. Holtappels, Characterisation of $La_{0.6}Sr_{0.4}Co_{0.2}Fe_{0.8}O_{3-\delta}$ and $Ba_{0.5}Sr_{0.5}Co_{0.8}Fe_{0.2}O_{3-\delta}$ as Cathode Materials for the Application in Intermediate Temperature Fu, ECS Trans. 7 (2007) 1217–1224.
[57] A. Zomorrodian, H. Salamati, Z. Lu, X. Chen, N. Wu, A. Ignatiev, Electrical conductivity of epitaxial $La_{0.6}Sr_{0.4}Co_{0.2}Fe_{0.8}O_{3-\delta}$ thin films grown by pulsed laser deposition, Int. J. Hydrogen Energy. 35 (2010) 12443–12448. doi:10.1016/j.ijhydene.2010.08.100.
[58] D. Oh, J. Yoo, D. Gostovic, K.S. Jones, E.D. Wachsman, A Kinetic Study of Catalytic Activity Degradation of $La_{0.6}Sr_{0.4}Co_{0.2}Fe_{0.8}O_{3-\delta}$, ECS Trans. 16 (2009) 97–105.
[59] C. Niedrig, S.F. Wagner, W. Menesklou, S. Baumann, E. Ivers-tiffée, Oxygen equilibration kinetics of mixed-conducting perovskites BSCF , LSCF , and PSCF at 900 ° C determined by electrical conductivity relaxation, 283 (2015) 30–37.
[60] Y. Li, K. Gerdes, T. Horita, X. Liu, Surface Exchange and Bulk Diffusivity of LSCF as SOFC Cathode: Electrical Conductivity Relaxation and Isotope Exchange Characterizations, J. Electrochem. Soc. 160 (2013) F343–F350. doi:10.1149/2.044304jes.
[61] J.A. Lane, S.J. Benson, D. Waller, J.A. Kilner, Oxygen transport in $La_{0.6}Sr_{0.4}Co_{0.2}Fe_{0.8}O_{3-\delta}$, Solid State Ionics. 121 (1999) 201–208. doi:10.1016/S0167-2738(99)00014-4.
[62] E.N. Armstrong, K.L. Duncan, D.J. Oh, J.F. Weaver, E.D. Wachsman, Determination of Surface Exchange Coefficients of LSM, LSCF, YSZ, GDC Constituent Materials in Composite SOFC Cathodes, J. Electrochem. Soc. 158 (2011) B492. doi:10.1149/1.3555122.
[63] J. Fleig, J. Maier, The polarization of mixed conducting SOFC cathodes: Effects of surface reaction coefficient, ionic conductivity and geometry, J. Eur. Ceram. Soc. 24 (2004) 1343–1347. doi:10.1016/S0955-2219(03)00561-2.
[64] J. Maier, On the correlation of macroscopic and microscopic rate constants in solid state chemistry, Solid State Ionics. 112 (1998) 197–228. doi:10.1016/S0167-2738(98)00152-0.
[65] B.A. Boukamp, N. Hildenbrand, P. Nammensma, D.H.A. Blank, The impedance of thin dense oxide cathodes, Solid State Ionics. 192 (2011) 404–408. doi:10.1016/j.ssi.2010.05.037.
[66] C.W. Tanner, A. V. Virkar, A simple model for interconnect design of planar solid oxide fuel cells, J. Power Sources. 113 (2003) 44–56. doi:10.1016/S0378-7753(02)00479-2.
[67] W. Yang, Z. Wang, Z. Wang, Z. Yang, C. Xia, R. Peng, X. Wu, Y. Lu, Enhanced Catalytic Activity toward O2 Reduction on Pt-Modified $La_{1-x}Sr_xCo_{1-y}Fe_yO_{3-\delta}$ Cathode: A Combination Study of First- Principles Calculation and Experiment, ACS Appl. Mater. Interfaces. 6 (2014) 21051–21059. doi:10.1021/am505900g.
[68] S.P. Simner, M.D. Anderson, L.R. Pederson, J.W. Stevenson, Performance Variability of $La(Sr)FeO_3$ SOFC Cathode with Pt, Ag, and Au Current Collectors, J. Electrochem. Soc. 152 (2005) A1851. doi:10.1149/1.1995687.
[69] Y.-L. Huang, A.M. Hussain, C. Pellegrinelli, C. Xiong, E.D. Wachsman, Chromium Poisoning Effects on Surface Exchange Kinetics of $La_{0.6}Sr_{0.4}Co_{0.2}Fe_{0.8}O_{3-\delta}$, ACS Appl. Mater. Interfaces. 9 (2017) 16660–16668. doi:10.1021/acsami.7b02762.
[70] M. Perz, E. Bucher, C. Gspan, J. Waldhäusl, F. Hofer, W. Sitte, Long-termdegradation of $La_{0.6}Sr_{0.4}Co_{0.2}Fe_{0.8}O_{3-\delta}$ IT-SOFC cathodes due to silicon poisoning, Solid State Ionics. 288 (2016) 22–27. doi:10.1016/j.ssi.2016.01.005.
[71] E. Bucher, W. Sitte, F. Klauser, E. Bertel, Oxygen exchange kinetics of $La_{0.58}Sr_{0.4}Co_{0.2}Fe_{0.8}O_3$ at 600 °C in dry and humid atmospheres, Solid State Ionics. 191 (2011) 61–67. doi:10.1016/j.ssi.2011.03.019.
[72] M. Niania, R. Podor, S.J. Skinner, J.A. Kilner, In-Situ Surface Analysis of SOFC Cathode Degradation Using High Temperature Environmental Scanning Electron Microscopy, ECS Trans. 68 (2015) 665–670.

doi:10.1149/06801.0665ecst.
[73] S. Gupta, J.A. Lane, J.R. Wilson, P.J. Plonczak, P. Singh, Interfacial stability of iron doped lanthanum strontium chromite and Scandia stabilized zirconia in oxidizing and reducing atmosphere, Solid State Ionics. 288 (2016) 10–13. doi:10.1016/j.ssi.2016.01.010.
[74] W. Lee, B. Yildiz, Factors that influence Cation Segregation at the Surfaces of Perovskite Oxides, ECS Trans. 57 (2013) 2115–2123.
[75] I. Petrov, P.B. Barna, L. Hultman, J.E. Greene, Microstructural evolution during film growth, J. Vac. Sci. Technol. A Vacuum, Surfaces, Film. 21 (2003) S117–S128. doi:10.1116/1.1601610.
[76] J.A. Thornton, Influence of apparatus geometry and deposition conditions on the structure and topography of thick sputtered coatings, J. Vac. Sci. Technol. 11 (1974) 666–670. doi:10.1116/1.1312732.
[77] J.A. Thornton, High Rate Thick Film Growth, Annu. Rev. Mater. Sci. 7 (1977) 239–260. doi:10.1146/annurev.ms.07.080177.001323.
[78] H.U. Habermeier, Thin films of perovskite-type complex oxides, Mater. Today. 10 (2007) 34–43. doi:10.1016/S1369-7021(07)70243-2.
[79] M. Lorenz, H. Hochmuth, M. Kneï¿½, M. Bonholzer, M. Jenderka, M. Grundmann, From high-Tcsuperconductors to highly correlated Mott insulators - 25 years of pulsed laser deposition of functional oxides in Leipzig, Semicond. Sci. Technol. 30 (2015). doi:10.1088/0268-1242/30/2/024003.
[80] J. Santiso, M. Burriel, Deposition and characterisation of epitaxial oxide thin films for SOFCs, J. Solid State Electrochem. 15 (2011) 985–1006. doi:10.1007/s10008-010-1214-6.
[81] A. Orsini, P.G. Medaglia, S. Sanna, E. Traversa, S. Licoccia, A. Tebano, G. Balestrino, Epitaxial superlattices of ionic conductor oxides, Superlattices Microstruct. 46 (2009) 223–226. doi:10.1016/j.spmi.2008.10.047.
[82] T.V. Aksenova, M.V. Anan'ev, L.Y. Gavrilova, V.. A. Cherepanov, Phase equilibria and crystal structures of solid solutions in the System $LaCoO_{3-d}$–$SrCoO_{2.5\pm d}$–$SrFeO_{3-d}$–$LaFeO_{3-d}$, Inorg. Mater. 43 (2007) 347–351. doi:10.1134/S0020168509030108.
[83] M. Yashima, T. Kamioka, Neutron diffraction study of the perovskite-type lanthanum cobaltite $La_{0.6}Sr_{0.4}Co_{0.8}Fe_{0.2}O_{3-\delta}$ at 1260 °C and 394 °C, Solid State Ionics. 178 (2008) 1939–1943. doi:10.1016/j.ssi.2008.01.032.
[84] D. Pergolesi, V. Esposito, A. Tebano, P.G. Medaglia, S. Sanna, S. Licoccia, G. Balestrino, E. Traversa, Ceria-Based Thin Film Hetero-structure Growth and Characterization for SOFC Applications, ECS Trans. 7 (2007) 891–898. doi:10.1149/1.2729181.
[85] C.C. Appel, N. Bonanos, A. Horsewell, S. Linderoth, Ageing behaviour of zirconia stabilized by yttria and manganase oxide, J. Mater. Sci. 36 (2001) 4493–4501.
[86] S. Gewies, W.G. Bessler, Physically Based Impedance Modeling of Ni/YSZ Cermet Anodes, J. Electrochem. Soc. 155 (2008) B937–B952. doi:10.1149/1.2943411.
[87] S. Kazlauskas, A. Kežionis, T. Šalkus, A.F. Orliukas, Electrical properties of YSZ and CaSZ single crystals, Solid State Ionics. 231 (2013) 37–42. doi:10.1016/j.ssi.2012.10.020.
[88] F.S. Baumann, J. Fleig, H.U. Habermeier, J. Maier, Impedance spectroscopic study on well-defined (La,Sr)(Co,Fe)$O_{3-\delta}$ model electrodes, Solid State Ionics. 177 (2006) 1071–1081. doi:10.1016/j.ssi.2006.02.045.
[89] J.J. Randall, R. Ward, The Preparation of Some Ternary Oxides of the Platinum Metals, J. Am. Chem. Soc. 81 (1959) 2629–2631. doi:10.1021/ja01520a007.
[90] G.M. Rupp, A. Limbeck, M. Kubicek, A. Penn, M. Stöger-Pollach, G. Friedbacher, J. Fleig, Correlating surface cation composition and thin film microstructure with the electrochemical performance of lanthanum strontium cobaltite (LSC) electrodes, J. Mater. Chem. A. 2 (2014) 7099–7108. doi:10.1039/C3TA15327D.

[91] G.M. Rupp, A.K. Opitz, A. Nenning, A. Limbeck, J. Fleig, Real-time impedance monitoring of oxygen reduction during surface modification of thin film cathodes, Nat. Mater. 16 (2017) 640–645. doi:10.1038/nmat4879.
[92] N. Tsvetkov, Q. Lu, L. Sun, E.J. Crumlin, B. Yildiz, Improved chemical and electrochemical stability of perovskite oxides with less reducible cations at the surface, Nat. Mater. 15 (2016) 1010–1016. doi:10.1038/nmat4659.
[93] J. Fleig, On the current-voltage characteristics of charge transfer reactions at mixed conducting electrodes on solid electrolytes., Phys. Chem. Chem. Phys. 7 (2005) 2027–2037. doi:10.1039/B501086A.
[94] Y.A. Mastrikov, R. Merkle, E. Heifets, E.A. Kotomin, J. Maier, Pathways for oxygen incorporation in mixed conducting perovskites: A DFT-based Mechanistic analysis for (La, Sr)$MnO_{3-\delta}$, J. Phys. Chem. C. 114 (2010) 3017–3027. doi:10.1021/jp909401g.
[95] R. Merkle, J. Maier, How is oxygen incorporated into oxides? A comprehensive kinetic study of a simple solid-state reaction with SrTiO3 as a model material, Angew. Chemie - Int. Ed. 47 (2008) 3874–3894. doi:10.1002/anie.200700987.
[96] Z. a. Feng, M.L. Machala, W.C. Chueh, Surface electrochemistry of CO_2 reduction and CO oxidation on Sm-doped CeO_{2-x} : coupling between Ce^{3+} and carbonate adsorbates, Phys. Chem. Chem. Phys. 17 (2015) 12273–12281. doi:10.1039/C5CP00114E.
[97] Z. a. Feng, F. El Gabaly, X. Ye, Z.-X. Shen, W.C. Chueh, Fast vacancy-mediated oxygen ion incorporation across the ceria–gas electrochemical interface, Nat. Commun. 5 (2014) 1–9. doi:10.1038/ncomms5374.
[98] Z.A. Feng, C. Balaji Gopal, X. Ye, Z. Guan, B. Jeong, E. Crumlin, W.C. Chueh, Origin of Overpotential-Dependent Surface Dipole at CeO_{2-x}/Gas Interface during Electrochemical Oxygen Insertion Reactions, Chem. Mater. 28 (2016) 6233–6242. doi:10.1021/acs.chemmater.6b02427.
[99] A. Nenning, A.K. Opitz, C. Rameshan, R. Rameshan, R. Blume, M. Hävecker, A. Knop-Gericke, G. Rupprechter, B. Klötzer, J. Fleig, Ambient pressure XPS study of mixed conducting perovskite-type SOFC cathode and anode materials under well-defined electrochemical polarization, J. Phys. Chem. C. 120 (2016) 1461–1471. doi:10.1021/acs.jpcc.5b08596.
[100] D.N. Mueller, M.L. Machala, H. Bluhm, W.C. Chueh, Redox activity of surface oxygen anions in oxygen-deficient perovskite oxides during electrochemical reactions., Nat. Commun. 6 (2015) 6097. doi:10.1038/ncomms7097.
[101] CasaXPS©, (2018) Casa Software Ltd., Teignmouth, United Kingdom.
[102] J.F. Moulder, W.F. Stickle, P.E. Sobol, K.D. Bomben, Handbook of X-Ray Photoelectron Spectroscopy.pdf, (1995) 255. doi:10.1002/sia.740030412.
[103] M. Larssont, P. Baltzer, S. Svensson, B. Wannbergs, N. Martensson, A.N. De Brito, N. Correia, M.P. Keanej, X-ray photoelectron , Auger electron and ion fragment spectra of 0 , and potential curves of 0 ;', 23 (1990) 1175–1195.
[104] H. Tillborg, A. Nilsson, B. Hernnäs, N. Mårtensson, R.E. Palmer, X-ray and UV photoemission studies of mono-, bi- and multilayers of physisorbed molecules: O_2 and N_2 on graphite, Surf. Sci. 295 (1993) 1–12. doi:10.1016/0039-6028(93)90180-R.
[105] E.J. Crumlin, E. Mutoro, Z. Liu, M.E. Grass, M.D. Biegalski, Y.-L. Lee, D. Morgan, H.M. Christen, H. Bluhm, Y. Shao-Horn, Surface strontium enrichment on highly active perovskites for oxygen electrocatalysis in solid oxide fuel cells, Energy Environ. Sci. 5 (2012) 6081. doi:10.1039/c2ee03397f.
[106] A. Lebugle, U. Axelsson, R. Nyholm, N. Mårtensson, Experimental L and M Core Level Binding Energies for the Metals 22 Ti to 30 Zn, Phys. Scr. 23 (1981) 825–827. doi:10.1088/0031-8949/23/5A/013.
[107] W.Y. Howng, R.J. Thorn, The multicomponent structure of the 4d orbital in X-ray Photoelectron spectra of the Lanthanum (III) ion, Chem. Phys. Lett. 56 (1978) 463–465.
[108] W.Y. Howng, R.J. Thorn, Investigation of the electronic structure of $La_{1-x}(M^{2+})_xCrO_3$, Cr_2O_3 and La_2O_3 by

x-ray photoelectron spectroscopy, (1979).
[109] Z. Guan, D. Chen, W.C. Chueh, Analyzing the dependence of oxygen incorporation current density on overpotential and oxygen partial pressure in mixed conducting oxide electrodes, Phys. Chem. Chem. Phys. 19 (2017) 23414–23424. doi:10.1039/C7CP03654J.
[110] D.N. Mueller, M.L. Machala, H. Bluhm, W.C. Chueh, Redox activity of surface oxygen anions in oxygen-deficient perovskite oxides during electrochemical reactions, Nat. Commun. 6 (2015) 6097. doi:10.1038/ncomms7097.
[111] T. Jacobsen, M. Mogensen, The Course of Oxygen Partial Pressure and Electric Potentials across an Oxide Electrolyte Cell, 13 (2008) 259–273.
[112] J.H. Joo, G.M. Choi, Electrical conductivity of thin film ceria grown by pulsed laser deposition, J. Eur. Ceram. Soc. 27 (2007) 4273–4277. doi:10.1016/j.jeurceramsoc.2007.02.135.
[113] D.. Mullins, S.. Overbury, D.. Huntley, Electron spectroscopy of single crystal and polycrystalline cerium oxide surfaces, Surf. Sci. 409 (1998) 307–319. doi:10.1016/S0039-6028(98)00257-X.
[114] M.C. Spadaro, P. Luches, G. Bertoni, V. Grillo, S. Turner, G. Van Tendeloo, S. Valeri, S. D'Addato, Influence of defect distribution on the reducibility of CeO_{2-x} nanoparticles, Nanotechnology. 27 (2016) 1–8. doi:10.1088/0957-4484/27/42/425705.
[115] P. Burroughs, A. Hamnett, A.F. Orchard, G. Thornton, Satellite Structure in the X-Ray Photoelectron Spectra of some Binary and Mixed Oxides of Lanthanum and Cerium, J. Chem. Soc. Dalt. Trans. (1976) 1686–1698. doi:10.1039/DT9760001686.
[116] T. Jacobsen, C. Chatzichristodoulou, M. Mogensen, Fermi Potential across Working Solid Oxide Cells with Zirconia or Ceria Electrolytes, ECS Trans. 61 (2014) 203–214. doi:10.1149/06101.0203ecst.
[117] COMSOL Multiphysics® v. 5.3, (n.d.) COMSOL AB, Stockholm, Sweden. www.comsol.com.
[118] K.D. Katzer, W. Mertin, G. Bacher, A. Jaeger, K. Streubel, Voltage drop in an $(Al_xGa_{1-x})_{0.5}In_{0.5}P$ light-emitting diode probed by Kelvin probe force microscopy, Appl. Phys. Lett. 89 (2006) 103521–103522. doi:10.1063/1.2347184.
[119] O. Vatel, M. Tanimoto, Kelvin probe force microscopy for potential distribution measurement of semiconductor devices, J. Appl. Phys. 77 (1995) 2358–2362. doi:10.1063/1.358758.
[120] M. Tanimoto, Kelvin probe force microscopy for characterization of semiconductor devices and processes, J. Vac. Sci. Technol. B Microelectron. Nanom. Struct. 14 (1996) 1547. doi:10.1116/1.589136.
[121] G. Leveque, P. Girard, E. Skouri, D. Yarekha, Measurements of electric potential in a laser diode by Kelvin Probe Force Microscopy, Appl. Surf. Sci. 157 (2000) 251–255. doi:10.1016/S0169-4332(99)00535-8.
[122] E.J. Fuller, D. Pan, B.L. Corso, O. Tolga Gul, J.R. Gomez, P.G. Collins, Quantitative Kelvin probe force microscopy of current-carrying devices, Appl. Phys. Lett. 102 (2013). doi:10.1063/1.4793480.
[123] D.B. Blücher, J.-E. Svensson, L.-G. Johansson, M. Rohwerder, M. Stratmann, Scanning Kelvin Probe Force Microscopy, J. Electrochem. Soc. 151 (2004) B621. doi:10.1149/1.1809590.
[124] S.S. Nonnenmann, R. Kungas, J. Vohs, D. a Bonnell, Direct In Situ Probe of Electrochemical Processes in Operating Fuel Cells, ACS Nano. (2013) 6330–6336.
[125] M. Nonnenmacher, M.P. O'Boyle, H.K. Wickramasinghe, Kelvin probe force microscopy, Appl. Phys. Lett. 58 (1991) 2921–2923. doi:10.1063/1.105227.
[126] I.R.R. Jankov, I.D.D. Goldman, R.N.N. Szente, Principles of the Kelvin Probe Force Microscopy, Rev. Bras. Ensino Física. 22 (2000) 503–509.
[127] R. Chiba, F. Yoshimura, Y. Sakurai, An investigation of $LaNi_{1-x}Fe_xO_3$ as a cathode material for solid oxide fuel cells, Solid State Ionics. 124 (1999) 281–288. doi:10.1016/S0167-2738(99)00222-2.
[128] R.N. Basu, F. Tietz, E. Wessel, H.P. Buchkremer, D. Stöver, Microstructure and electrical conductivity of $LaNi_{0.6}Fe_{0.4}O_3$ prepared by combustion synthesis routes, Mater. Res. Bull. 39 (2004) 1335–1345.

doi:10.1016/j.materresbull.2004.03.015.
[129] N. Sata, K. Ikeda, F. Iguchi, H. Yugami, Synthesis of $La_{0.6}Sr_{0.4}FeO_3/La_{0.6}Sr_{0.4}CoO_3$ mixed ion conducting superlattices by PLD, Solid State Ionics. 178 (2007) 1563–1567. doi:10.1016/j.ssi.2007.10.005.
[130] C.B. Wang, Y.X. Zhu, L. Li, Q. Shen, L.M. Zhang, Epitaxial growth and transport property of $La_{0.9}Sr_{0.1}MnO_3$ thin films deposited on MgO, $LaAlO_3$ and $SrTiO_3$ substrates, J. Alloys Compd. 693 (2017) 832–836. doi:10.1016/j.jallcom.2016.09.268.